Astrophysics and Physics of Neutrino Detection

A THESIS
SUBMITTED TO THE FACULTY OF THE GRADUATE SCHOOL
OF THE UNIVERSITY OF MINNESOTA
BY

Cheng-Hsien Li

IN PARTIAL FULFILLMENT OF THE REQUIREMENTS
FOR THE DEGREE OF
Doctor of Philosophy

Professor Yong-Zhong Qian, Advisor

September, 2017

Acknowledgements

This dissertation would be impossible to complete without the help and support from many people and institutions.

First and foremost, I would like to express my sincere gratitude to my research advisor, Professor Yong-Zhong Qian, who has patiently guided me through this long PhD journey. I learned a lot from his insights in neutrino physics and his approaches to problems during countless hours of discussion. He always offered helpful suggestions regarding my thesis projects and how to conduct rigorous research.

I would like to thank Dr. Projjwal Banerjee for guiding me on the SN1987A project presented in this thesis. He was not only a research collaborator but he is also a dear friend to me. He kindly offered advice and encouragement which helped me overcome difficulties during my PhD study. In addition, I feel grateful to have received a lot of help from then fellow graduate students, Dr. Ke-Jun Chen, Dr. Meng-Ru Wu, Dr. Zhen Yuan, Mr. Zhu Li, and Mr. Zewei Xiong, in the Nuclear Physics Group.

I am also indebted to Professor Hans-Thomas Janka and Professor Tobias Fischer for generously providing supernova simulation results from their research groups upon request, Professor Huaiyu Duan for commenting on my wave-packet project, and Professor Alexander Heger for the computing resource I received in the research group. I would also like to thank Professor Joseph Kapusta, Professor Thomas Jones, and Professor Daniel Cronnin-Hennessy for serving as the committee members in my preliminary oral examination and thesis defense

examination. I also feel very grateful for the long-term financial support from the Nuclear Physics Group and from the School of Physics and Astronomy as well as the travel support from the 2013 TAUP Summer School, the 2015 IPA Symposium, the Center for Nuclear Astrophysics at Shanghai Jiao Tong University, and the NuPhys2015 conference.

Finally, it is my privilege to befriend many nice and great people I met in Minnesota and they have made my PhD journey a memorable one.

Dedication

To my mother Miao-Ru Chu. 謹以此論文，獻給我的母親朱妙如女士。

Abstract

A galactic core-collapse supernova is a powerful neutrino source of which the signals can be picked up by a water Cherenkov detector on the Earth. From an astrophysical point of view, the signals reveal the dynamics of core-collapse supernova explosion and the subsequent cooling of a proto-neutron star (PNS). In this regard, we compare the neutrino emission profiles from the recent 1D hydrodynamics simulation by Mirizzi et al. (2016) with the historical SN1987A data through a statistical goodness-of-fit test. Such test reveals the tension between the data and rapid PNS cooling prescribed by the convection treatment employed in the simulation. The implications will be discussed. From a quantum-mechanical point of view, on the other hand, the supernova neutrino flux is so intensive such that a huge degree of wave-packet overlap is estimated. Such overlap may give rise to an interference effect known as the Hanbury Brown and Twiss (HBT) effect. We derive the solution for a 3D Gaussian wave packet and, with such solution, the joint-detection probability. We demonstrate that an observable interference occurs if the joint-detection were to render the two detected neutrinos in the same phase space cell. Upon further examination, however, we conclude that such effect is difficult to observe from neutrinos in practical experimental settings.

Contents

List of Tables

List of Figures

Chapter 1

Introduction

Stars born with different progenitor masses end their lives differently [1]. During the lifetime of a star, the core forms an onion-like structure of concentric layers with elements of mass number arranged in a descending order away from the core. As each thermonuclear fusion stage of a stellar core comes to an end due to fuel depletion, the core contraction is accelerated resulting in further increase of the core's temperature and density. Such increase may ignite the subsequent nuclear fusion to form heavier elements in its core. For a star with a progenitor mass $M \lesssim 8M_\odot$, the stellar core may undergo hydrogen burning ($M > 0.08M_\odot$), helium burning ($M > 0.5M_\odot$), and carbon burning ($M > 7M_\odot$) and then cools down afterward as a white dwarf which is supported by the degeneracy pressure of non-relativistic electrons.

On the other hand, a more massive star will eventually develop a core exceeding the Chandrasekhar mass limit [2],

$$M_{\rm ch} \approx 1.44 \left(\frac{Y_e}{0.5}\right)^2 M_\odot, \tag{1.1}$$

where Y_e is the ratio of electrons to baryons, such that the electron degeneracy pressure can no longer balance its self-gravity. More specifically, the star can form an O-Ne-Mg core ($8M_\odot \lesssim M \lesssim 9M_\odot$) or an iron core ($M \gtrsim 9M_\odot$), of which the density can reach 10^{10} g/cm^3. At such density, two processes [3] can reduce the

core's sustaining pressure thereby triggering a gravitational collapse – the ultimate fate of massive stars. The first process is the electron capture by heavy nuclei or free protons,

$$\begin{aligned} e^- + \mathcal{N}(Z, A) &\rightarrow \mathcal{N}(Z-1, A) + \nu_e \\ e^- + p &\rightarrow n + \nu_e \end{aligned} \tag{1.2}$$

enabled by the Fermi energy of (relativistic) electrons,

$$\epsilon_F = \hbar c \left(3\pi^2 n_e\right)^{\frac{1}{3}}, \tag{1.3}$$

where n_e is the electron number density, reaching the electron capture energy threshold at an order of 10 MeV. This electron capture process reduces the electron number as well as the degeneracy pressure at the core. It is primarily responsible for triggering the collapse of stars with progenitor mass $8M_\odot \lesssim M \lesssim 9M_\odot$. The second process is the photo-disintegration of iron-group nuclei

$$\gamma + {}^{56}Fe \rightleftharpoons 13\alpha + 4n - 124 \text{ MeV}, \tag{1.4}$$

the forward reaction of which is favored by the nuclear statistical equilibrium at a temperature $T \sim 10^{10}$ K and reduces the thermal pressure. The collapse of stars with $9M_\odot \lesssim M \lesssim 100M_\odot$ is mainly caused by the photo-disintegration process. Once the stellar collapse commences, nothing stops the core from getting denser and denser until the collapse is abruptly stopped by the stiffened nuclear equation of state (EOS) at the nuclear density[1] $\rho \sim 10^{14}$ g/cm^3. Subsequently, the bounced core immediately launches an outward shock wave while the outer part of the core is still collapsing. Such shock wave will eventually expel the stellar mantle into the interstellar medium and, hence, the supernova (SN) explodes.

The collapsed core releases an enormous amount of gravitational binding energy. With the proto-neutron star (PNS) radius $R_{\rm PNS} \sim 10$ km and mass $M_{\rm PNS} \sim$

[1] This dramatic density rise from the pre-collapse density to the nuclear density occurs in less than one second.

$M_\odot$, an order-of-magnitude estimate suggests that the liberated binding energy amounts to

$$E_b \sim \frac{GM_{\rm PNS}^2}{R_{\rm PNS}} \approx 3 \times 10^{53} \text{ erg}. \tag{1.5}$$

As the layers overlying the collapsing core are optically opaque, neutrinos and anti-neutrinos (hereafter referred to as "neutrinos" in this chapter), which interact weakly, provide an efficient way of radiating this amount of energy over a time scale of 10 seconds. In fact, neutrinos are responsible for carrying away $\sim 99\%$ of this energy budget in comparison to the rest $\sim 1\%$ by the explosion ejecta in the form of kinetic energy and $\ll 1\%$ by photons. This suggests that neutrinos play a critical role in the dynamics of SN explosion and the subsequent cooling of the compact remnant. With the typical energy $E_\nu \sim 10$ MeV, a number 10^{58} of neutrinos implied by the energy budget can provide observable signals for detectors on the Earth thereby offering an effective probe for revealing information about the collapsing stellar core. In fact, the SN1987A event has already provided such opportunity to validate SN models, albeit with very limited statistics. A more in-depth discussion about the experimental signals of SN neutrinos and the constraint from the SN1987A data will be given in the first part of this thesis.

In addition to understanding the most intensive neutrino sources – core-collapse SNe – in the universe, a better description of neutrinos themselves has also been sought after in the past decades. As has been established by numerous neutrino oscillation experiments [4], the neutrino production-propagation-detection process involves quantum interference among the neutrino's mass eigenstates. Such quantum interference is further complicated by a more realistic form – wave packet (WP) – of the neutrino's wave function. Since the seminal discussion was given in [5], theoretical efforts have been devoted to seeking for proper description of neutrinos as WPs. By treating the neutrino as an intermediate WP propagating between its production and detection locations (the quantum-mechanical approach) [6, 5, 7, 8, 9, 10] or as a virtual particle in a macroscopic Feynman diagram in which the external particles are described as WPs (the field-theoretical approach)

[11, 12, 13, 14, 15, 10, 16, 17, 18], the formula of neutrino oscillations has been derived and compared with the one obtained by assuming neutrinos as plane waves. Although the plane wave treatment yields a simple and satisfactory description of neutrino oscillations for the purpose of experimental fitting, its paradoxical implications (see [19] for a review) causes confusions and it also neglects several oscillation-suppressing factors in the flavor transformation probabilities predicted by the WP treatments. These suppression factors are fundamentally connected with quantum-mechanical uncertainties inherent to the WP description and testify the importance of proper description of neutrinos.

The aforementioned studies focused on neutrino oscillations for which 1D description of neutrinos suffices because the coherence conditions concern the separation of mass-eigenstate components due to the difference in their group velocities. One shortcoming of the 1D picture, however, is that it neglects potential overlap of 3D neutrino wave functions which may induce interference among them. Here, the wave-function overlap between two neutrinos should not be confused with the overlap of the mass-eigenstate components of a neutrino; the former and its consequences are the main issues we would like to address in the second part of this thesis while the later concerns the coherence conditions of neutrino oscillations for which a subset of the literature is given above. One known interference effect is the Hanbury Brown and Twiss (HBT) effect [20, 21, 22]. Originally proposed as an intensity interferometry technique in astronomy, the HBT effect has been applied to subatomic physics [23] and realized [24, 25] with particles other than photons. The potential applications of the HBT effect with neutrinos has been discussed: A theoretical possibility of using the HBT effect to probe the neutrino nature – whether neutrinos are Dirac or Majorana particles – was discussed in [26] a decade ago. Very recently, the idea of measuring the diameter of a PNS from a galactic SN event was proposed [27]. In this thesis, we aim to derive the conditions for and analyze the viability of observing the neutrino HBT effect. As our focus is on the potential interference among neutrinos, we will neglect the neutrino masses (thus neutrino oscillations) for a succinct presentation.

The rest of this thesis is organized as follows:

- In Chapter 2, we give a brief review on the standard stellar collapse theory and an update of the current status of 1D SN simulation. Then we discuss the detection of SN neutrinos in a water Cherenkov detector and some experimental issues relevant to the SN1987A observation.

- In Chapter 3, we carry out a statistical goodness-of-fit test on the latest 1D simulation models with the SN1987A data. We identify some disagreement between the simulation models and the data. A possible fallback scenario to eliminate the disagreement will be explored.

- In Chapter 4, we model neutrinos as a 3D Gaussian wave packet and discuss methods to derive its quantum evolution in time. With such solution, we elucidate the concept of wave-particle duality.

- In Chapter 5, we discuss the wave packet detection in a quantum-mechanical framework. The transition amplitude of one-particle detection will be applied to deriving the joint-detection probability which shows an interference term between two detected identical particles. The conditions for the interference effect will be derived.

- In Chapter 6, we develop a wave packet overlap model based on the interference conditions from the joint-detection probability. We examine various sources for possible observation of the interference effect in neutrino experiments.

- In Chapter 7, a brief summary of the findings in this thesis will be given.

Chapter 2

Core-Collapse Supernovae Neutrinos

After the stellar core collapses and bounces, the launched shock wave can be viewed as a moving boundary which divides two regions – unshocked and post-shocked – with distinct characteristics (temperature, density, velocity, and etc.). As materials are accreted across this boundary, heavy nuclei are broken up into free nucleons at the cost of about 9 MeV per nucleon. In fact, the shock wave is heavily taxed by such energy cost and, as a result, the shock wave becomes weakened and even "stalled"[1] . It has been established that the stalled shock wave can be revived by the energy deposition by neutrinos in the post-shock region for a successful SN explosion. Depending on the amount of materials the shock wave has to traverse through, it can take up to a few hundred milliseconds for the shock revival to occur. This scenario is the delayed neutrino-heating mechanism [28]. In the following, we discuss the characteristics of neutrino emission as well as the interplay between the shock wave and neutrinos in a core-collapse SN explosion.

[1] The shock front apparently comes to a stop relative to an observer at rest far away from the star.

2.1 Delayed Neutrino-Heating Mechanism

In the delayed scenario of core-collapse SN explosion, the neutrino emission can be characterized by

1. a prompt neutronization burst of ν_e,
2. an accretion phase during which ν_e and $\bar{\nu}_e$ are abundantly produced compared to other non-electron species, and
3. a Kelvin-Helmholtz cooling phase of the PNS during which thermal neutrinos and anti-neutrinos of all flavors are emitted.

The accretion phase and cooling phase altogether constitute the major observable neutrino signal of core-collapse SN explosion. These stages will be discussed in the following.

2.1.1 Neutronization Burst

As the gravitational collapse begins, the neutrino emission is dominated by the ν_e production via the electron capture process shown in Eq. (1.2). The produced neutrinos initially escape the stellar core freely but soon become trapped by iron nuclei when the core density exceeds $\rho_{\rm trap,Fe} \sim 10^{11}$ g/cm^3. The emission of ν_e at this time is temporarily shut off while the electron capture process as well as the collapse-and-bounce process of the core continues. After the core bounces, the hydrodynamic shock wave dissociates nuclei into free nucleons on its way out, creating a more favorable condition for ν_e production in the post-shock region because electron capture is more efficient on free protons than on nuclei. Compared to iron nuclei, free nucleons are also more transparent to ν_e and correspond to a ν_e-trapping density $\rho_{\rm trap,nucleon} \sim 10^{12}$ g/cm^3. Consequently, a huge amount of ν_e pile up behind the shock wave until it reaches the density layer $\rho \sim 10^{11}$ g/cm^3 where the unshocked iron nuclei become transparent. This results in a brief yet

luminous emission of ν_e which is termed the neutronization burst[2] . Although the luminosity can reach $L \sim 10^{53}$ erg/s, this prompt ν_e burst lasts only a few milliseconds and can only carry away $\sim 1\%$ of the total neutrino energy budget.

2.1.2 Accretion Phase

Within a few milliseconds after core-bounce, the shock front soon stagnates at a few hundred kilometers from the core as the ν_e burst drains energy from the post-shock region and iron nuclei continue to fall through. The PNS formed below this accretion shock initially has a radius of ~ 100 km. Through out the accretion phase and the cooling phase, the PNS will first undergo a rapid contraction to a radius ~ 20 km within the first second after core-bounce and then slowly contract to a radius less than 15 km over a 10-second time scale. Inside the hot core of the PNS with a temperature up to a few tens of MeV, thermal neutrinos and anti-neutrinos of all flavors are produced via neutral current interactions [29]:

$$\begin{aligned}
&e^- + e^+ \to \nu + \bar{\nu} && \text{(pair annihilation)} \\
&e^\pm + N \to e^\pm + N + \nu + \bar{\nu} && \text{(electron–nucleon bremsstrahlung)} \\
&N + N \to N + N + \nu + \bar{\nu} && \text{(nucleo–nucleon bremsstrahlung)} \\
&\gamma \to \nu + \bar{\nu} && \text{(plasmon decay)} \\
&\gamma + e^\pm \to e^\pm + \nu + \bar{\nu} && \text{(photo–annihilation).}
\end{aligned} \tag{2.1}$$

Additionally, electron neutrinos and anti-neutrinos can also be produced, with abundant electron-positron pairs at such temperature, via (the forward reaction of) the charged current interactions

$$\begin{aligned}
e^- + p &\rightleftharpoons n + \nu_e \\
e^+ + n &\rightleftharpoons p + \bar{\nu}_e.
\end{aligned} \tag{2.2}$$

[2] This term is somewhat misleading as the burst only carries away a small fraction of electron lepton number of the core.

These thermal neutrinos diffuse out of the flavor-dependent neutrino spheres[3] with luminosities characterized by the Stephan-Boltzman's law[30]

$$L_{\nu}^{\rm core} \sim 4\pi R_{\nu}^2 \times \sigma_{\nu} T_{\nu}^4, \tag{2.3}$$

where $\sigma_{\nu} = 4.50 \times 10^{35}$ erg MeV^{-4} cm^{-2} sec^{-1}, R_{ν} is the neutrino sphere radius, and T_{ν} is the effective temperature at the neutrino sphere surface. In addition to the "core component", additional ν_e and $\bar{\nu}_e$ production through Eq. (2.2) also takes place between the neutrino spheres and the stalled shock. Assuming a quasi-stationary state, the accretion contributes to a total luminosity

$$L_{\nu_e+\bar{\nu}_e}^{\rm acc} \sim \frac{G M_{\rm PNS} \dot{M}_{\rm acc}}{R_{\rm PNS}}, \tag{2.4}$$

where $\dot{M}_{\rm acc}$ is the accretion rate of materials through the stalled shock and $M_{\rm PNS}$ and $R_{\rm PNS}$ are respectively the mass and radius of the PNS.

The stalled shock wave can be revived by energy deposition of the neutrinos and anti-neutrinos, in particular, from the core component discussed above. As they diffuse out of the neutrino spheres, a small fraction of them may re-interact with matter in the so-called gain layer behind the shock front. Such energy deposition is realized predominantly by the reverse reaction of Eq. (2.2) with ν_e and $\bar{\nu}_e$ since the absorption of other non-electron type of neutrinos and anti-neutrinos is forbidden kinematically. In the post-shock region, the neutrino cooling rate[4] drops much faster than the neutrino heating rate does with respect to the radial distance. As a result, there exits a crossing point [3, 28] where these two rates are equal. The gain layer is therefore defined between this crossing point and the shock front; materials in this layer gain energy over time as the name suggests. The stalled shock will eventually be refueled by such energy deposition and successfully expel infalling materials, leaving behind the hot PNS yet to be cooled down.

[3] Neutrino sphere is a boundary accross which the propagation of neutrinos transitions from diffusion to free streaming.

[4] The cooling rate is the rate at which materials lose energy by emitting neutrinos. Similarly, the heating rate is the rate at which materials gain energy by absorbing neutrinos.

2.1.3 Cooling Phase

Compared to the ν_e burst and the accretion phase, the cooling phase takes place over a much longer time scale (up to ~ 10 seconds). During this phase, a large fraction of the gravitational binding energy as well as the electron lepton number will be carried away from the PNS by thermal neutrinos produced from processes in Eq. (2.1)-(2.2). During this phase, the luminosities of neutrinos and anti-neutrinos of all flavors are approximately identical in magnitude. Moreover, an energy hierarchy

$$\langle E_{\nu_e} \rangle < \langle E_{\bar{\nu}_e} \rangle \approx \langle E_{\nu_x} \rangle \approx \langle E_{\bar{\nu}_x} \rangle \tag{2.5}$$

is followed because ν_e has the largest neutrino sphere radius as a result of its additional charged current interaction (the reverse reaction of Eq. (2.2)) and the abundance of neutrons in the partially deleptonized PNS.

In summary, Fig. 2.1 illustrates the neutrino luminosities with two progenitor-mass models. We note that the magnitude and timing of the ν_e burst are independent of the progenitor mass as the physical conditions for the collapse-and-bounce process are the same. Heavier progenitor mass, however, corresponds to a prolonged accretion phase. Elevated level of ν_e and $\bar{\nu}_e$ luminosities during the accretion phase can also be observed from Fig. 2.1. In the next section, we will briefly discuss the latest status of current SN simulation.

2.2 Latest Computer Simulation Models

For predicting experimental signals of neutrinos from a core-collapse SN event, a long-term evolution of luminosity with spectral information for all neutrino species is desirable. This means that the simulation model must include both the accretion phase and the cooling phase. So far, only models from one-dimensional (1D) simulations can fulfill this requirement as multi-dimensional (2D or 3D) simulations are computationally expensive and usually limited to the first second or so after core-bounce. However, the major shortcoming of a 1D simulation model

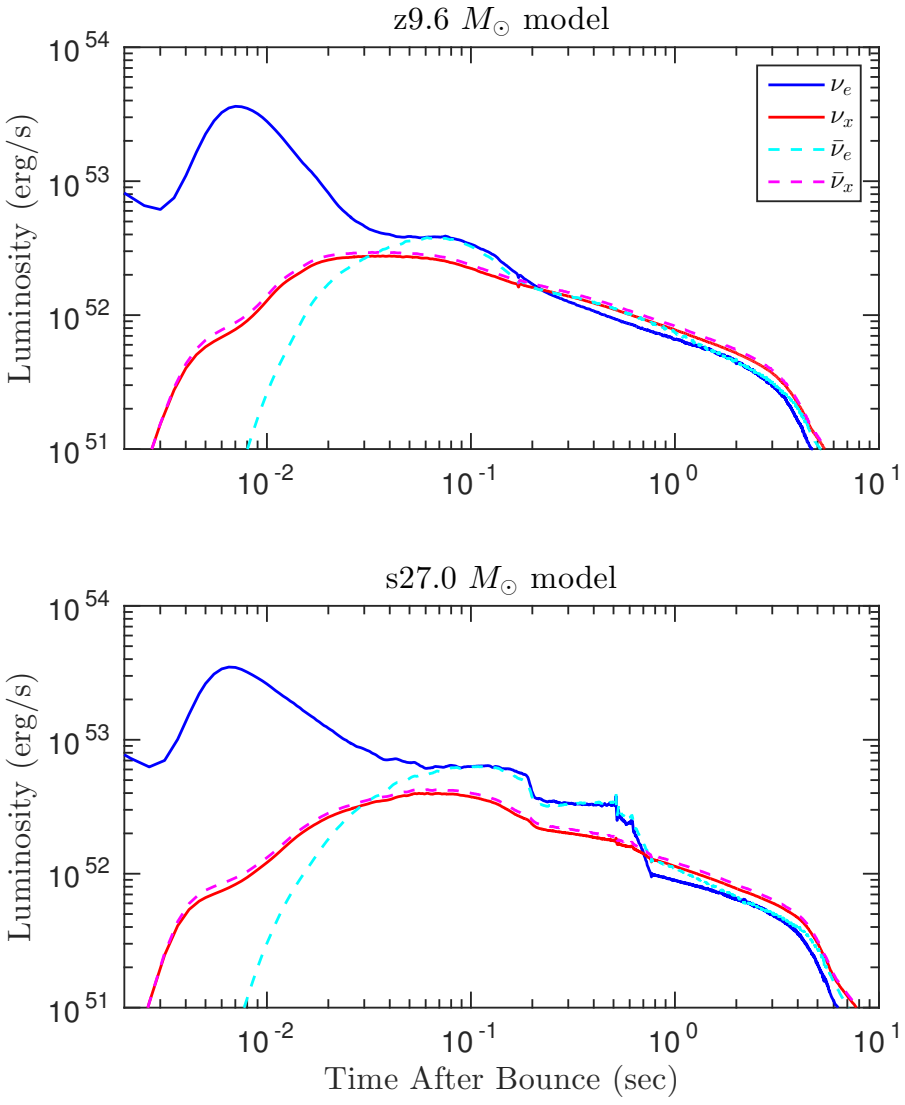

Figure 2.1: The luminosities of neutrinos and anti-neutrinos of (top) a z9.6 $M_\odot$ model and (bottom) a s27.0 $M_\odot$ model from [30]. These are also part of the models we will perform goodness-of-fit test with the SN1987A data in Chap. 3. The flavor index "x" represents either muon or tau flavor since they have the same luminosity and energy spectrum. The peak of the ν_e burst of both models can be seen at $t \approx 6$ msec. The explosion takes place at $t \approx 0.13$ sec in the z9.6 $M_\odot$ model and at $t \approx 0.5$ sec in the s27.0 $M_\odot$ model.

has been its underlying assumption of spherical symmetry of the explosion which is commonly observed, in multi-D simulations, to be violated by convective flows and non-radial deformation modes of the standing shock. These multi-D phenomena have been found to assist the revival of the shock wave (see [31] and references therein). Without such assistance, self-consistent explosion in 1D simulations can only be achieved with a small progenitor mass ($M \lesssim 10M_{\odot}$) which has minimal mass shells overlying the stalled shock wave; for slightly massive progenitors, the explosion has to be triggered artificially.

It was only until recently that the convection effect was implemented by Mirizzi et al. [30] with a mixing length treatment in a long-term 1D hydrodynamic simulation, which produced results consistent with their 2D counterpart. In addition to the assistance in shock revival, it was found that convective flows in the interior of the PNS can also expedite deleptonization and cooling. As the observable neutrino signals are largely contributed by the emission during the cooling phase, the importance of testing these latest simulation models with the SN1987A event, which is the only SN explosion event observed in terms of neutrinos so far, cannot be overstated. For a comparison with the historical SN1987A data in Chap 3, we obtain from the authors of [30] the neutrino emission profiles of two mass models, $9.6M_{\odot}$ with zero metalicity and $27.0M_{\odot}$ with solar metalicity. The profiles[5] of anti-neutrinos from these models are of relevance to analyzing the SN1987A data and they are summarized in Fig. 2.2. Each of these progenitor masses has been simulated with two nuclear equations of state (EOSs) abbreviated as "LS220" [32] and "SHFO" [33]. These EOSs have been widely implemented in simulations over recent years and yet there remains theoretical uncertainty in nuclear physics at supranuclear densities. The LS220 EOS is a "softer" EOS compared to the SFHO EOS. A softer EOS generally allows faster contraction of the PNS which in turn

[5] These 1D simulations terminate somewhere between 11 seconds and 17 seconds after core-bounce. To accommodate the time span of the full KAM-II data set in our analysis, we extrapolate the neutrino number luminosity, mean energy, and root mean square energy until $t = 24$ seconds by fitting the last 0.1 seconds of each quantity with an exponentially decaying function. Such extrapolation contributes very little to the total expected number of events in both the KAM-II and IMB detectors but will be essential for our goodness-of-fit method.

leads to faster release of gravitational binding energy. The effect of different EOS appears more significant as the cooling of the PNS follows distinct trajectory at late time as shown in Fig. 2.2 and the implication will be discussed in Chap. 3.

2.3 Detection of Supernova Neutrinos

Taking the simulation models discussed in the last section at face value, we discuss the experimental signals of SN neutrinos in a water Cherenkov detector. Specific experimental settings relevant to the Kamiokande-II (KAM-II) experiment [34, 35] and the Irvine-Michigan-Brookhaven (IMB) experiment [36, 37] will be assumed with an intention for making a comparison between the SN simulation models and the SN1987A data sets from the two experiments later in Chap. 3.

2.3.1 Relevant Channels of Water Cherenkov Detector

SN neutrinos and anti-neutrinos have energies of order ~ 10 MeV. At such energy scale, the relevant targets for them to interact with in water are electrons, protons, and oxygen nuclei. The interaction rate is dominated by the inverse beta decay (IBD) process

$$\bar{\nu}_{\mathrm{e}} + \mathrm{p} \rightarrow \mathrm{e}^{+} + n, \tag{2.6}$$

whereas other interactions

$$\begin{aligned} \nu + e^{-} &\rightarrow \nu + e^{-} \\ \bar{\nu} + e^{-} &\rightarrow \bar{\nu} + e^{-} \\ \nu_e + {}^{16}\mathrm{O} &\rightarrow e^{+} + {}^{16}\mathrm{F} \\ \bar{\nu}_e + {}^{16}\mathrm{O} &\rightarrow e^{+} + {}^{16}\mathrm{N} \end{aligned} \tag{2.7}$$

have much smaller cross sections [38, 39]. After accounting for the relative abundance of the targets in water, the processes shown in Eq. (2.7) do not contribute

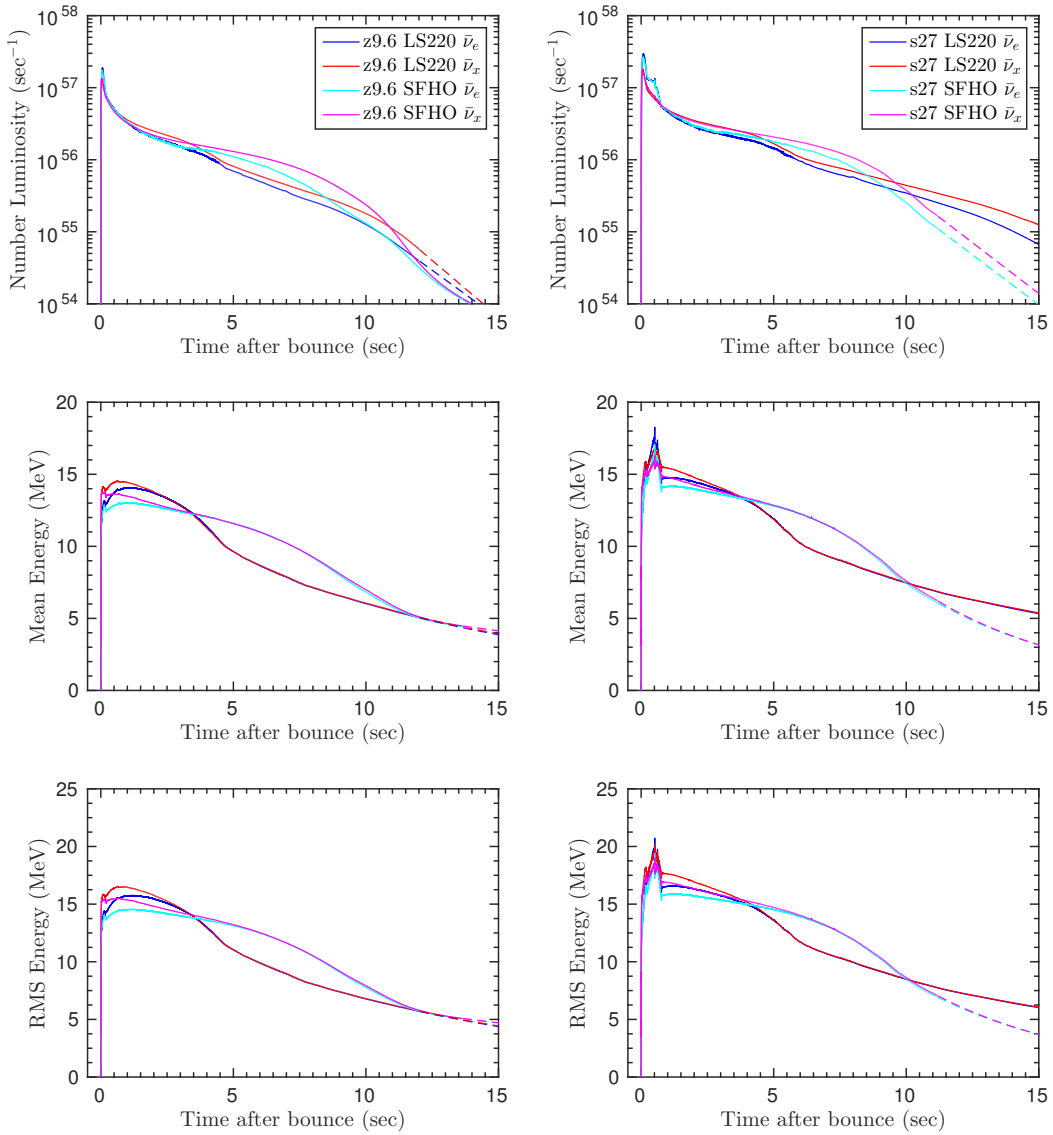

Figure 2.2: The emission profiles of anti-neutrinos from the z9.6 (left) and s27.0 (right) models from [30]. Blue (cyan) and red (magenta) curves represent $\bar{\nu}_e$ and $\bar{\nu}_x$ ($x = \mu$ or τ) from the LS220 (SFHO) model, respectively. The top, middle, and bottom figures are respectively the number luminosity, the mean energy, and the root mean square energy of anti-neutrinos at $R = 500$ km from the PNS core. Dashed part of each curve represents the extrapolation of the original simulation data. The curves are plotted up to $t = 15$ seconds in this figure and extrapolated up to $t = 24$ seconds for the goodness-of-fit analysis in Chap. 3.

to more than 10% of the interaction rate in the relevant energy range. Therefore, these subdominant channels will be neglected from our analysis.

In the IBD process, the recoil energy of the neutron is negligible and thus

$$E_\nu \approx \Delta + E_e, \tag{2.8}$$

where $\Delta \equiv m_n - m_p \approx 1.3$ MeV. This approximate relation allows the reconstruction of $\bar{\nu}_e$ energy by measuring the positron energy. The IBD interaction rate in the detector can be expressed as

$$\frac{\mathrm{d}^2 N_{int}}{\mathrm{d}t\,\mathrm{d}E_\nu} = F_{\bar{\nu}_e}(E_\nu, t) \times \sigma_{\bar{\nu}_e p}(E_\nu) \times N_{\text{protons}}, \tag{2.9}$$

where $F_{\bar{\nu}_e}(E_\nu, t)$ is the energy-differential $\bar{\nu}_e$ flux at the detector, $\sigma_{\bar{\nu}_e p}(E_\nu)$ is the IBD cross section, and N_{protons} is the number of free proton in the detector mass (to be converted from 2.14 ktons of water in the KAM-II detector and 6.8 ktons in the IMB detector).

2.3.2 Quasi-thermal Spectra of Supernova Neutrinos

The spectra followed by neutrinos emerging from the SN are not thermal. The emerging spectrum is a superposition of spectra of neutrinos emitted from different regions in the PNS. In addition, the interactions of neutrinos with matter are also energy dependent. These factors can easily result in a non-thermal spectrum even if the neutrinos are originally emitted with a thermal distribution. To parameterize a non-thermal spectrum, the traditional way is to use a nominal Fermi-Dirac distribution [40]

$$f(E_\nu) = \frac{1}{T_\nu^3 F_2(\eta_\nu)} \times \frac{E_\nu^2}{\exp\left(\frac{E_\nu}{T_\nu} - \eta_\nu\right) + 1}, \tag{2.10}$$

where T_ν is the effective neutrino temperature, η_ν is a degeneracy parameter in place of the chemical potential term in the canonical Fermi-Dirac distribution, and the complete Fermi-Dirac integral is defined as

$$F_n(\eta) \equiv \int_0^\infty \mathrm{d}x\, \frac{x^n}{[\exp(x - \eta) + 1]}. \tag{2.11}$$

The relation between the neutrino energy moments and the spectral parameters, T_ν and η_ν, can be expressed as

$$\begin{aligned} \langle E_\nu \rangle &= \frac{F_3(\eta_\nu)}{F_2(\eta_\nu)} \times T_\nu \\ \langle E_\nu^2 \rangle &= \frac{F_4(\eta_\nu)}{F_2(\eta_\nu)} \times T_\nu^2. \end{aligned} \tag{2.12}$$

The above relation suggests that fitting the spectral parameters from an "empirical" energy distribution observed in a simulation is not so straightforward.

An alternative fitting formula has been proposed in [41]. With the two lowest order energy moments, $\langle E_\nu \rangle$ and $\langle E_\nu^2 \rangle$, the quasi-thermal spectrum can be described equally well by the α-fit formula [42, 41]

$$f(E_\nu) = \frac{1}{\langle E_\nu \rangle} \times \frac{[1+\alpha]^{1+\alpha}}{\Gamma(1+\alpha)} \times \left(\frac{E_\nu}{\langle E_\nu \rangle} \right)^\alpha \exp\left\{ -(1+\alpha) \times \frac{E_\nu}{\langle E_\nu \rangle} \right\} \tag{2.13}$$

, where the shape parameter, defined as

$$\alpha \equiv \frac{2\langle E_\nu \rangle^2 - \langle E_\nu^2 \rangle}{\langle E_\nu^2 \rangle - \langle E_\nu \rangle^2}, \tag{2.14}$$

determines the degree of "pinching" relative to a Maxwell-Boltzmann distribution ($\alpha = 2$) or a Fermi-Dirac distribution with zero chemical potential ($\alpha = 2.3$). Larger α value corresponds to a more pinched (narrowed) spectrum and vice versa. In addition to the mathematical convenience of allowing a direct conversion from the energy moments to the spectral parameters, α and $\langle E_\nu \rangle$, implied by Eq. (2.13)-(2.14), the α-fit formula can also characterize an anti-pinched spectrum to which Eq. (2.10) is not applicable. Nevertheless, a Monte Carlo study in [41] has found the instantaneous spectrum always pinched relative to a Maxwell-Boltzmann distribution with the typical range $2 \lesssim \alpha \lesssim 4$ for SN neutrinos.

2.3.3 Supernova Neutrino Fluxes

It is well established that neutrinos undergo flavor transformations as they propagate in vacuum or in matter [4]. While it is essential to account for this phenomena

in a rigorous analysis especially with sufficient event statistics, treating neutrino oscillations is unnecessary for our purpose and a brief rationale is as follows. Let the electron anti-neutrino flux observed at the detector to be $F_{\bar{\nu}_e}(E_\nu, t)$ and, with neutrino oscillations, it is contributed by the fluxes of anti-neutrinos of all flavors that emerge from the SN. These unoscillated fluxes are expressed as

$$F^0_\beta(E_\nu, t) = \frac{1}{4\pi D^2} \times L^{\rm num}_\beta(t) \times f_\beta(E_\nu, t), \tag{2.15}$$

where the flavor index $\beta \in \{\bar{\nu}_e, \bar{\nu}_\mu, \bar{\nu}_\tau\}$, D kpc is the distance between the SN and the Earth, $L^{\rm num}_\beta(t)$ is the number luminosity, and $f_\beta(E_\nu, t)$ is the normalized energy spectrum discussed in Sec. 2.3.2. Given the overall survival probability $P_{sur}(E_\nu)$ of an electron anti-neutrino which accounts for all possible flavor transformations on its way to the detector, the observed $\bar{\nu}_e$ flux can be expressed as [43]

$$F_{\bar{\nu}_e}(E_\nu, t) = F^0_{\bar{\nu}_e}(E_\nu, t) + [1 - P_{sur}(E_\nu)] \left[F^0_{\bar{\nu}_x}(E_\nu, t) - F^0_{\bar{\nu}_e}(E_\nu, t)\right], \tag{2.16}$$

where $\nu_x = \bar{\nu}_\mu$ or $\bar{\nu}_\tau$. The above equation suggests that $F_{\bar{\nu}_e}$ is less sensitive to the survival probability if both $F^0_{\bar{\nu}_e}$ and $F^0_{\bar{\nu}_x}$ fluxes are similar, as is the case implied by Fig 2.2. In view of this, we consider in this thesis only the simplest cases in which the survival probability is either 1 or 0. These two cases will be referred to, respectively, as "un-oscillated" and "fully oscillated" throughout the rest of the discussion. Along with the choice of SN progenitor mass (s27.0 vs z9.6) and EOS (LS220 vs SFHO) from the available simulation models, a number of eight possible combinations of these "ingredients" will be compared to the SN1987A data in the next chapter.

2.3.4 Experimental Issues with Cherenkov Detector

A few experimental issues have to be addressed before we can compare the simulation models with the SN1987A data.

Positron Detection

The detection of positron is not 100% efficient and precise. Once an IBD event occurs, the outgoing positron moves faster than the speed of light in water and, as a result, the Cherenkov radiation is emitted by the positron. Such radiation may not be detected with 100% probability by the photomultiplier tubes surounding the detector mass due to light attenuation and detector geomoetry. The probability of detecting the positron is termed detector efficiency which is a function of positron energy and location of the event. For simplicity, a volume-averaged detector efficiency $\epsilon(E_e)$ is often used. We take the fitting formulas for the KAM-II and IMB detector efficiency functions from [44]. These functions are plotted in Fig. 2.3, which implies that the two detectors were sensitive to different parts of the neutrino energy spectrum.

Besides, the true positron energy is linearly correlated with the number of photomultiplier tube hits, which is to be multiplied by a proportionality factor to obtain an observed (best-fit) positron energy E_e^{obs}, and this number is subject to statistical fluctuations. Consequently, one must fold the finite energy resolution of the detector with the interaction rate from Eq. (2.9) when deriving the detector counting rate. In regards to this, we adopt in our theoretical calculation a smearing function of Gaussian form with a volume-averaged energy resolution

$$\sigma_E = \alpha\sqrt{\frac{E_e}{\text{MeV}}}, \tag{2.17}$$

where we use the same values, $\alpha = 0.87$ MeV for the KAM-II detector and $\alpha = 1.16$ MeV for the IMB detector, as in [45, 46]. We remark that this KAM-II detector resolution is more conservative (up to 20% larger α value) than was reported in [47]; however, the choice of detector resolution has minimal effect on the goodness-of-fit results to be presented in the next chapter.

Background Event Rate

Excess events above normal background level were observed in the KAM-II and IMB experiments as well as the Baksan [48] experiment at about the same time

within their reported absolute time uncertainties (see the discussion in Sec. 3.2). This correlation has led researchers to attribute the excess events to the SN1987A neutrino busrt. Among the three detectors, the Baksan detector had a background component that permeated the entire energy spectrum with a rate comparable to the SN neutrino signal rate. Therefore, the Baksan data set provides no discriminating power in our goodness-of-fit test in Chap. 3 and will neglected from our analysis. As for the KAM-II detector, we obtain the background rate over complementary energy ranges from both [49, 50] and [51], the later of which reported the experiment's solar neutrino measurement during the experimental phase when the SN1987A event occurred. The KAM-II background rate is summarized in Fig. 2.4. In addition, we emphasize that this rate is empirical and it already reflects the smearing effect from the finite energy resolution of the detector [52].

The KAM-II background rate peaked at around $E_e^{obs} = 6$ MeV according to Fig. 2.4 whereas the major SN neutrino signal was above $E_e \approx 8$ MeV where the detector efficiency exceeded 50%. This means that only those low energy events in the KAM-II data set could have been background. The general approach adopted by investigators to analyzing the KAM-II data set is to set an artificial threshold at $E_e^{obs} = 7.5$ MeV to reduce most of the background. To avoid holding prejudice against low energy events and to utilize the full information from the KAM-II data set, we will perform the goodness-of-fit test both with and without this conventional energy threshold in Chap. 3. On the other hand, the IMB data set can be viewed as background free because of its experimental capability to legitimately remove events deemed as background although the IMB detector did have an empirical background trigger rate of 2.7 Hz [53], mostly due to penetrating muons.

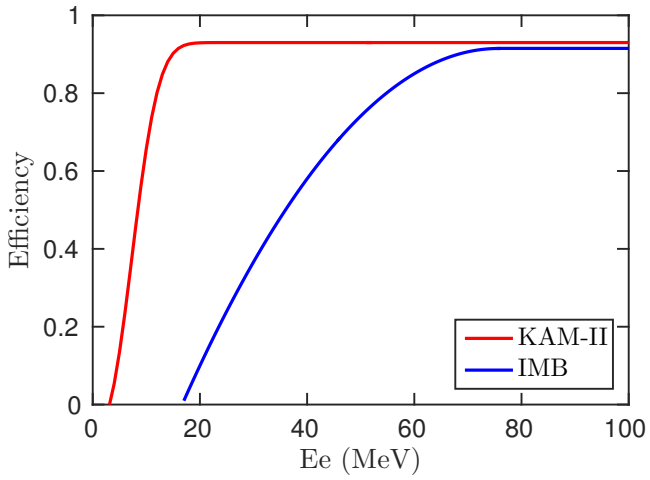

Figure 2.3: The efficiency curves of the KAM-II and IMB detectors as functions of positron energy.

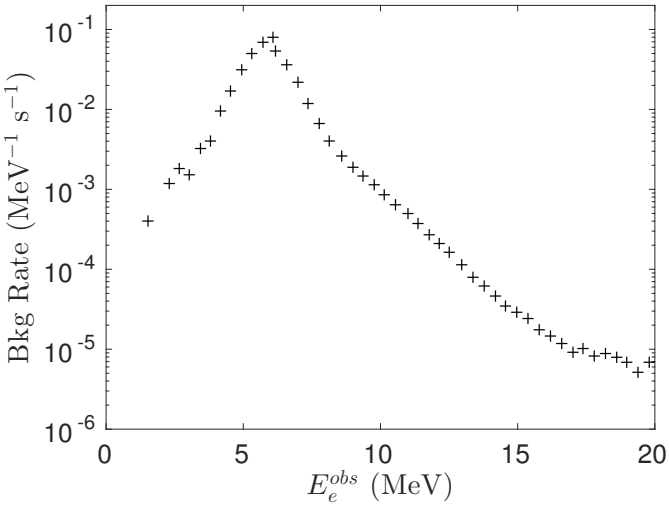

Figure 2.4: The empirical background rate of the KAM-II detector. For $E_e < 6$ MeV, the curve is taken from [49, 50] while, for $E_e \geq 6$ MeV, the curve is taken from [51]. Such background rate on average yields about 0.14 events per second over the entire energy domain and 0.01 events per second above the conventional threshold $E_e^{obs} = 7.5$ MeV.

Practical Detector Counting Rate

The detector counting rate, after accounting for the aforementioned characteristics of positron detection and background rate, can be expressed as [50]

$$\frac{\mathrm{d}^2 N_{count}}{\mathrm{d}t\,\mathrm{d}E_e^{obs}} = B(E_e^{obs}) + \int \mathrm{d}E_e \frac{\mathrm{d}^2 N_{int}}{\mathrm{d}t\,\mathrm{d}E_e} \times \frac{1}{\sigma_E\sqrt{2\pi}} \exp\left\{-\frac{(E_e - E_e^{obs})^2}{2\sigma_E^2}\right\} \times \epsilon(E_e), \tag{2.18}$$

where the true positron energy E_e has been substituted for E_ν in the interaction rate from Eq. (2.9) and $B(E_e^{obs})$ is the empirical background rate. For analyzing the IMB data set, we will simply set $B(E_e^{obs}) = 0$.

As a reference, Table 2.1 summarizes the total number of events computed by integrating Eq. (2.18) over time and over observed positron energy with each model. It is apparent that the total number of events depends strongly on the SN progenitor mass. One immediate concern to be raised is that the actual SN1987A progenitor mass lies between 9.6 $M_\odot$ and 27.0 $M_\odot$; a direct comparison between the numbers of events from Table 2.1 and the SN1987A observation (see Table 3.1) seems inappropriate. In the next chapter, we will discuss a method to assess the goodness-of-fit in terms of the events' distribution in time and energy.

	Un-oscillated				Fully oscillated			
	s27.0 LS220	s27.0 SFHO	z9.6 LS220	z9.6 SFHO	s27.0 LS220	s27.0 SFHO	z9.6 LS220	z9.6 SFHO
KAM-II (no threshold)	20.8	20.9	11.2	11.3	20.6	21.3	12.7	12.5
KAM-II ($E_e^{obs} \geq 7.5$ MeV)	17.4	17.5	7.9	7.9	17.2	17.9	9.4	9.2
IMB	9.8	8.7	3.1	2.6	11.2	10.7	4.9	4.1

Table 2.1: The predicted total number of events in the KAM-II and IMB detectors over a 24-second time window starting from the arrival of the SN neutrino flux. For the KAM-II detector, each of the tabulated numbers includes 3.4 background events (above and below the threshold) and 0.2 background events (above the $E_e^{obs} = 7.5$ MeV threshold) expected during such period. As for the IMB detector, the numbers only reflect the contribution from the SN neutrino flux and the dead-time effect is not considered.

Detector Dead Time

The IMB detector suffered from its 35 msec dead-time following each registered event. During such data acquisition period, no other events could be recorded and thus the detector counting rate was affected. A quick estimate using the aforementioned background trigger rate alone suggests a 90% live fraction; this fraction would be even smaller if the SN neutrino signal rate is comparable to or greater than the background rate. In fact, this is the case during the first second of the SN neutrino burst. Given the counting rate before dead-time adjustment as shown in Eq. (2.18), one could in principle use Poisson statistics to find the probability of observing no events during the dead-time window prior to a time of interest so as to find the expected instantaneous counting rate [54]. Then one would find the total number of SN neutrinos events discounted by a fraction ranging from 75% to 88% with the SN models shown in Fig. 2.2. However, we refrain from involving this complication in our analysis because the goodness-of-fit test to be discussed in the next chapter does not concern the total number of events but rather their probability distribution. Most importantly, the p-values from our tests with the IMB data set are large enough (above 10%) such that the correction from the dead-time effect does not have any statistical importance. We remark that a goodness-of-fit test that does compare the total number of events should properly treat such dead-time effect.

Chapter 3

Goodness of Fit with SN1987A Data

Valuable information was extracted from the limited statistics immediately after the epochal observation of neutrinos from SN1987A in the Large Magellanic Cloud to scrutinize stellar collapse models. A total of nineteen SN1987A neutrino candidate events observed in the KAM-II and IMB detectors confirmed the general theoretical expectations such as the Kelvin-Helmholtz cooling phase of a PNS lasting about 10 seconds, the PNS contracting to a radius of order 10 kilometers, and the SN neutrinos emitted with an average energy of order 10 MeV. More recently, follow-up analyses [49, 52] employing more sophisticated statistical methods suggested that SN1987A data favors the delayed scenario of SN explosion discussed in Sec. 2.1. These remarkable analyses were based on parametric emission models inspired by numerical simulations which were still under development back then. While inference of parameters can reveal important information in the data, this practice inevitably assumes that the observed events were due either to the physical processes implied by the parametric model or to the detector background. The lack of examination with reliable calculations from first principles could hinder a better understanding of SN1987A data.

In this chapter, we carry out a goodness-of-fit test of the 1D hydrodynamic

simulation models discussed in Sec. 2.2 with the historical SN1987A data. Our results indicate the poor fitting of the simulation models with the late-time events from the KAM-II data set. We discuss the implications of the poor goodness-of-fit and explore a fallback scenario in the SN1987A SN explosion.

3.1 Goodness-of-fit Methodology

As discussed in Sec. 2.1, a SN with a larger progenitor mass generally endures longer accretion phase. This means that more materials can be accreted onto the PNS thereby raising the luminosity and average energy of the neutrino emission from the accretion phase onward. Accordingly, more $\bar{\nu}_e$ events with a harder spectrum will be measured by the detector. The progenitor mass of SN1987A was determined to be in the range $16 \sim 22 M_\odot$[55]. Therefore, an assumption has to be made that the neutrino emission from an intermediate mass model, which is appropriate for describing SN1987A, is an "interpolation" between the 9.6 $M_\odot$ and 27.0 $M_\odot$ models we have in hand. More specifically, we assume that the double differential counting rate as shown in Eq. (2.18) – a 2D function of time and observed positron energy – of such model is bound between those rates of the 9.6 $M_\odot$ and 27.0 $M_\odot$ models. Based on this assumption, events observed at unlikely locations in the 2D time-energy domain in light of the 9.6 $M_\odot$ and 27.0 $M_\odot$ models will signify inconsistency between the SN simulation and the SN1987A neutrino data as we shall demonstrate with the following method.

As we have seen in Table 2.1, the expected total number of events also increase with the progenitor mass. We should avoid assessing the goodness-of-fit in terms of total number of events simply because the available mass models will either under- or over-produce $\bar{\nu}_e$ events compared to a simulation model with an intermediate progenitor mass. To remove the normalization factor of the counting rate that scales with progenitor mass from our analysis, we consider the probability density function (PDF) obtained by dividing the counting rate shown in Eq. (2.18) by the

predicted total number of events N_{tot} as listed in Table 2.1, i.e.

$$g(t, E_e^{obs}) \equiv \frac{1}{N_{tot}} \times \frac{\mathrm{d}^2 N_{count}}{\mathrm{d}t \, \mathrm{d}E_e^{obs}}. \tag{3.1}$$

Fig. 3.1 and Fig. 3.2 plot the PDFs of all the eight simulation models for the KAM-II and IMB detectors, respectively. For a visual comparison, each plot is overlaid with the SN1987A events which are also summarized in Table 3.1. These events are plotted without energy error bars since the PDFs to compare with are already probability distributions with respect to best fit energy. This allows us to justifiably use the best fit energies of the events without dealing with their uncertainty on an event-by-event basis. This philosophy will persist throughout the analysis in this chapter.

The goodness-of-fit of the above PDFs will be assessed by p-values in the following analysis. A p-value is a sum of probabilities of all statistically possible outcomes which are deemed as extreme as or more extreme than the observed outcome. A small p-value suggests that the observed outcome is an unlikely instance under the assumed model and that there is incompatibility between the model and the observed outcome. A high p-value, however, can only be interpreted as no evidence of incompatibility. Prior to computing the p-value, a test statistic must be chosen to quantify the degree of deviation from expectation. We choose the probability of an outcome as the test statistic for its conceptual simplicity and we will comment on an alternative choice of χ^2 metric later.

In the following discussion, a statistical outcome is defined to be a set of n events, each of which has a pair of coordinates in the 2D time-energy domain. In order to assign a nonzero probability to the outcome, we divide each of the time and energy domains into m equal intervals such that a 2D uniform grid with a number $k = m \times m$ of cells can be used to categorize these n events. Let x_i $(i = 1, 2, \ldots k)$ be the count of events in the $\mathrm{i_{th}}$ cell and, according to the multinomial distribution, the probability of such outcome is

$$Pr\,(x_1, x_2, \ldots, x_k) = n! \prod_{i=1}^{k} \frac{p_i^{x_i}}{x_i!}, \tag{3.2}$$

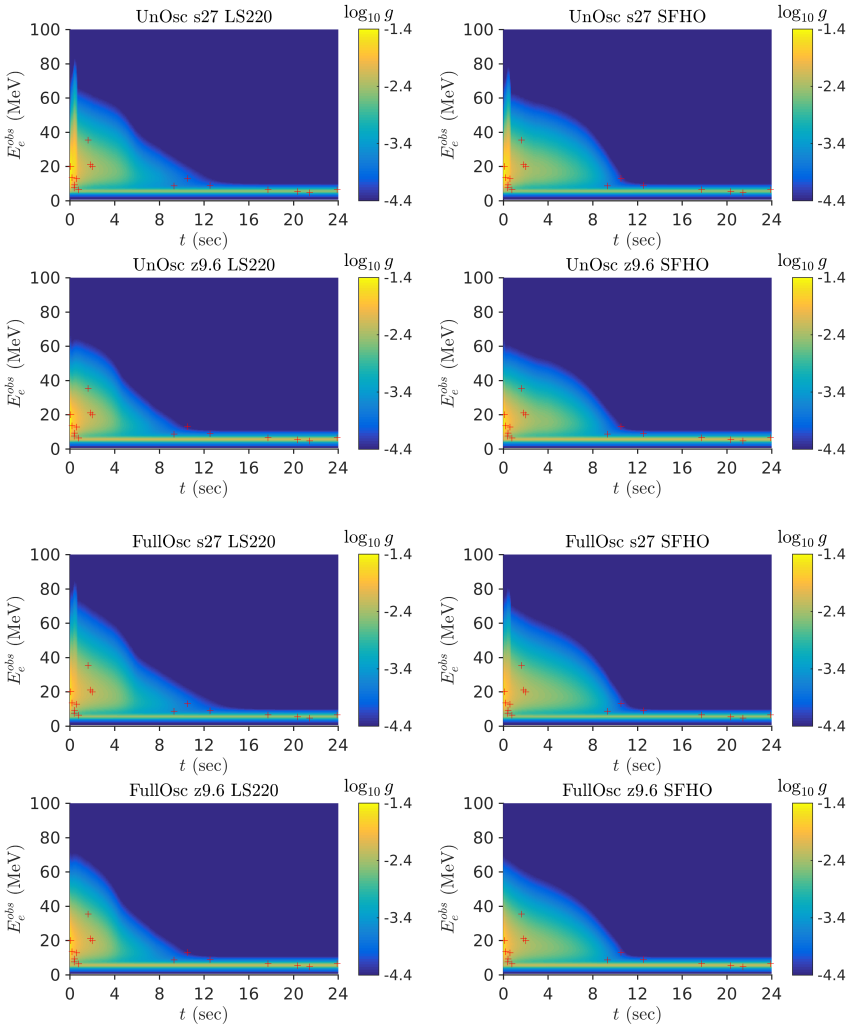

Figure 3.1: The normalized PDFs (in $\mathrm{MeV}^{-1}\mathrm{sec}^{-1}$) of all the eight combinations of progenitor mass, ν-oscillation condtion, and EOS with the KAM-II detector. The constant background component can be seen at the bottom (low energy) of each plot. The SN1987A neutrino candidate events along with the background events are overlaid as red crosses by assuming a 0.1-second time offset relative to the SN neutrino flux. For a better visual contrast, the color axis only covers three order of magnitude such that the dark blue color represents values more than a thousand times smaller than the maximum. It is clear that the events K10 through K12 locate at where both the SN neutrino signal and the static background are weak. The size of each red cross does not resemble measurement uncertainty.

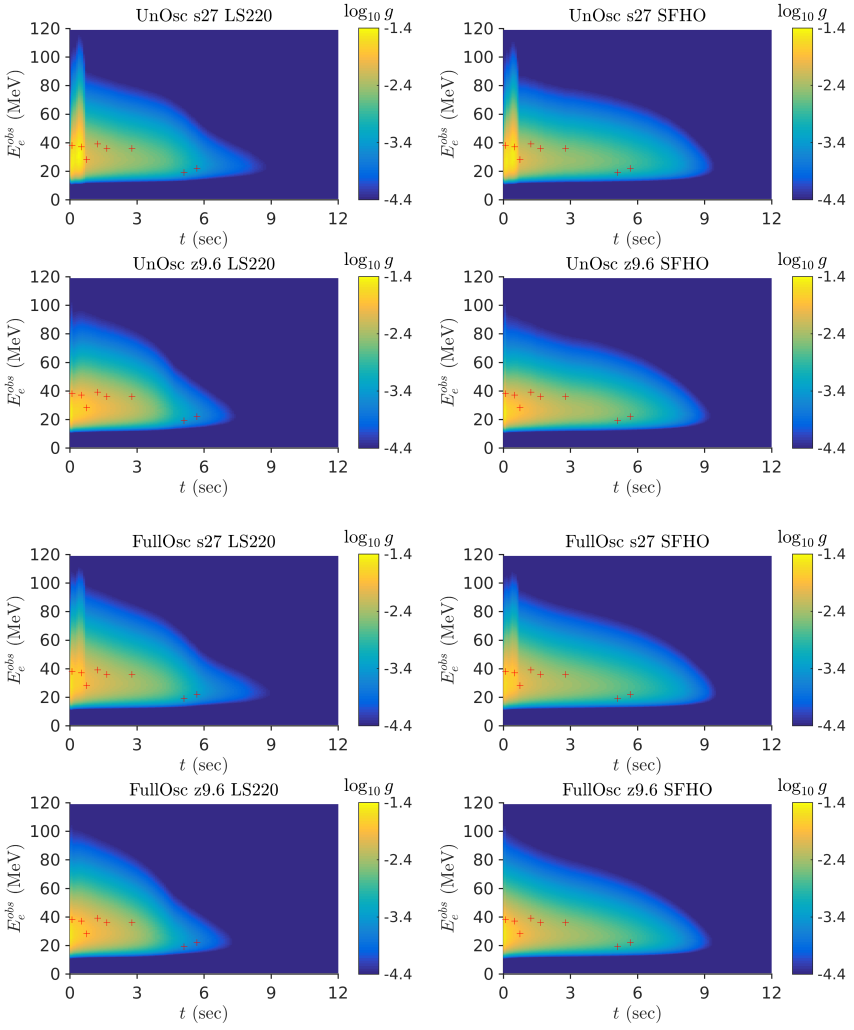

Figure 3.2: Similar to Fig. 3.1 but with the IMB detector. The background is not included since the IMB data set is already background free.

KAM-II				IMB			
Event #	t (sec)	E_e^{obs} (MeV)	σ_E^{rptd} (MeV)	Event #	t (sec)	E_e^{obs} (MeV)	σ_E^{rptd} (MeV)
K1	0.000	20.0	2.9	I1	0.000	38	7
K2	0.107	13.5	3.2	I2	0.412	37	7
K3	0.303	7.5	2.0	I3	0.650	28	6
K4	0.324	9.2	2.7	I4	1.141	39	7
K5	0.507	12.8	2.9	I5	1.562	36	9
K6	0.686	6.3	1.7	I6	2.684	36	6
K7	1.541	35.4	8.0	I7	5.010	19	5
K8	1.728	21.0	4.2	I8	5.582	22	5
K9	1.915	19.8	3.2				
K10	9.219	8.6	2.7				
K11	10.433	13.0	2.6				
K12	12.439	8.9	1.9				
K13	17.641	6.5	1.6				
K14	20.257	5.4	1.4				
K15	21.355	4.6	1.3				
K16	23.814	6.5	1.6				

Table 3.1: The SN1987A data sets from the KAM-II and IMB experiments. The time of each event is relative to the first event recorded by the respective detector. These experiments reported the energy uncertainty σ_E^{rptd} on an event-by-event basis, in addition to the observed positron energy.

where

$$p_i = \int\limits_{\mathrm{i}_{th}\ \mathrm{cell}} \mathrm{d}t\, \mathrm{d}E_e^{obs}\, g(t, E_e^{obs}). \tag{3.3}$$

The multinomial probability is maximized when $x_i \approx n \times p_i$ for all $i \in \{1, 2, \ldots, k\}$ [1] and therefore it can be used to quantify the deviation of the configuration, $(x_1, x_2, \ldots, x_k)$, from the underlying PDF. By definition, the p-value is can be computed by exhaustively enumerating through a number $H_n^k = \frac{(n+k-1)!}{n!(k-1)!}$ of statistically possible outcomes:

$$\text{p-value} = \sum_{\substack{x_1, x_2, \ldots, x_k \\ \sum_i x_i = n \\ Pr(\vec{x}) \leq Pr(\vec{x}_{1987A})}} Pr(x_1, x_2, \ldots, x_k), \tag{3.4}$$

where the reference probability $Pr(\vec{x}_{1987A})$ is computed from the observed data. The sparse events from the SN1987A data set makes such exhaustive enumeration possible with a coarse grid; however, the multiplicity soon becomes out of reach with a modern computer when the grid is refined.

An alternative way to compute the p-value is to use a Monte Carlo method with the following procedures:

1. Repeatedly sample a set of n events to realize a random outcome by using the acceptance-rejection method with the PDF.

2. Compute the multinomial probability of each realized outcome and compare with the multinomial probability of the observed data.

3. Calculate the occurrence frequency at which an equally or more extreme outcome is realized from the acceptance-rejection method.

For instance, if a total number N_0 of iterations are performed in the simulation and N_{extrme} outcomes are found to be equally or more extreme compared to the

[1] The equality is exact if $n \times p_i$ happens to be an integer for all i. In such case, it can be shown that any deviation, i.e. by moving one event from one bin to the other, from this optimal configuration results reduction in the multinomial probability.

SN1987A observation, then the p-value is estimated by the ratio N_{extrme}/N_0. Such occurrence frequency can be demonstrated to converge, after a sufficiently large number of iterations, to the p-value computed via Eq. (3.4). The uncertainty in the estimated p-value can also be properly controlled. Suppose the true p-value is p_{true} and then it is expected that a number $N_0 \times p_{\text{true}}$ of equally or more extreme outcomes will be sampled in the simulation. The actual number observed in the simulation has an uncertainty of order $\delta N_{\text{extrme}} \sim \mathcal{O}\left(\sqrt{N_0 p_{\text{true}}}\right)$. Therefore, the uncertainty in the estimated p-value is of order $\mathcal{O}\left(\sqrt{p_{\text{true}}/N_0}\right)$. For a p-value at percent level, i.e. $p_{\text{true}} \sim 10^{-2}$, and one million iterations, the uncertainty is estimated to be $\delta p_{\text{true}} \sim 10^{-4}$.

We make two additional comments on the above p-value method. Firstly, without imposing any condition, the number of events found in each cell follows a Poisson distribution, with a mean computed by integrating Eq. (2.18) over the cell area, and so does the sum of counts from all the cells. Since we do not concern the goodness-of-fit to the total number of events but rather the distribution of the events, the set of statistically possible outcomes is limited to those with a fixed sum of events. It is shown in Appendix A that the distribution of the cell counts conditional on a fixed sum actually reduces to the multinomial distribution shown in Eq. (3.2). Secondly, we could have chosen

$$\chi^2 \equiv \sum_{i=1}^{k} \frac{(x_i - np_i)^2}{np_i}, \tag{3.5}$$

where the same notations as in Eq. (3.2) and Eq. (3.3) are used, as the test statistic instead of the multinomial probability. Note that Eq. (3.5) is a χ^2 metric with a fixed sum of events. If the observed SN1987A events were numerous enough such that each cell has more than five events, this statistic would follow a χ^2-distribution with $k-1$ degrees of freedom [56]. This desirable χ^2-distribution is, however, not applicable to the small data set and the computation of p-value must be done with the aforementioned exhaustive enumeration or Monte Carlo method. Nevertheless, both choices measure the deviation of the cell counts from the assumed PDF equally well and result in very similar p-values.

3.2 Time Offset for the Data Sets

The relative time between events in the KAM-II and IMB data sets was accurately measured to better than 1 msec, but, unfortunately, the absolute time in the KAM-II experiment was not properly calibrated at the time of the SN1987A neutrino burst. The first KAM-II event was recorded at 7:35:35 UT $\pm$ 1 min, while the first IMB event was observed at 7:35:41.37 UT $\pm$ 0.05 s. There could be a brief yet unknown delay of the first event relative to the incoming SN neutrino flux and such delay could be different in the two detectors due to the random nature of particle detection (a Poisson process). This can potentially affect our goodness-of-fit test results since, as the time offset is varied, the way the observed events is categorized into the cells on the 2D grid will be shifted along the time dimension, thereby affecting the reference probability $Pr(\vec{x}_{1987A})$ and, consequently, the p-value according to Eq. (3.4). It is therefore essential to have a reasonable estimate of the time offset prior to computing the p-value.

Let us define the arrival time of the SN neutrino flux at the detector to be the time origin, as already implied in Fig. 3.1 and Fig. 3.2, and define t_1 to be the time of the first event relative to this time orgin. Given n events to randomly distribute according to the 2D PDF defined in Eq. (3.1), we would like to find a probability distribution, to be denoted as $h(t_1)$, of t_1 for further estimating the time offset. Since only the time is of relevance here, we integrate Eq. (3.1) over the energy dimension to obtain a 1D PDF of time

$$\tilde{g}(t) = \int \mathrm{d}E_e^{obs}\, g(t, E_e^{obs}) \tag{3.6}$$

obeyed by these n events. A trivial yet crucial observation is that there is no event observed before the so-called first event. The probability of observing no events before some time t, hence observing all n events after the time t, can be derived from the binomial distribution, namely

$$Pr(\text{no event before t}) = \left[1 - \int_0^t \mathrm{d}t' \tilde{g}(t')\right]^n . \tag{3.7}$$

The difference between the probability of observing no events before t_1 and the probability of observing no events before $t_1 + \mathrm{d}t_1$ is equal to the probability of observing the first event between t_1 and $t_1 + \mathrm{d}t_1$. It is then straightforward to show that the PDF of t_1 is

$$h(t_1) = n \left[1 - \int_0^{t_1} \mathrm{d}t' \, \tilde{g}(t') \right]^{n-1} \tilde{g}(t_1), \tag{3.8}$$

from which the expectation value, variance, and percentiles of t_1 can be computed. Eq. (3.8) is skewed toward $t_1 = 0$ with the standard deviation of t_1 comparable to its mean. Fig 3.3 shows the percentiles, at increments of 5%, of the time offset for the KAM-II and IMB data sets. Roughly speaking, the time offset is below 0.3 seconds and 0.6 seconds for the KAM-II and IMB data sets, respectively, on a 90% confidence level. The IMB data set has a larger time offset mostly due to its sparser events.

3.3 P-values

Following the methodology discussed earlier, we compute the p-values of all the eight models with the data sets listed in Table 3.1. For each p-value, the time offset corresponding to each data set and each model is applied to the event times. To maintain consistency, we use the same 2D domain for both the KAM-II and IMB data sets. The time and energy domains are set to be -0.001 sec $\leq t \leq 24$ sec and 1.5 MeV $\leq E_e^{obs} \leq$ 120 MeV, respectively. In computing the p-values with the conventional energy threshold applied to the KAM-II data set, the energy domain is reduced to 7.5 MeV $\leq E_e^{obs} \leq$ 120 MeV.

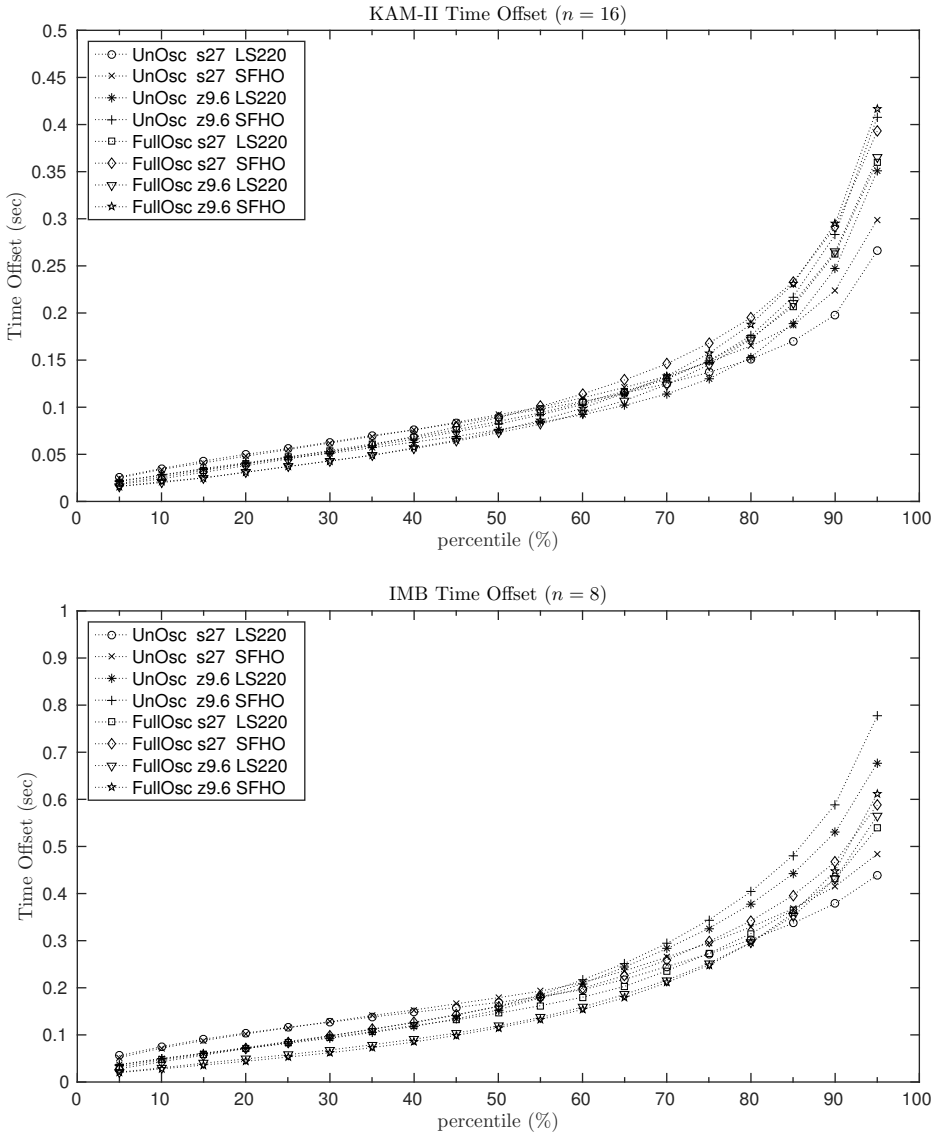

Figure 3.3: Percentiles of the time offset for (top) the KAM-II data set with 16 events and (bottom) the IMB data set with 8 events. For each model, 19 percentiles of the time offset are plotted.

	Un-oscillated				Fully oscillated			
Data Set	s27.0 LS220	s27.0 SFHO	z9.6 LS220	z9.6 SFHO	s27.0 LS220	s27.0 SFHO	z9.6 LS220	z9.6 SFHO
KAM-II (all events)	3.2%	3.8%	7.7%	14.2%	7.4%	7.0%	6.6%	16.2%
KAM-II ($E_{e,th}^{obs} = 7.5$ MeV)	4.9%	5.1%	6.6%	11.8%	8.7%	8.1%	5.7%	14.2%
KAM-II (w/o K10-12)	42.5%	55.2%	78.3%	84.5%	60.3%	68.5%	76.5%	86.3%
IMB (all events)	15.4%	39.6%	12.8%	53.2%	35.1%	63.5%	13.5%	57.2%

Table 3.2: The p-values of all the eight models with the indicated data sets. Each p-value is computed based on the median time offset corresponding to the model and the data set. The computation of this table uses a grid with 10^6 cells. The first row corresponds to the full KAM-II data set (16 events) without applying any energy threshold while the results after applying the 7.5 MeV threshold to the KAM-II data set are listed in the second row. This energy threshold reduces the KAM-II data set to 11 events. The third row demonstrates the improvement of p-values after removing the events K10 through K12 from the KAM-II data set (no threshold applied). The last row corresponds to p-values with the IMB data set.

The p-values computed with the median time offsets are summarized in Table 3.2. The p-values with the full KAM-II data set clearly indicate poor fitting by these SN simulation models. While p-values at the few-percent to ten-percent level are far from a firm rejection of the models and an extreme outcome could simply have been observed from the SN1987A burst by chance, the incompatibility between the KAM-II data set and the models is worthy of a closer examination. After applying the conventional 7.5 MeV threshold, we obtain p-values similar to those with the full KAMII-data set and this suggests that the events below the threshold (presumably background events) have no difficulty in agreeing with the background component in the models. In addition, as one can observe from Fig. 3.1, the three events K10, K11, and K12 seem difficult to be explained by either the background or the SN neutrino flux. Indeed, this observation is further confirmed by the dramatic improvement in the p-value after removing the three events from the data set. The removal of these three events also helps alleviate the tension between the KAM-II and IMB data sets as will be discussed in Sec. 3.4. Moreover, the p-values with the IMB data set slightly disfavor those models with the LS220 EOS. The events I7 and I8 were observed at the time when the two nuclear equations of state predict different cooling behavior of the PNS according to Fig. 2.2 and Fig. 3.2. Unfortunately, the sparse SN1987A events do not possess sufficient discriminating power for eliminating this theoretical uncertainty.

A number of issues have been examined to ensure that the above p-value results are reliable. The first among all is the time offset applied to the data set. In computing the p-value for each model, we apply those 19 time offset percentiles, as plotted in Fig 3.3, to the corresponding data set so as to gauge its dependence on the time offset. Fig. 3.4 shows such dependence by using the full KAM-II data set as an example. The p-values stay stable over most of the percentiles and only decline with extremely small or large time offset. Therefore, the p-values listed in Table 3.2 are approximately the maximum[2] p-values one can obtain with the models. Secondly, a series of grid refinement factors ($m =$

[2] So that a more conservative stance is taken in model rejection.

$10, 30, 100, 300,$ and 1000) have been applied to partitioning the 2D domain and the p-values are found to be stable with $m \gtrsim 300$ as shown in Fig. 3.5. Thirdly, the p-values are essentially estimated from sampling outcomes (sets of n events) via the Monte Carlo method as discussed earlier. We run the Monte Carlo simulation for one million iterations and this number is more than enough to ensure good convergence for p-values at percent level or above. Lastly, the electron flavor charged lepton emerging from the event K1 of the KAM-II data set was found to be in the forward direction[3] which is characteristic of an electron scattering process. Removing the event K1 as an electron scattering event from our analysis does not affect the p-values substantially.

3.4 Average Positron Energy

We have identified a subset of events from the KAM-II data set that causes poor goodness-of-fit. We elaborate on how this may shed light on the unresolved tension between the KAM-II and IMB data sets that has puzzled researchers. In the past, the sparse SN1987A events encouraged researchers to perform a simple maximum likelihood analysis with a time-integrated neutrino spectrum to infer the fluence and the average energy of the neutrino burst. As demonstrated in [57], consistent parameters cannot be fitted from a quasi-thermal spectrum between analyzes with the KAM-II set and with the IMB data set; the confidence interval from either analysis agrees only marginally with each other due to the fact that the average energy of events from the KAM-II data set was relatively low compared to that of the IMB events after accounting for different characteristics of the two detectors. This observation has led to a data-driven proposal for a bi-modal spectrum [49, 58] which consists of a low and a high energy peaks whose signals can be preferentially picked up by the KAM-II and IMB detectors, respectively. However, such proposal receives skepticism [57, 52] since the superposition of the

[3] The event K1 had an angle $\theta_{LMC} = 18 \pm 18$ degree [35] where the angle is defined with respect the direction pointing away from the Large Magellanic Cloud.

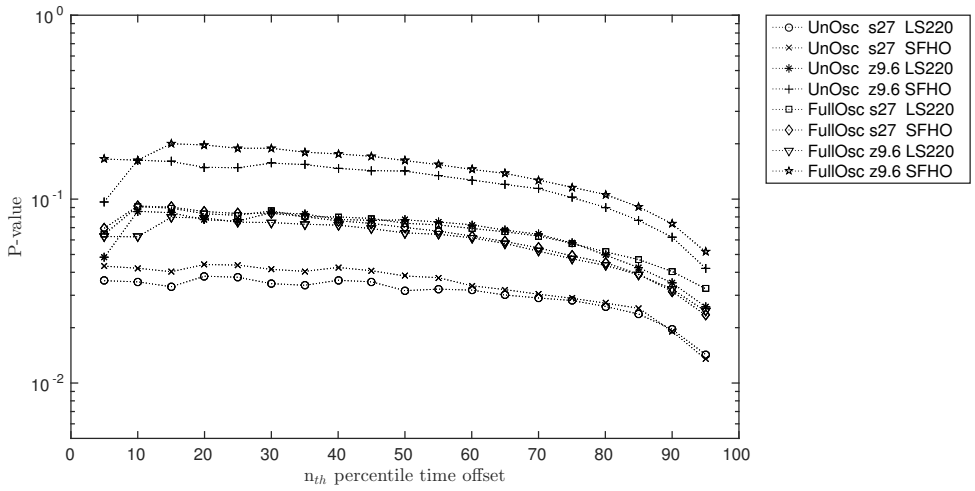

Figure 3.4: The dependence of p-value on the time offset. Each curve is computed with the full KAM-II data set using a grid with 10^6 cells.

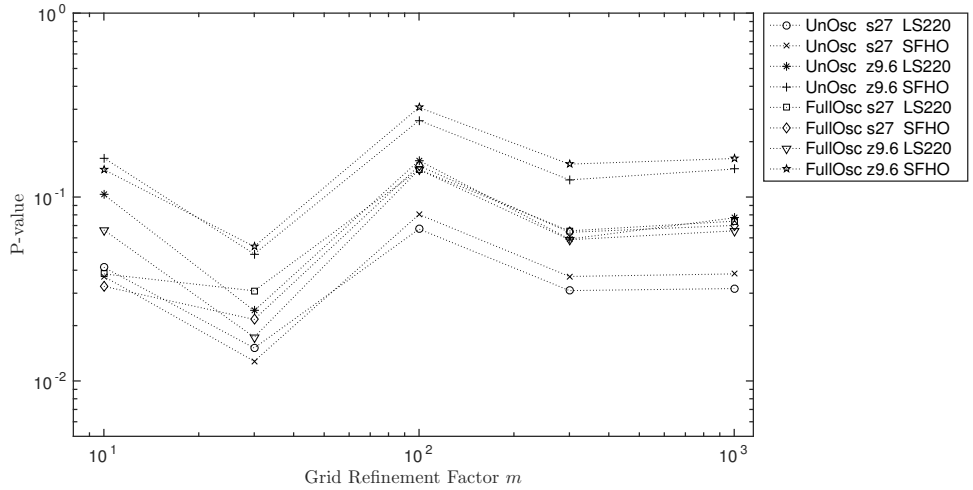

Figure 3.5: The p-values computed with a 2D grid with m^2 cells. Each curve is computed with the full KAM-II data set with a median time offset computed from the respective model.

instantaneous (and pinched according to [41]) anti-neutrino spectrum, of which the mean energy does not vary by more than 50% during the first few seconds, is most likely to result in a broadened quasi-thermal spectrum. Indeed, no evidence from the recent simulations [30, 59] suggests such bi-modal shape and the tension between the two data sets remains.

To measure the discrepancy between the data sets and the time-integrated spectra from the simulation models, we define a diagnostic indicator

$$\Delta E \equiv E_{\rm avg}^{\rm model} - E_{\rm avg}^{\rm data}, \tag{3.9}$$

where $E_{\rm avg}^{\rm model}$ is the average energy of n events sampled from the PDF of a simulation model and $E_{\rm avg}^{\rm data}$ is the average energy of n events from a data set. For a meaningful interpretation of ΔE, we briefly discuss the estimate of its uncertainty in the following. We note that $E_{\rm avg}^{\rm model}$ is a random variable whose expectation value and variance can be computed with the help of the time-integrated PDF

$$\bar{g}(E_e^{obs}) = \int {\rm d}t\, g(t, E_e^{obs}). \tag{3.10}$$

The expectation value of $E_{\rm avg}^{\rm model}$ is simply the average of the distribution, $\langle E \rangle \equiv \int {\rm d}E \times E \times \bar{g}(E)$, whereas its intrinsic variance stems from the finite sample size n and can be shown to be

$$Var[E_{\rm avg}^{\rm model}] = \frac{1}{n} \int {\rm d}E \times \bar{g}(E) \times (E - \langle E \rangle)^2, \tag{3.11}$$

which reduces to the variance of $\bar{g}(E)$ with $n = 1$ and approaches to zero as $n \to \infty$. On the other hand, the value of $E_{\rm avg}^{\rm data}$ is simply a constant that equals to the average of the best fit energies of the events. Once again, we stress that the PDFs already account for the finite detector resolution and we refrain from propagating the energy uncertainty from each individual event to ΔE. In fact, the PDFs shown in Fig. 3.1 and Fig. 3.2 are more "stretched" along the energy dimension compared to similar plots made without the smearing effect from finite detector resolution. Such smearing effect has already made additional contribution to $Var[E_{\rm avg}^{\rm model}]$ and therefore we ascribe the uncertainty of ΔE solely to the uncertainty from

$E_{\rm avg}^{\rm model}$. Moreover, in presenting the results of ΔE below, we have applied the 7.5 MeV threshold cut to the KAM-II data set and PDFs since, as we have shown in Table 3.2, those events below the threshold do not play an active role in the low p-values.

Fig. 3.6 summarizes the values of ΔE along with the corresponding uncertainty. We can observe that the average energy of the KAM-II data set is about 2σ lower than that expected from the models whereas, for the IMB data set, $\Delta E \approx 0$ within 1σ error. It is also clear that the tension exists between both data sets under the simulation models. Reconciliation between the two data sets can be achieved by removing the events K10-12 from the KAM-II data set, which have been identified to cause poor goodness-of-fit in the previous section. Such reduced KAM-II data set also exhibits a better agreement with the simulation models although the resultant ΔE is still more than 1σ above zero. Overall, larger progenitor mass and neutrino oscillations increase the value of ΔE since both factors increase the predicted energy of $\bar{\nu}_e$ flux observed on the Earth.

In summary, the analysis presented in this chapter so far suggests that the KAM-II data set cannot be easily explained by the state-of-the-art SN models shown in Fig. 2.2. The major issues are the relatively late timing of the events K10-12 as well as the average positron energy of the KAM-II data set being too low. We will discuss the implications of these results in the next section.

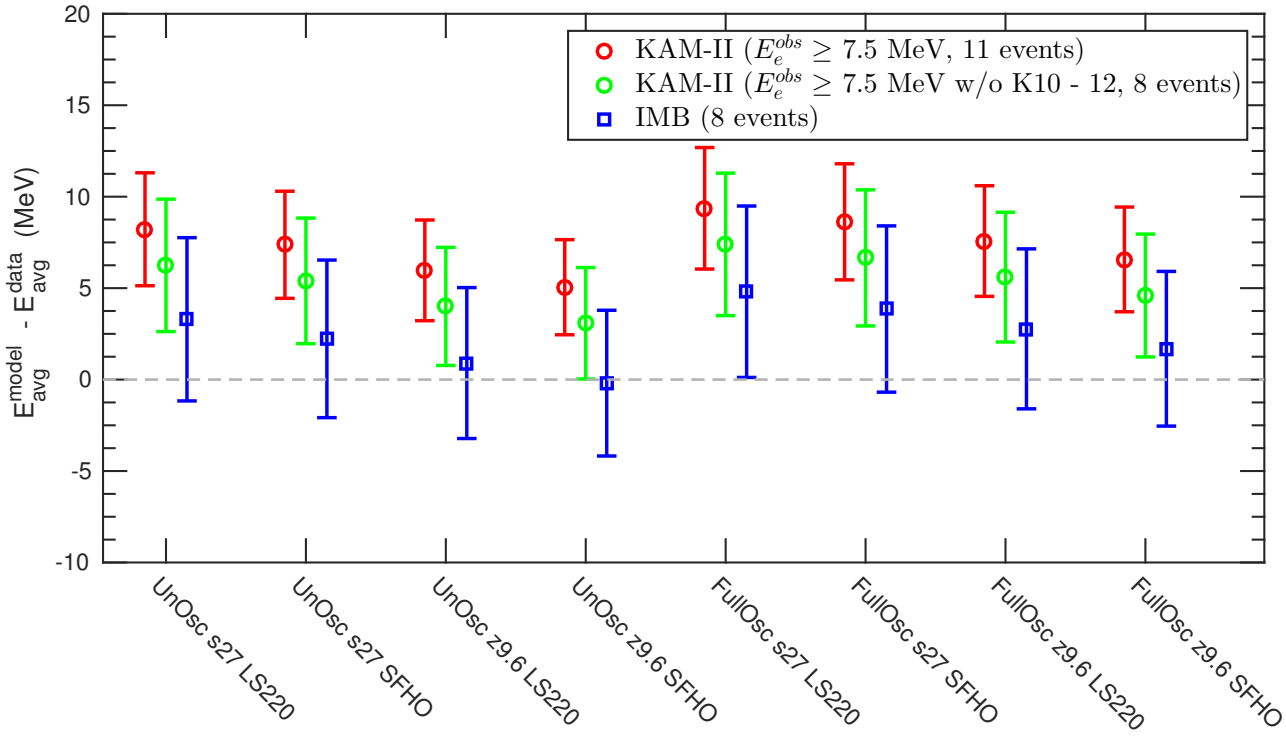

Figure 3.6: The discrepancy between the expected and observed average positron energy of n events. Each point represents a comparison between the indicated model and data set. The size of each error bar is the square root of $Var[E_{\text{avg}}^{\text{model}}]$ shown in Eq. (3.11).

3.5 Discussions

With the rather limited statistics from the SN1987A observation, it is hard to determine with certainty whether the poor agreement between the KAM-II data set and the simulation models is statistical or physical. However, if one assumes that the SN1987A observation was a statistically probable outcome, then there are clearly some physical implications. One conservative approach to bringing the simulation models to a better alignment with the KAM-II and IMB data sets, without subjectively removing any event, is perhaps to tune microphysics ingredients in the hydrodynamic simulation so as to slow down the cooling of the PNS. By having a slower cooling rate, not only can the events K10-K12 from the KAM-II data set as well as the events I6-I7 from the IMB data set be better accounted for by the SN neutrino flux but the average energy of the time-integrated neutrino spectrum can also be lowered. Factors like the EOS, neutrino opacities, convective instabilities can affect the cooling trajectory of the PNS and they are still subject to theoretical uncertainty to different extent. An attempt in this direction requires model adjustments made to prolong the cooling phase and lower the predicted average energy of observed events by a few MeVs without counteracting the efforts for achieving a successful SN explosion in the simulation. Nevertheless, this approach still leaves the existing tension between the KAM-II and IMB data sets unresolved.

Alternatively, we can take a more speculative stance to hypothesize additional neutrino production mechanism which is not included in the standard SN explosion paradigm to account for the late-time neutrino emission observed by the KAM-II experiment. It was pointed out in [60] that a fraction of the SN ejecta can be decelerated, become gravitationally bound, and then fall back onto the PNS within the first 10-15 seconds after the explosion is launched. The point was made by using an "energy-injected" explosion in the 1D simulation instead of a "piston-driven" explosion[4] [61] which the author of [60] argued to cause a delay and an

[4] These are two methods to artificially trigger the explosion in 1D simulations.

underestimate of the accretion rate of fallback mass. Moreover, multi-dimensional simulations [3] also predict asymmetric explosion whereby stellar materials, weakly ejected along some directions, fall back onto the PNS. Motivated by findings from SN simulations, we discuss one possible scenario in which the three events were contributed by fallback mass accreted onto the PNS.

To keep the analysis general, this late-time neutrino emission could be due to these materials falling directly onto the PNS surface or, if they had sufficient angular momentum, forming an accretion disk to spiral inward towards the PNS. Either way, the released gravitational binding energy could be transformed into neutrino luminosity. Despite extremely limited statistics, we perform a maximum likelihood analysis for the purpose of theoretical exploration of this scenario. To avoid involving the fallback dynamics in the following analysis, we consider only a time-integrated luminosity $\mathcal{I}_{\bar{\nu}_e}$ and a constant temperature $T_{\bar{\nu}_e}$ for the $\bar{\nu}_e$ flux observed on the Earth which is assumed to follow a Fermi-Dirac distribution, Eq. (2.10), with zero chemical potential such that $\langle E_\nu \rangle = [F_3(0)/F_2(0)] \times T_\nu \approx 3.15 \times T_\nu$. We also neglect the KAM-II background component since the duration of the emission due to fallback materials is not specified here. Then the counting rate can be obtained as a time-integration of Eq. (2.18) with the interaction rate replaced by

$$\frac{\mathrm{d}N_{int}}{\mathrm{d}E_\nu} = \frac{1}{4\pi D^2} \frac{\mathcal{I}_{\bar{\nu}_e}}{\langle E_{\bar{\nu}_e} \rangle} f_{FD}(E_{\bar{\nu}_e}, T_{\bar{\nu}_e}) \sigma_{\bar{\nu}_e p}(E_{\bar{\nu}_e}) N_{\text{protons}}. \tag{3.12}$$

Furthermore, we construct a combined likelihood function that takes both the KAM-II and IMB observations into account; the fallback component would contribute three events (or two if there was one background event) in the KAM-II detector and no event in the IMB detector. Since the number of observed events is of relevance here, a combined likelihood function $\mathcal{L}_{\text{combined}}$ is defined to be a

product of extended likelihood functions for the KAM-II and IMB observations:

$$\mathcal{L}_{\text{combined}} = \prod_{D\in\{\text{KAM-II, IMB}\}} \mathcal{L}_D, \text{ where}$$
$$\mathcal{L}_D = \frac{\lambda_D^{n_D}\exp\left(-\lambda_D\right)}{n_D!} \times \begin{cases} \prod_{i=1}^{n_D} \tilde{g}_D(E_i), & \text{if } n_D \geq 1. \\ 1, & \text{if } n_D = 0. \end{cases} \tag{3.13}$$

Each of the extended likelihood function has a Poisson probability component that depends on the expected total number of events λ_D and, for KAM-II in particular, a component consists of the normalized energy distribution function $\bar{g}_D(E)$, similar to that defined in Eq. (3.10), evaluated at the energies of the n_D events to assess the quality of energy fitting. Fig. 3.7 shows the best fit point obtained by maximizing Eq. (3.13) and the 1σ as well as 2σ confidence intervals in the $\mathcal{I}_{\bar{\nu}_e}$-$T_\nu$ parameter space. Due to the small sample size that renders asymptotic confidence intervals unfeasible, we use a Monte Carlo simulation to find the confidence intervals for the estimated parameters and the details are described in Appendix B. Since we have neglected the KAM-II background component, the analysis is also performed by removing one event, K12 for example, as a background event from the analysis.

The analysis suggests that the fallback scenario would require a significant amount of energy released in the form of low energy neutrinos. The inferred value of $\mathcal{I}_{\bar{\nu}_e}$ can be related to the mass of fallback materials M_{fallback} via

$$\mathcal{I}_{\bar{\nu}_e} = \kappa \times \frac{GM_{\text{NS}}M_{\text{fallback}}}{R_{\text{NS}}}, \tag{3.14}$$

where κ is a model-dependent conversion efficiency of gravitational binding energy into the observed integrated luminosity $\mathcal{I}_{\bar{\nu}_e}$. We remark that the most efficient conversion would occur if (1) the fallback materials fell directly onto the PNS surface releasing ν_e and $\bar{\nu}_e$ presumably in equal numbers via the forward reactions of Eq. (2.2) and (2) the anti-neutrinos were detected in the absence of neutrino oscillations. In such an ideal case, $\kappa = \frac{1}{2}$ and, by taking $M_{\text{NS}} = 1.4M_\odot$ and

$R_{\rm NS} = 10$ km, Eq (3.14) suggests a fallback mass

$$M_{\rm fallback} = 5.4 \times 10^{-3} \times \left(\frac{\mathcal{I}_{\bar{\nu}_e}}{10^{51}\ {\rm erg}} \right) \times M_\odot. \tag{3.15}$$

The best fit value of $\mathcal{I}_{\bar{\nu}_e}$ from Fig. 3.7 then corresponds to an amount of $0.3 M_\odot$ (or $0.1 M_\odot$ if one event was background) of fallback materials. We note that any departure from this idealized case would result in a smaller efficiency and thus more fallback mass is required to yield the observed luminosity. The period over which the fallback materials were accreted must be greater than the observed time interval spanned by the events K10-12. Such accretion rate could be a few times $10^{-2} M_\odot$ sec^{-1} and, within the uncertainty from parameter estimation, comfortably agree with the accretion rate of fallback matter estimated in [60]. One noticeable discrepancy, however, is the average energy of neutrinos: our parameter estimation suggests an average energy 3 MeV $\lesssim \langle E_\nu \rangle \lesssim$ 8 MeV (1σ range) whereas in [60] a rather high average energy $\langle E_\nu \rangle \gtrsim 20$ MeV was obtained. We comment that the conversion of gravitational binding energy of the fall back mass to neutrino luminosity is model-dependent and our results can serve as an observational constraint for future simulation study of the fallback scenario.

Due to the broad confidence intervals as a result of sparse data, the analysis presented here should be regarded as an invitation for more careful scrutiny. The timing and duration of materials falling back onto the PNS as well as the luminosity and effective temperature of the neutrino emission will have to be determined by self-consistent numerical simulations. As estimated above, the fallback mass could be a few times $10^{-1} M_\odot$ and potentially push the neutron star over the mass limit to become a black hole, the formation of which at the SN1987A remnant has been debated for the past decades. Properly understanding the potential experimental signature of fallback mass resulting from asymmetric explosion can also prepare us for the next galactic SN explosion.

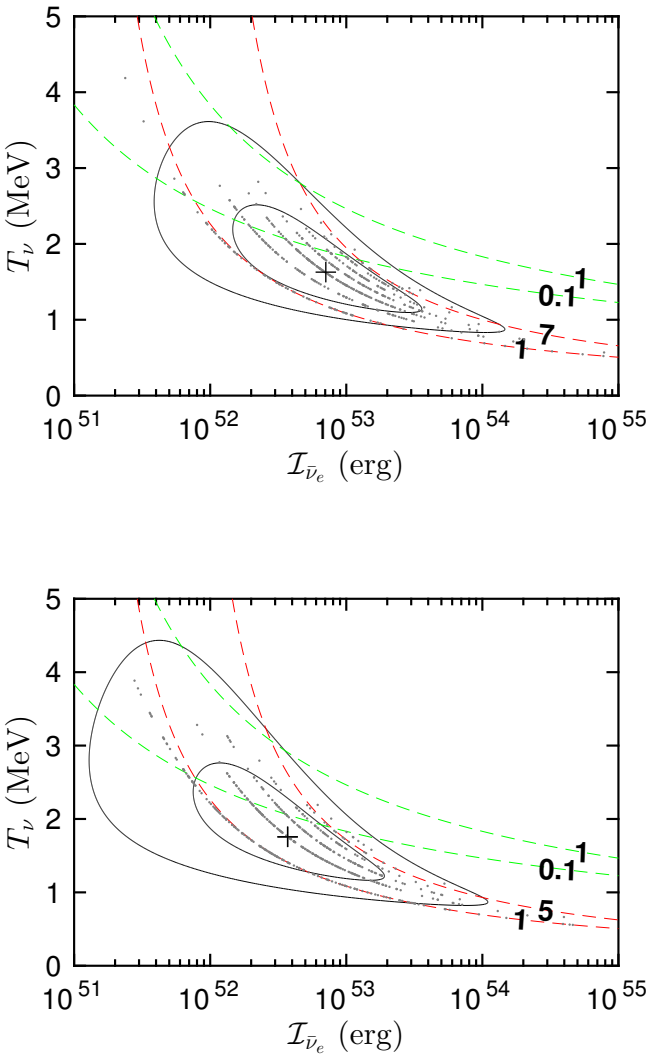

Figure 3.7: Maximum likelihood parameter estimation with the three events K10, K11, and K12 (top figure) or with only the two events K10 and K11 (bottom figure). The black cross represents the best fit point and two black solid contours are respectively 1σ and 2σ confidence regions. The gray dots are the best fit points with fake data sets sampled by Monte Carlo simulation (see Appendix B). For a better visual presentation, only five hundred iterations (gray dots) are plotted. To provide a goodness-of-fit assessment by eye, the red (green) dashed contours are overlaid to indicate the expected total number of events in the KAM-II (IMB) detector.

Chapter 4

Evolution of a 3D Gaussian Wave Packet

In this chapter, we present the methodologies for deriving the solution for a 3D Gaussian WP. For simplicity, we ignore neutrino masses and neglect neutrino oscillations although the neutrino mass term can be introduced in the derivations of the WP solution in this chapter and the quantum detection of WPs in the next chapter. In addition, to simplify mathematical formulas, we adopt natural units ($c = \hbar = 1$) throughout the following chapters. We also assume that the momentum distribution of the neutrino is sharply peaked around its mean momentum $\vec{k}_0$ so that the spinor part of the wave function is essentially an irrelevant constant factor. The initial 3D WP in our study is parameterized by its widths a_l and a_t in the longitudinal (propagating) and transverse directions, respectively. The assumption of sharp momentum distribution requires that the transverse and longitudinal momentum uncertainties be small compared to the mean momentum and, according to Heisenberg's uncertainty principle, this assumption is translated to the following inequalities:

$$k_0 a_l \gg 1 \text{ and } k_0 a_t \gg 1, \tag{4.1}$$

which will be frequently referred to in this chapter.

Suppose, at $t = 0$, the initial Gaussian WP is produced at the origin and it propagates along the z-axis. The wave function can be expressed as

$$\Psi(\vec{r}, 0) = \left[(2\pi)^3 a_t^4 a_l^2\right]^{-\frac{1}{4}} \exp\left(-\frac{\rho^2}{4a_t^2} - \frac{z^2}{4a_l^2} + ik_0 z\right), \tag{4.2}$$

where $\rho \equiv \sqrt{x^2 + y^2}$. It's well-known that this WP spreads as it evolves in time due to its intrinsic momentum uncertainty. A massless WP spreads only in the transverse direction and the angular size subtended by such WP can be estimated from the ratio of its transverse momentum uncertainty to its mean momentum. This simple estimate suggests that the angular size should be $\Delta k_\perp / k_0 \sim (2k_0 a_t)^{-1}$, as will be verified in the following sections where the time evolution of Eq. (4.2) is derived.

4.1 Fourier Transform Method

The approach commonly followed in the literature to finding the WP evolution is to decompose the initial wave function into a superposition of momentum eigenstates and then evolve these eigenstates with different frequencies [62, 63, 64, 65]. To begin with this approach, the Fourier transform corresponding to Eq. (4.2) must be obtained and it is

$$\tilde{\Psi}(\vec{k}) = (8\pi)^{\frac{3}{4}} a_t a_l^{\frac{1}{2}} \exp\left[-a_t^2\left(k_x^2 + k_y^2\right) - a_l^2\left(k_z - k_0\right)^2\right]. \tag{4.3}$$

As the WP evolves in time, each plane wave component of the WP acquires a different phase factor $\exp\left(-i\omega_{\vec{k}}\, t\right)$, where $\omega_{\vec{k}}$ is the energy of the plane wave. Therefore, the time evolution of Eq. (4.2) can be found from the inverse Fourier transform at $t > 0$

$$\Psi(\vec{r}, t) = \int \frac{\mathrm{d}^3\vec{k}}{(2\pi)^3}\, \tilde{\Psi}(\vec{k}) \exp\left(-i\omega_{\vec{k}} t + i\vec{k}\cdot\vec{r}\right). \tag{4.4}$$

With the sharp momentum distribution assumption, we can expand the energy-momentum relation around the mean momentum $\vec{k}_0 = (0, 0, k_0)$ up to quadratic

order [1]

$$\omega_{\vec{k}} \approx k_0 \left[1 + \frac{k_x^2 + k_y^2}{2k_0^2} + \frac{1}{k_0}\left(k_z - k_0\right)\right], \tag{4.5}$$

which allows the exponent of Eq. (4.4) to be expressed as a quadratic polynomial of the momentum variables. Upon completing the square for each momentum variable in the exponent, a closed-form expression of Eq. (4.4) can be derived by Gaussian integral. It follows that the evolved WP is found to be

$$\begin{aligned}\Psi(\vec{r},t) &= (2\pi)^{-\frac{3}{4}} \sigma_t^{FT}(t)^{-1} a_l^{-\frac{1}{2}} \\ &\times \exp\left[-\frac{x^2+y^2}{4a_t^2\left(1+\frac{it}{2k_0 a_t^2}\right)} - \frac{(z-t)^2}{4a_l^2} + ik_0\left(z-t\right) - i\zeta^{FT}(t)\right],\end{aligned} \tag{4.6}$$

where[2] the (squared) transverse width is defined to be

$$\sigma^{FT}(t)^2 \equiv a_t^2\left(1 + \frac{t^2}{4k_0^2 a_t^4}\right) \tag{4.7}$$

and the time-dependent phase is defined to be

$$\zeta^{FT}(t) \equiv \arctan\left(\frac{t}{2k_0 a_t^2}\right). \tag{4.8}$$

In addition, Eq. (4.6) corresponds to a probability density

$$|\Psi(\vec{r},t)|^2 = (2\pi)^{-\frac{3}{2}} \sigma_t^{FT}(t)^{-2} a_l^{-1} \times \exp\left[-\frac{x^2+y^2}{2\sigma_t^{FT}(t)^2} - \frac{(z-t)^2}{2a_l^2}\right], \tag{4.9}$$

which suggest that the WP moves along the z-axis at the speed of light ($c = 1$) and spreads in the direction transverse to the z-axis. Asymptotically, the transverse width $\sigma^{FT}(t) \sim t/2k_0 a_t$ which, combined with the distance traveled $z \approx t$, verifies that the angle subtended by the WP is $\sim 1/2k_0 a_t$.

---

[1] Eq. (4.4) applies to the massless case. In the case with nonzero mass, the approximated energy-momentum relation is found to be $\omega_{\vec{k}} \approx \omega_0\left[1 + \frac{k_x^2+k_y^2}{2\omega_0^2} + \frac{m^2}{2\omega_0^4}\left(k_z - k_0\right)^2 + \frac{k_0}{\omega_0^2}\left(k_z - k_0\right)\right]$, where $\omega_0 \equiv \sqrt{k_0^2 + m^2}$. The solution for a relativistic massive WP can be derived in the same way as discussed in this section.

[2] We use the superscript "FT" to denote the quantities derived from this Fourier transform method. These two quantities will be compared to those found from the paraxial wave equation method in the next section.

The solution we obtain above represents a WP with a "flat" shape that is stretched in the transverse direction. One paradoxical implication of such solution is the superluminal propagation of its edge and it has sparked discussions in the past [66, 67, 68]. While this approach may provide a satisfactory 1D solution, the discarded higher order terms in the expansion in Eq. (4.5) are, however, responsible for causing spherical curvature of the evolved WP [68]. Unfortunately, the inclusion of higher order terms can only allow the analytic solution to be found perturbatively with limited applicability. The spherical shape is not only required to comply with special relativity but it is also crucial for establishing wave-particle duality in the 3D space as we shall demonstrate. Therefore, an alternative approach will be pursued in the next section.

4.2 Paraxial Wave Equation Method

Inspired by the discussion in [67], we construct the desired WP solution using the paraxial solution from laser optics. Derived by making paraxial approximation to the wave equation, the paraxial solution describes a laser beam with a transverse Gaussian profile at the beam waist. Appendix C summarizes the derivation of the solution and the criteria for the paraxial approximation. In brief, the paraxial solution reads

$$\Psi_k(\vec{r},t) = \frac{A}{\sigma_t(t)} \exp\left\{-\frac{\rho^2}{4\sigma_t(z)^2} + i\left[\frac{k\rho^2}{2R(z)} - \zeta(z) + k(z-t)\right]\right\}, \tag{4.10}$$

where A is a normalization constant,

$$L_R \equiv 2ka_t^2 \tag{4.11}$$

is the Rayleigh range of the Gaussian beam,

$$R(z) \equiv z\left(1 + \frac{L_R^2}{z^2}\right) \tag{4.12}$$

characterizes the radius of curvature of the wavefront,

$$\sigma_t(z) \equiv a_t\sqrt{1 + \frac{z^2}{L_R^2}} \tag{4.13}$$

is a time-dependent transverse width, and

$$\zeta(z) \equiv \arctan\left(\frac{z}{L_R}\right) \tag{4.14}$$

is a position-dependent phase. Eq. (4.10) is valid under the condition $(ka_t)^2 \gg 1$, which is already guaranteed by the assumption of sharp momentum distribution as shown in Eq. (4.1).

As illustrated by Fig. C.1 in Appendix C, the paraxial solution is localized in the transverse direction but unconfined in the longitudinal direction. It behaves similarly to a plane wave along the z-axis, except for the additional phase $\zeta(z)$ which varies from 0 to $\pi/2$ as z increases from 0 to ∞. To construct a solution that is also localized in the z-direction from the paraxial solution, we recall that a 1D Gaussian WP is constructed by superposing plane waves weighted by a Gaussian distribution of the plane wave momentum. We therefore consider the following solution

$$\Psi(\vec{r},t) = \sigma_k^{-1} \int_{-\infty}^{\infty} \mathrm{d}k \, \exp\left[-\frac{(k-k_0)^2}{4\sigma_k^2}\right] \Psi_k(\vec{r},t), \tag{4.15}$$

where the k-width of the Gaussian distribution is chosen to be $\sigma_k = (2a_l)^{-1}$ from hindsight. The prefactor σ_k^{-1} is to ensure that $\Psi(\vec{r},t)$ has the same dimension as $\Psi_k(\vec{r},t)$. We caution that the implicit dependence on k of the quantities L_R, $\sigma_t(z)$, $R(z)$, and $\zeta(z)$ defined in Eq. (4.11)-(4.14) must be accounted for in the k-integration of Eq. (4.15). In the following discussion, boldface quantities, i.e. $\boldsymbol{R}(z)$, $\boldsymbol{\zeta}(z)$, $\boldsymbol{\sigma_t}(z)$ and $\boldsymbol{L_R}$ represent those with k set to be k_0, the central momentum of the Gaussian distribution in the integrand of Eq. (4.15).

To see that Eq. (4.15) is indeed a Gaussian WP at $t = 0$, we consider the approximations

$$\left.\begin{aligned} R(z) &\approx \frac{L_R^2}{z} \\ \zeta(z) &\approx 0 \\ \sigma_t(z) &\approx a_t \end{aligned}\right\} \text{ at the near-field limit } z \ll \boldsymbol{L_R}. \tag{4.16}$$

The phase term $ik\rho^2/2R(z) \lesssim \mathcal{O}(z/\boldsymbol{L_R})$ can then be neglected from Eq. (4.10) and the superposition in Eq. (4.15) reduces to a Gaussian integral which yields

$$\Psi_{\text{near}}(\vec{r},0) \approx \left[(2\pi)^3 a_t^4 a_l^2\right]^{-\frac{1}{4}} \exp\left(-\frac{z^2}{4a_l^2} - \frac{\rho^2}{4a_t^2} + ik_0 z\right), \tag{4.17}$$

where the normalization constant is now fixed as $A = 2^{-\frac{7}{4}}\pi^{-\frac{5}{4}} {a_l}^{-\frac{1}{2}}$ in order to satisfy the normalization condition $1 = \int \mathrm{d}^3\vec{r}\,|\Psi_{\text{near}}|^2$. We can see that, if $a_l \ll \boldsymbol{L_R}$, Eq. (4.17) is sufficient to describe the whole initial WP and thus Eq. (4.15) corresponds to the solution of the Gaussian WP. This additional assumption, $a_l \ll \boldsymbol{L_R}$, is equivalent to

$$k_0 a_l \ll (k_0 a_t)^2, \tag{4.18}$$

which not only allows the construction of WP solution from the paraxial solution but also simplifies the overlap model to be developed in Sec. 6.1.

Similarly, the evolution of the WP at $t \gg \boldsymbol{L_R}$ can be found by evaluating the superposition with the approximations

$$\left.\begin{aligned} R(z) &\approx z \\ \zeta(z) &\approx \frac{\pi}{2} \\ \sigma_t(z) &\approx \frac{z}{2ka_t} \end{aligned}\right\} \text{ at the far-field limit } z \gg \boldsymbol{L_R}. \tag{4.19}$$

Under this limit, Eq. (4.15) reduces, again, to a Gaussian integral

$$\Psi_{\text{far}}(\vec{r},t) = \frac{4a_l a_t A}{z}\int_{-\infty}^{\infty} \mathrm{d}k \times k \times \exp\left[\Omega(k)\right], \tag{4.20}$$

where the exponent

$$\begin{aligned} \Omega(k) &= -a_l^2\left(1 + \frac{a_t^2\rho^2}{a_l^2 z^2}\right)k^2 + \left[2k_0 a_l^2 + i\left(z + \frac{\rho^2}{2z} - t\right)\right]k - \left(k_0^2 a_l^2 + \frac{i\pi}{2}\right) \\ &\equiv \alpha k^2 + \beta k + \gamma \end{aligned} \tag{4.21}$$

is expressed as a quadratic polynomial of k with three complex coefficients α, β, and γ. Then a closed-form expression for Eq. (4.20) is found to be

$$\Psi_{\text{far}}(\vec{r},t) = \frac{(2\pi)^{-\frac{3}{4}} a_l^{\frac{1}{2}} a_t}{z} \times \frac{\beta \exp\left\{-\frac{\beta^2}{4\alpha} + \gamma\right\}}{(-\alpha)^{\frac{3}{2}}}, \tag{4.22}$$

where the exponent reads

$$-\frac{\beta^2}{4\alpha}+\gamma=-\frac{\left(z+\frac{\rho^2}{2z}-t\right)^2}{4a_l^2\left(1+\frac{a_t^2\rho^2}{a_l^2z^2}\right)}-\frac{k_0^2a_l^2\times\frac{a_t^2\rho^2}{a_l^2z^2}}{\left(1+\frac{a_t^2\rho^2}{a_l^2z^2}\right)}+\frac{ik_0\left(z+\frac{\rho^2}{2z}-t\right)}{1+\frac{a_t^2\rho^2}{a_l^2z^2}}-\frac{i\pi}{2}. \tag{4.23}$$

Given the complicated appearance of the far-field solution, it is appropriate to find an expression specifically only for the region where the solution has a non-vanishing magnitude. Therefore we require the absolute values of the two non-positive real terms in the exponent to be comparable to or less than $\mathcal{O}(1)$. In particular, the second real term in Eq. (4.23) imposes the condition

$$\left(\frac{a_t\rho}{a_lz}\right)^2\lesssim\mathcal{O}\left((k_0a_l)^{-2}\right)\ll1, \tag{4.24}$$

which is equivalent to $\rho/z\lesssim\mathcal{O}\left((k_0a_t)^{-1}\right)\ll1$. Subsequently, the first term suggests that

$$z+\frac{\rho^2}{2z}-t\lesssim\mathcal{O}(a_l). \tag{4.25}$$

Applying Eq. (4.24) to Eq. (4.23), we find

$$\begin{aligned}\Psi_{\text{far}}(\vec{r},t)\approx&\left[(2\pi)^3\boldsymbol{\sigma_t}(z)^4a_l^2\right]^{-\frac{1}{4}}\\&\times\exp\left[-\frac{\left(z+\frac{\rho^2}{2z}-t\right)^2}{4a_l^2}-\frac{\rho^2}{4\boldsymbol{\sigma_t}(z)^2}+ik_0\left(z+\frac{\rho^2}{2z}-t\right)-i\frac{\pi}{2}\right],\end{aligned} \tag{4.26}$$

where the far-field approximation of $\boldsymbol{\sigma_t}(z)$ shown in Eq. (4.19) is assumed. At this point, we can compare the solution Eq. (4.6) derived with the Fourier transform method with Eq. (4.26). These two solutions are in fact identical to each other on the z-axis, except that the time-dependence in Eq. (4.7)-(4.8) have been replaced by the z-dependence in Eq. (4.13)-(4.14). Of course, away from the z-axis, the two solutions start to show difference in that Eq. (4.26) implies a spherical curvature to be discussed below whereas Eq. (4.6) is a flat WP.

The solution in Eq. (4.26) can be easily understood if expressed in terms of spherical coordinates; the term $z+\rho^2/2z$ in Eq. (4.26) can be approximated as

the radial distance $r = \sqrt{z^2 + \rho^2}$ since $\rho/z \ll 1$ whereas other standalone ρ and z variables can be substituted, respectively, by $r\sin\theta$ and $r\cos\theta$ by definition. Eq. (4.26) can then be factorized as

$$\Psi_{\text{far}}(\vec{r}, t) \approx \frac{1}{r}\sqrt{\Theta(\hat{r})}\Psi_{1D}(r, t), \tag{4.27}$$

where

$$\Psi_{1D}(r, t) \equiv \frac{1}{(2\pi a_l^2)^{\frac{1}{4}}} \exp\left[-\frac{(r-t)^2}{4a_l^2} + ik_0(r-t) - i\frac{\pi}{2}\right] \text{ for } r > 0 \tag{4.28}$$

is an effective 1D Gaussian wave packet and

$$\Theta(\theta) \equiv \begin{cases} \frac{(2k_0a_t)^2}{2\pi\cos^2\theta} \exp\left[-\frac{\tan^2\theta}{2\cdot(2k_0a_t)^{-2}}\right] & \text{, if } 0 \le \theta < \frac{\pi}{2}, \\ 0 & \text{, if } \frac{\pi}{2} \le \theta \le \pi, \end{cases} \tag{4.29}$$

is an angular probability distribution that is peaked in the forward direction and normalized over the entire 4π solid angle. Eq. (4.27) justifies the prevalent 1D simplification of neutrino propagation in that the wave mechanics can be dealt with solely by the effective 1D wave function whereas the factor $r^{-1}\sqrt{\Theta}$ properly accounts for the normalization of probability flux when squared. In practical situations, the source is incoherent and emits neutrinos into a solid angle that is much greater than the effective solid angle spanned by a single WP. Upon averaging over the source solid angle, Eq (4.29) plays no role in the observed number flux of neutrinos.

4.3 Viewpoint from Wave-particle Duality

The far-field solution shown in Eq. (4.26) can also be understood as a manifestation of wave-particle duality. In the absence of interference, a quantum particle described by its wave function may as well be regarded as a classical point particle with a probability distribution for its momentum; that probability distribution is in fact equal to the modulus square of the Fourier transform of the wave function.

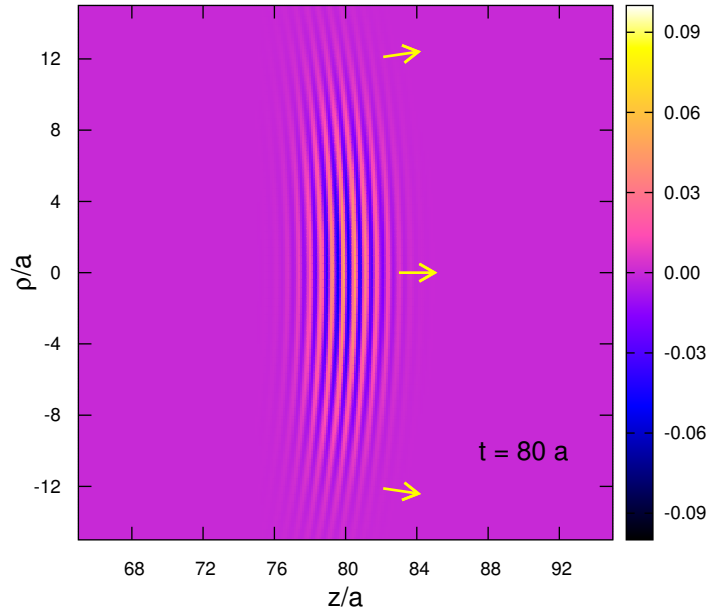

Figure 4.1: The real part of far-field solution at $t = 80a$. For visualization purpose, the plot is made by assuming $a_t = a_l \equiv a$ and $k_0 a = 10$. Yellow arrows point radially away from the origin and they are perpendicular to the spherical wavefront.

This way, the constant longitudinal position width of the far-field WP solution can be understood by viewing the particle as a bullet-like object; the initial longitudinal position uncertainty is simply retained by the momentum-independent propagating speed of the massless particle, i.e. the speed of light. On the other hand, the WP's transverse size can easily grow to a macroscopic size thanks to the nonzero transverse momentum component allowed by the probability distribution. From the perspective of wave mechanics, an observer far away from the origin of the WP only "sees" a wave train. Because the phase term in the far-field solution is spherical, the observed momentum of the wave train points in the same direction as defined in a ballistic sense, i.e. parallel to the position vector pointing from the origin to the observer, as illustrated in Fig. 4.1.

By invoking the wave-particle duality discussed above, the angular probability distribution of the far-field solution, i.e. Eq. (4.29), should be equivalent to that derived from the momentum distribution of the initial WP, without actually finding its evolution at $t > 0$. Viewing the particle as classical, the probability of finding the particle at sufficiently far away (so that the initial position uncertainty can be neglected) along a certain direction is equal to the probability that the particle initially has a momentum pointing in that direction. We begin the verification of the above statement by referring to the Fourier transform of the initial WP shown in Eq. (4.3). The normalization condition of Eq. (4.3) can be expressed with spherical coordinates

$$1 = \int \frac{\mathrm{d}^3\vec{k}}{(2\pi)^3}\left|\tilde{\Psi}(\vec{k})\right|^2 = \int\limits_{S^2} \mathrm{d}\Omega \int\limits_0^\infty \frac{k^2\mathrm{d}k}{(2\pi)^3}\left|\tilde{\Psi}(\vec{k})\right|^2, \tag{4.30}$$

from which we can infer an angular probability distribution

$$\begin{aligned} S(\theta) &\equiv \int\limits_0^\infty \frac{k^2\mathrm{d}k}{(2\pi)^3}\left|\tilde{\Psi}(\vec{k})\right|^2 \\ &= \int\limits_0^\infty \frac{k^2\mathrm{d}k}{(2\pi)^3} \times (8\pi)^{\frac{3}{2}} a_t^2 a_l \exp\left[-a_t^2 k^2 \sin^2\theta - a_l^2\left(k\cos\theta - k_0\right)^2\right] \end{aligned} \tag{4.31}$$

that satisfies $1 = \int_{S^2} \mathrm{d}\Omega\, S(\theta)$. The integration is somewhat tedious to carry out but it can be shown to have a closed-form expression

$$S(\theta) = \frac{a_t^2 a_l \exp\left(-\zeta\right)}{(2\pi)^{3/2}\delta^{5/2}}\left\{2\epsilon\sqrt{\delta} + \sqrt{\pi}(2\delta + \epsilon^2)\exp\left(\frac{\epsilon^2}{4\delta}\right)\left[1 + \mathrm{erf}\left(\frac{\epsilon}{2\sqrt{\delta}}\right)\right]\right\}, \tag{4.32}$$

where the three positive quantities as well as the error function are defined as

$$\begin{aligned} \delta &\equiv 2(a_t^2\sin^2\theta + a_l^2\cos^2\theta) \\ \epsilon &\equiv 4k_0 a_l^2\cos\theta \\ \zeta &\equiv 2k_0^2 a_l^2 \\ \mathrm{erf}(x) &\equiv \frac{2}{\sqrt{\pi}}\int_0^x \mathrm{d}t\, \exp\bigl(-t^2\bigr). \end{aligned} \tag{4.33}$$

Despite the very different appearances of Eq. (4.29) and Eq. (4.32), the two angular probability distributions are in fact consistent with each other under the assumption of sharp momentum distribution. By making small angle approximation, we can immediately see that Eq. (4.29) reduces to a Gaussian distribution with an angular width $(2k_0a_t)^{-1}$. To show that $S(\theta)$ also reduces to the same Gaussian distribution, we note that the first term in the curly brackets of Eq. (4.32) is suppressed by the factor $\exp(-\zeta)$ whereas the second term is non-vanishing only if the factor,

$$\exp\left(\frac{\epsilon^2}{4\delta}-\zeta\right)=\exp\left(-\frac{2k_0^2a_l^2a_t^2\sin^2\theta}{a_t^2\sin^2\theta+a_l^2\cos^2\theta}\right)\leq 1, \tag{4.34}$$

is not diminishingly small. By requiring $|\epsilon^2/4\delta-\zeta|\lesssim\mathcal{O}(1)$, we can deduce that

$$a_t^2\sin^2\theta\lesssim\frac{a_l^2\cos^2\theta}{2k_0^2a_l^2-1}\ll a_l^2\cos^2\theta. \tag{4.35}$$

This condition implies $\epsilon\gg\sqrt{\delta}$ which can be used to greatly simplify the expression. It is then straightforward to show that

$$S(\theta)\approx\Theta(\theta)\approx\frac{(2k_0a_t)^2}{2\pi}\exp\left[-\frac{\theta^2}{2\cdot(2k_0a_t)^{-2}}\right], \tag{4.36}$$

which has no dependence on a_l. This is consistent with the simple estimate on the WP's angular size using the ratio of transverse momentum uncertainty to the mean momentum of the initial WP.

In this chapter, we have derived the 3D Gaussian WP solution and clarified why common 1D treatment suffices for describing the propagation of neutrinos when the interference among them is not of concern. We also addressed the wave-particle duality implied by the solution and this concept will be frequently referred to in the next chapter where the detection of WPs is discussed.

Chapter 5

Quantum Mechanics of Wave Packet Detection

In a scenario where the source is intensive enough such that the 3D wave functions of the emitted neutrinos overlap, a formal many-particle wave function might be needed. An immediate consequence implied by such description is the well-known Pauli exclusion principle which states that two identical fermions cannot be found in the same state. One is then tempted to wonder if this would affect the detection of neutrinos from an intensive source. To answer the question of what interference effect might be observed, we divide the following discussion into two cases. The first case concerns the scenario where only one neutrino is detected at a time and the second case concerns "simultaneous" detection of more than one overlapping neutrinos. For the second case, we will first review the description of WP detection in a quantum-mechanical framework and then discuss the conditions for the HBT effect discussed in Chap. 1. This effect is closely related to the exchange symmetry of fundamental particles as will be discussed in the later part of this chapter.

5.1 When Only One Neutrino Is Detected

To grasp the key idea without invoking unnecessary mathematical complexity, we consider only two 1-particle wave functions, $\Psi^{P_1}(\vec{r},t)$ and $\Psi^{P_2}(\vec{r},t)$, originating from two production processes labeled as P_1 and P_2. Most likely, P_1 and P_2 are separated by a macroscopic distance in the source. Without loss of generality, the normalized two-particle wave function is expressed as

$$\Phi(\vec{r}_1,\vec{r}_2,t)=\frac{\Psi^{P_1}(\vec{r}_1,t)\Psi^{P_2}(\vec{r}_2,t)-\Psi^{P_2}(\vec{r}_1,t)\Psi^{P_1}(\vec{r}_2,t)}{\sqrt{2-2|\langle\Psi^{P_1}|\Psi^{P_2}\rangle|^2}}. \tag{5.1}$$

The probability density of finding one neutrino at $\vec{r}$ regardless of the other is then

$$\begin{aligned}\rho(\vec{r}) &= \int \mathrm{d}^3\vec{r}_2\left|\Phi(\vec{r},\vec{r}_2)^2\right| + \int \mathrm{d}^3\vec{r}_1\left|\Phi(\vec{r}_1,\vec{r})\right|^2 \\ &= \frac{\left|\Psi^{P_1}(\vec{r})\right|^2+\left|\Psi^{P_2}(\vec{r})\right|^2-2\mathrm{Re}\left[\Psi^{P_1}(\vec{r})\Psi^{*P_2}(\vec{r})\langle\Psi^{P_1}|\Psi^{P_2}\rangle\right]}{1-|\langle\Psi^{P_1}|\Psi^{P_2}\rangle|^2},\end{aligned} \tag{5.2}$$

where the time dependence is not explicitly shown. The above equation shows that interference term is independent of the initial phases of the 1-particle states and is proportional to the magnitude of $\langle\Psi_a|\Psi_b\rangle$. Although the WP states may overlap in both position and momentum spaces, their inner product is in fact zero. The 1-particle WP states are governed by the same time evolution operator and the unitarity of the operator suggests that the inner product is time-independent:

$$\langle\Psi^{P_1}(t)|\Psi^{P_2}(t)\rangle=\langle\Psi^{P_1}(0)|\mathrm{e}^{i\hat{H}t}\mathrm{e}^{-i\hat{H}t}|\Psi^{P_2}(0)\rangle=\langle\Psi^{P_1}(0)|\Psi^{P_2}(0)\rangle, \tag{5.3}$$

where $\hat{H}$ is a relevant Hamiltonian operator. By tracing back to the time when the WPs emerge from spatially separated production regions in the source, it is clear that the inner product should be zero. Therefore, Eq. (5.1) reduces to a Slater determinant and Eq.(5.2) reduces to a simple sum of 1-particle probability densities. With a bit more algebraic effort, the above argument can be applied to an arbitrary number of overlapping neutrinos.

5.2 Quantum Mechanics of WP Detection

It is beneficial to review the description of WP detection in a more formalistic way before discussing the HBT effect of neutrinos. The detection process can be described as a projection of the neutrino WP onto a detected WP state [19]. Such treatment provides a simply way to derive the oscillation probability for neutrino WPs, when the neutrino masses are considered, in a quantum-mechanical framework. We remark that the detected state to be discussed below is merely an ad hoc description that represents the approximate conservation of momentum associated with the detection process. Neither does such detected WP state correspond to an actual particle nor does it evolve in time (or propagate in space). An implicit assumption implied by this "static" WP state is that the detection process is uninterrupted, i.e. it lasts sufficiently long for the incoming neutrino wave train to pass through the detection region.

To begin, we assume that the detected state is a Gaussian WP characterized by a mean momentum $\vec{k}_0^D$, a transverse position width a_t^D, and a longitudinal position width a_l^D, where the label "D" is used to distinguish from the parameters labeled with "P" for the neutrino WP from the production process. The detection process may take place at an "off-axis" position from the neutrino's classical path. As discussed in Sec. 4.3, the detection process observes a wave train with a momentum direction defined by the production and detection locations. For the following discussion, we shall define the line joining the two locations as the z-axis[1] with $z = 0$ and $z = L$ defined to be the centers of the production location and detection location, respectively. We remark that the mean momentum of the detected WP does not necessarily have to align with this z-axis as long as the incoming wave train's momentum component transverse to $\vec{k}_0^D$ does not exceed the transverse momentum uncertainty of the detected WP. Nevertheless, the following analysis assumes that $\vec{k}_0^D = k_0^D \hat{z}$ for simplicity. Similar to Eq. (4.2), the detected WP state

[1] This is not to be confused with the coordinate definition in Chap. 4 where the z-axis is defined to be the neutrino's classical path.

is described as

$$\Psi^D(\vec{r}) = \left[(2\pi)^3 a_t^{D\,4} a_l^{D\,2}\right]^{-\frac{1}{4}} \exp\left[-\frac{\rho^2}{4a_t^{D\,2}} - \frac{(z-L)^2}{4a_l^{D\,2}} + ik_0^D(z-L)\right]. \tag{5.4}$$

On the other hand, the incoming neutrino wave train can be effectively described by

$$\Psi^P(\vec{r},t) = \frac{\sqrt{\Theta_{P\to D}}}{L}\Psi_{1D}(z,t) \tag{5.5}$$

according to Eq. (4.27) and Eq. (4.28) in the neighborhood of the detection location where the values of $\Theta(\hat{r})$ and $1/r$ are essentially constant.

The transition amplitude can be calculated via straightforward integration of Eq. (5.4) and Eq. (5.5) over position space and it is found to be

$$\langle\Psi^D|\Psi^P(t)\rangle \propto \frac{\sqrt{\Theta_{P\to D}}}{L}\exp\left[-\frac{(t-L)^2}{4\sigma_{z,eff}^2} - \frac{(k_0^P - k_0^D)^2}{4\sigma_{k,eff}^2} - ik_{eff}^{PD}\times(t-L)\right], \tag{5.6}$$

where the effective position and momentum widths are defined as

$$\begin{aligned}\sigma_{z,eff}^2 &\equiv a_l^{P\,2} + a_l^{D\,2}\\ \sigma_{k,eff}^2 &\equiv \frac{1}{4a_l^{P\,2}} + \frac{1}{4a_l^{D\,2}}\end{aligned} \tag{5.7}$$

and the effective momentum is defined as

$$k_{eff}^{PD} \equiv \xi k_0^P + (1-\xi)k_0^D \tag{5.8}$$

with a weighting parameter $(0 < \xi < 1)$

$$\xi \equiv \frac{a_l^{P\,2}}{a_l^{P\,2} + a_l^{D\,2}}. \tag{5.9}$$

A few comments about the derived transition amplitude are made in the following. Eq. (5.6) is up to an arbitrary and constant complex phase as well as a factor that depends on the position widths of the two WPs. The transition amplitude is non-vanishing only if $|t-L| \lesssim \sigma_{z,eff}$ and $|k_0^P - k_0^D| \lesssim \sigma_{k,eff}$, which respectively reflect causality and conservation of momentum within given uncertainties. The

effective momentum is, roughly speaking, determined by whichever WP state that has a more precisely defined momentum (thus energy). For instance, if $a_l^D \gg a_l^P$, the momentum uncertainty of $|\Psi^D\rangle$ is much smaller than $|\Psi^P\rangle$ according to Heisenberg's uncertainty principle and, in this case, $k_{eff}^{PD} \approx k_0^D$. We also note that the effective widths shown in Eq. (5.7) satisfy an uncertainty relation

$$\sigma_{z,eff} \times \sigma_{k,eff} = \frac{a_l^{P\,2} + a_l^{D\,2}}{2a_l^P a_l^D} \geq 1, \tag{5.10}$$

where the inequality is inferred from the inequality of arithmetic and geometric means. The product reaches its minimum at $a_l^D/a_l^P = 1$ and approaches to infinity at $a_l^D/a_l^P \to 0$ or $a_l^D/a_l^P \to \infty$. In comparison to a Gaussian WP, which mathematically has the minimal uncertainty product, the transition amplitude has a slightly larger lower bound for the uncertainty product.

Assuming that the detection time is not measured, the detection probability can be found by integrating the modulus square of the transition amplitude over time, i.e.

$$Pr(P \to D) \propto \int \mathrm{d}t \left|\langle \Psi^D | \Psi^P(t) \rangle\right|^2 \propto \frac{\Theta_{P\to D}}{L^2} \exp\left(-\frac{(k_0^P - k_0^D)^2}{2\sigma_{k,eff}^2}\right). \tag{5.11}$$

Overall, this result meets the expectation that the detection probability should decrease with L^{-2} and be proportional to the angular probability $\Theta_{P\to D}$. We comment that in this quantum-mechanical framework a correct normalization for the probability cannot be obtained self-consistently which is not the main goal to achieve here. Nevertheless, this framework provides a simple expression for the detection probability that allows a succinct presentation of the interference effect later on. Finally, the complex phase, $\exp\left[-ik_{eff}^{PD}(t-L)\right]$, in Eq. (5.6) does not appear in the one-particle detection probability shown above for an obvious reason, but this varying phase actually plays a crucial role in the HBT effect as we shall discuss in the following.

5.3 When Two Neutrinos Are Detected

We now consider pair-detection by two uncorrelated processes D_1 and D_2 of two neutrinos produced from two uncorrelated processes P_1 and P_2 as schematically depicted in Fig. 5.1. Suppose the source and the detector are well separated such that the directional difference of the P_1 and P_2 locations cannot be resolved by either of the detection processes. Therefore, when the momenta of $|\Psi^{P_1}\rangle$ and $|\Psi^{P_2}\rangle$ as seen at the detector are very similar to those of $|\Psi^{D_1}\rangle$ and $|\Psi^{D_2}\rangle$, the ambiguity of pairing a production process with a detection process may arise. Similar to Eq. (5.11), the pair-detection probability is obtained by integrating the squared amplitude over the two detection times t_1 and t_2

$$\begin{aligned} &Pr(P_1P_2 \to D_1D_2) \\ &\quad \propto \frac{1}{2}\int \mathrm{d}t_1\mathrm{d}t_2 \left|\langle\Psi^{D_1}|\Psi^{P_1}(t_1)\rangle\langle\Psi^{D_2}|\Psi^{P_2}(t_2)\rangle - \langle\Psi^{D_1}|\Psi^{P_2}(t_1)\rangle\langle\Psi^{D_2}|\Psi^{P_1}(t_2)\rangle\right|^2, \end{aligned} \tag{5.12}$$

where the amplitude entails two possible configurations of production-detection pairing and the negative sign reflects the exchange symmetry of fermions. Expanding the integrand of Eq. (5.12) and referring to the 1-particle detection probability shown in Eq. (5.11), the pair-detection probability can be expressed as

$$\begin{aligned} &Pr(P_1P_2 \to D_1D_2) \\ &\quad \propto \frac{1}{2}\left[Pr(P_1 \to D_1) \times Pr(P_2 \to D_2) + Pr(P_1 \to D_2) \times Pr(P_2 \to D_1)\right] \\ &\quad - \int \mathrm{d}t_1\mathrm{d}t_2\, \mathfrak{Re}\left[\langle\Psi^{D_1}|\Psi^{P_1}(t_1)\rangle\langle\Psi^{D_2}|\Psi^{P_2}(t_2)\rangle\langle\Psi^{P_2}(t_1)|\Psi^{D_1}\rangle\langle\Psi^{P_1}(t_2)|\Psi^{D_2}\rangle\right], \end{aligned} \tag{5.13}$$

where the second line is an incoherent sum of products of 1-particle probabilities and the third line is the interference term to be investigated in details. The quartic amplitude in the interference term is invariant under arbitrary re-phasing of the four WP states. Furthermore, if the arrival times of the two wave trains, $|\Psi^{P_1}\rangle$ and $|\Psi^{P_2}\rangle$, at either of the detection locations are not sufficiently close, the quartic

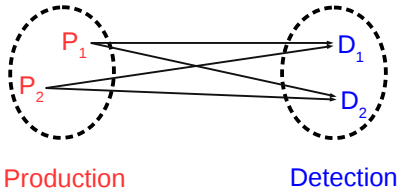

Figure 5.1: Diagrammatic illustration of pairing two production processes with two detection processes. $\overline{P_1P_2}$ and $\overline{D_1D_2}$ do not necessarily lie in the same plane. The size of the source and the detector, as defined by the dashed borders, are exaggerated. The four lines are virtually parallel to each other under the geometrical condition for the HBT effect to be derived in Sec. 5.4.

amplitude vanishes since at least one of the first and the third (similarly, second and fourth) constituent amplitudes will be zero at any given time. In addition to the proximity of $|\Psi^{P_1}\rangle$ and $|\Psi^{P_2}\rangle$, a few more conditions are in fact required for an experimentally observable interference effect. These conditions inevitably require some laborious mathematical derivation to uncover.

Without loss of generality, we define the production time of $|\Psi^{P_1}\rangle$ to be $t = 0$ and that of $|\Psi^{P_2}\rangle$ to be $t = t_0$, where t_0 can be either positive or negative. We consider only the same particle interaction channel for P_1 and P_2 (likewise, the same channel for D_1 and D_2) such that both WP states can be characterized by the same width parameters. As in the derivation of 1-particle detection probability, both the mean momenta of $|\Psi^{D_1}\rangle$ and $|\Psi^{D_2}\rangle$ are assumed to align with the momenta of the wave trains from $|\Psi^{P_1}\rangle$ and $|\Psi^{P_2}\rangle$ to simplify the calculation; this assumption is legitimate since, with sufficient source-detector distance, $\overrightarrow{P_1D_j}$ are approximately parallel to $\overrightarrow{P_2D_j}$ for $j = 1$ or 2. The ingredients needed for

Eq. (5.13) can be obtained by making a quick reference to Eq. (5.6):

$$\begin{aligned}
&\langle \Psi^{D_j} | \Psi^{P_1}(t) \rangle \\
&\propto \frac{\sqrt{\Theta_{P_1 \to D_j}}}{L_{1j}} \exp\left[-\frac{(t - L_{1j})^2}{4\sigma_{z,eff}^2} - \frac{(k_0^{P_1} - k_0^{D_j})^2}{4\sigma_{k,eff}^2} - i k_{eff}^{P_1 D_j} (t - L_{1j}) \right] \\
&\langle \Psi^{D_j} | \Psi^{P_2}(t) \rangle \\
&\propto \frac{\sqrt{\Theta_{P_2 \to D_j}}}{L_{2j}} \exp\left[-\frac{(t - t_0 - L_{2j})^2}{4\sigma_{z,eff}^2} - \frac{(k_0^{P_2} - k_0^{D_j})^2}{4\sigma_{k,eff}^2} - i k_{eff}^{P_2 D_j} (t - t_0 - L_{2j}) \right],
\end{aligned} \tag{5.14}$$

where $L_{ij} \equiv \overline{P_i D_j}$ and the definitions in Eq. (5.7)-(5.8) apply. In the factor multiplying the exponential function of each amplitude, an approximation $\Theta_{P_j \to D_1} \approx \Theta_{P_j \to D_2} \equiv \Theta_{P_j}$, for $j = 1$ or 2, can be made since the angular size of the detector as seen at the source can be safely neglected. In addition, the distance variable in that prefactor can also be approximated by an average source-detector distance L_0. However, extra care shall be taken with the distance variable in the exponent as it is relevant to the quantum phase that gives rise to the interference effect; for instance, a 10 MeV SN neutrino has a de Broglie wavelength of order 10 fm which dictates a very small margin of error in the length approximation to be dealt with later. With Eq. (5.14), the quartic amplitude is found to be

$$\begin{aligned}
&\langle \Psi^{D_1} | \Psi^{P_1}(t_1) \rangle \langle \Psi^{D_2} | \Psi^{P_2}(t_2) \rangle \langle \Psi^{P_2}(t_1) | \Psi^{D_1} \rangle \langle \Psi^{P_1}(t_2) | \Psi^{D_2} \rangle \\
&\propto \frac{\Theta_{P_1} \Theta_{P_2}}{L_0^4} \\
&\times \exp\left\{ \frac{-1}{4\sigma_{z,eff}^2} \left[(t_1 - L_{11})^2 + (t_2 - t_0 - L_{22})^2 + (t_1 - t_0 - L_{21})^2 + (t_2 - L_{12})^2 \right] \right\} \\
&\times \exp\left\{ \frac{-1}{4\sigma_{k,eff}^2} \left[(k_0^{P_1} - k_0^{D_1})^2 + (k_0^{P_2} - k_0^{D_2})^2 + (k_0^{P_2} - k_0^{D_1})^2 + (k_0^{P_1} - k_0^{D_2})^2 \right] \right\} \\
&\times \exp\left\{ i\xi \left(k_0^{P_2} - k_0^{P_1} \right) (t_1 - t_2) \right\} \\
&\times \exp\left\{ i \left[k_{eff}^{P_1 D_1} L_{11} + k_{eff}^{P_2 D_2} (t_0 + L_{22}) - k_{eff}^{P_2 D_1} (t_0 + L_{21}) - k_{eff}^{P_1 D_2} L_{12} \right] \right\}.
\end{aligned} \tag{5.15}$$

At first glance, the imaginary part of the exponent gives rise to temporal (the second last line) and spatial (the last line) oscillations which on average do not contribute to the pair-detection probability. With the same prefactor $\Theta_{P_1}\Theta_{P_2}/L_0^4$ as the incoherent part of the pair-detection probability, the interference term can, however, "reshuffle" the overall temporal distribution (hence the term "anti-bunching" effect for fermions) of the two detections if certain conditions are met.

A few more steps to rewrite the quartic amplitude are necessary before the physics picture becomes clear. We first define

$$\begin{aligned} \bar{k}_0^P &\equiv \frac{1}{2}(k_0^{P_1} + k_0^{P_2}),\ \Delta k_0^P \equiv k_0^{P_1} - k_0^{P_2}, \\ \bar{k}_0^D &\equiv \frac{1}{2}(k_0^{D_1} + k_0^{D_2}),\ \text{and}\ \Delta k_0^D \equiv k_0^{D_1} - k_0^{D_2}, \end{aligned} \tag{5.16}$$

as well as recall the definition of the effective momentum in Eq. (5.8)-(5.9). These identities allow one to rewrite $k_{eff}^{P_1D_1} = \xi(\bar{k}_0^P + \frac{1}{2}\Delta k_0^P) + (1-\xi)(\bar{k}_0^D + \frac{1}{2}\Delta k_0^D)$ and the other three effective momenta with similar expressions. Then it follows that, in the last line of Eq. (5.15),

$$\begin{aligned} &k_{eff}^{P_1D_1}L_{11} + k_{eff}^{P_2D_2}(t_0 + L_{22}) - k_{eff}^{P_2D_1}(t_0 + L_{21}) - k_{eff}^{P_1D_2}L_{12} \\ &= \left[\xi\bar{k}_0^P + (1-\xi)\bar{k}_0^D\right](L_{11} + L_{22} - L_{21} - L_{12}) \\ &+ \frac{1}{2}\xi\Delta k_0^P\,(L_{11} - L_{22} + L_{21} - L_{12}) \\ &+ \frac{1}{2}(1-\xi)\Delta k_0^D\,(L_{11} - L_{22} - L_{21} + L_{12} - 2t_0)\,. \end{aligned} \tag{5.17}$$

Furthermore, by defining $\vec{L}_0 \equiv \frac{1}{2}(\overrightarrow{P_1D_1} + \overrightarrow{P_2D_2})$, $\vec{\Delta}_P \equiv \overrightarrow{P_1P_2}$, and $\vec{\Delta}_D \equiv \overrightarrow{D_1D_2}$, it is shown in Appendix D that three different combinations of the four distance variables can be approximated as

$$\begin{aligned} L_{11} + L_{22} - L_{21} - L_{12} &\approx -\frac{\Delta_{P,\perp}\Delta_{D,\perp}\cos\phi}{L_0} \\ L_{11} - L_{22} + L_{21} - L_{12} &\approx -2\Delta_{D,\parallel} \\ L_{11} - L_{22} - L_{21} + L_{12} - 2t_0 &\approx 2\left(\Delta_{P,\parallel} - t_0\right), \end{aligned} \tag{5.18}$$

where the "$\perp$" and "$\parallel$" components are defined with respect to $\hat{L}_0$ and ϕ is the angle between $\vec{\Delta}_{P,\perp}$ and $\vec{\Delta}_{D,\perp}$. With Eq. (5.17)-(5.18), the quartic amplitude can

now be expressed as

$$
\begin{aligned}
&\langle\Psi^{D_1}|\Psi^{P_1}(t_1)\rangle\langle\Psi^{D_2}|\Psi^{P_2}(t_2)\rangle\langle\Psi^{P_2}(t_1)|\Psi^{D_1}\rangle\langle\Psi^{P_1}(t_2)|\Psi^{D_2}\rangle \\
&\propto \frac{\Theta_{P_1}\Theta_{P_2}}{L_0^4} \\
&\times \exp\left\{\frac{-1}{4\sigma_{z,eff}^2}\left[(t_1-L_{11})^2+(t_2-t_0-L_{22})^2+(t_1-t_0-L_{21})^2+(t_2-L_{12})^2\right]\right\} \\
&\times \exp\left\{\frac{-1}{4\sigma_{k,eff}^2}\left[(k_0^{P_1}-k_0^{D_1})^2+(k_0^{P_2}-k_0^{D_2})^2+(k_0^{P_2}-k_0^{D_1})^2+(k_0^{P_1}-k_0^{D_2})^2\right]\right\} \\
&\times \exp\left\{i\left[\xi\Delta k_0^P\left(t_2-t_1-\Delta_{D,\|}\right)+(1-\xi)\Delta k_0^D\left(\Delta_{P,\|}-t_0\right)\right]\right\} \\
&\times \exp\left\{-i\left[\xi\bar{k}_0^P+(1-\xi)\bar{k}_0^D\right]\times\frac{\Delta_{P,\perp}\Delta_{D,\perp}\cos\phi}{L_0}\right\}.
\end{aligned}
\tag{5.19}
$$

5.4 Conditions for the HBT Effect

We are now ready to interpret the interference term in the current form shown in Eq. (5.19). To begin, we give physical interpretation of the two quantities $t_2-t_1-\Delta_{D,\|}$ and $\Delta_{P,\|}-t_0$ appearing in the complex phase. As t_1 and t_2 are the detection times, the quantity $t_2-t_1-\Delta_{D,\|}$ corresponds to the relative distance parallel to $\hat{L}_0$ between the two "point-like" neutrinos as determined by the two detection processes. This can be understood from an analogy of two marathon runners who run at the same known speed. Suppose the passage of each runner at a different checkpoint is timed and the distance between the two checkpoints is known. Then the constant distance between the two runners is determinable given the two time measurements and the distance between the two checkpoints. Similarly, the quantity $\Delta_{P,\|}-t_0$ is simply the parallel distance between the two neutrinos as they emerge from the production processes. Although the two neutrinos are supposed to maintain constant distance between them, the quantity $t_2-t_1-\Delta_{D,\|}$ need not coincide with the quantity $\Delta_{P,\|}-t_0$ simply because of the intrinsic position uncertainties of the production and detection processes. In the following, we shall

discuss the interference conditions in relation to these two quantities.

Two sets of conditions are required for a non-vanishing magnitude of the interference term: The first set of conditions is

$$\left.\begin{aligned} |t_1 - L_{11}| \\ |t_2 - t_0 - L_{22}| \\ |t_1 - t_0 - L_{21}| \\ |t_2 - L_{12}| \end{aligned}\right\} \lesssim \mathcal{O}(\sigma_{z,eff}), \tag{5.20}$$

which, by combining two of the four inequalities using the identity$|A - B| \leq |A| + |B|$, implies (for $j = 1$ or 2)

$$|t_2 - t_1 - (L_{j2} - L_{j1})| \approx \left|t_2 - t_1 - \Delta_{D,\|}\right| \lesssim \mathcal{O}(\sigma_{z,eff}) \text{ and} \tag{5.21a}$$

$$|L_{1j} - L_{2j} - t_0| \approx \left|\Delta_{P,\|} - t_0\right| \lesssim \mathcal{O}(\sigma_{z,eff}). \tag{5.21b}$$

The second set of conditions is

$$\left.\begin{aligned} \left|k_0^{P_1} - k_0^{D_1}\right| \\ \left|k_0^{P_2} - k_0^{D_2}\right| \\ \left|k_0^{P_2} - k_0^{D_1}\right| \\ \left|k_0^{P_1} - k_0^{D_2}\right| \end{aligned}\right\} \lesssim \mathcal{O}(\sigma_{k,eff}), \tag{5.22}$$

which, again by combining two of the above four inequalities, implies

$$\left|k_0^{P_1} - k_0^{P_2}\right| = \left|\Delta k_0^P\right| \lesssim \mathcal{O}(\sigma_{k,eff}) \text{ and} \tag{5.23a}$$

$$\left|k_0^{D_1} - k_0^{D_2}\right| = \left|\Delta k_0^D\right| \lesssim \mathcal{O}(\sigma_{k,eff}). \tag{5.23b}$$

Strictly speaking, if these two sets of conditions are satisfied, the interference among the four amplitudes occurs; however, these conditions alone do not guarantee an observable interference effect.

In addition to the non-vanishing magnitude, the interference term must not undergo rapid oscillations upon summing over all pairs of production and detection processes since otherwise the interference effect will be smeared. This means that the imaginary part of the exponent of Eq. (5.19) must be kept small compared to π. Therefore, we require

$$\left|\xi\Delta k_0^P\left(t_2 - t_1 - \Delta_{D,\parallel}\right)\right| \lesssim \mathcal{O}(1) \text{ and} \tag{5.24a}$$

$$\left|(1-\xi)\Delta k_0^D\left(\Delta_{P,\parallel} - t_0\right)\right| \lesssim \mathcal{O}(1) \tag{5.24b}$$

as well as

$$\left[\xi\bar{k}_0^P + (1-\xi)\bar{k}_0^D\right]\frac{\Delta_{P,\perp}\Delta_{D,\perp}}{L_0} \lesssim \mathcal{O}(1). \tag{5.25}$$

Recalling Eq. (5.9)-(5.10), we can observe that Eq. (5.21) and Eq. (5.23) automatically guarantee Eq. (5.24) if $a_l^P \sim a_l^D$. However, Eq. (5.24) imposes additional constraints when $a_l^P \gg a_l^D$ or $a_l^P \ll a_l^D$. To summarize at this point, the HBT effect requires all the conditions shown in Eq. (5.21), (5.23), (5.24), and (5.25) to be met.

The quantity $t_2 - t_1 - \Delta_{D,\parallel}$ discussed earlier is subject to the inequalities Eq. (5.21a) and Eq. (5.24a). The later can be expressed as

$$\left|t_2 - t_1 - \Delta_{D,\parallel}\right| \lesssim \xi^{-1}\left|\Delta k_0^P\right|^{-1} \sim \xi^{-1}\sigma_{k,eff}^{-1} \sim \frac{a_l^D}{a_l^P} \times \sigma_{z,eff}, \tag{5.26}$$

where $\left|\Delta k_0^P\right| \sim \sigma_{k,eff}$ is assumed. Combining Eq. (5.26) and Eq. (5.21a) and recalling the asymptotic values of $\sigma_{z,eff}$, we obtain

$$\left|t_2 - t_1 - \Delta_{D,\parallel}\right| \lesssim \min\left(1, \frac{a_l^D}{a_l^P}\right) \times \sigma_{z,eff} \sim a_l^D, \tag{5.27}$$

regardless of whether $a_l^D \gg a_l^P$ or $a_l^D \ll a_l^P$. Note that in principle it is possible that $\left|\Delta k_0^P\right| \ll \sigma_{k,eff}$, in which case the combined upper bound shown above might be relaxed up to $\sigma_{z,eff}$; however, this scenario is much less probable as the relevant neutrino flux is proportional to the energy width directly translated from $\left|\Delta k_0^P\right|$.

The interpretation of Eq. (5.27) is quite simple: the condition states that the two detection processes, with the finite spatial resolution a_l^D, cannot tell the neutrinos apart along the parallel direction. Similarly, Eq. (5.21b) and Eq. (5.24b) together set the upper bound of $\left|\Delta_{P,\parallel} - t_0\right|$. With the assumption $\left|\Delta k_0^D\right| \sim \sigma_{k,eff}$, we obtain

$$\left|\Delta_{P,\parallel} - t_0\right| \lesssim \min\left(1, \frac{a_l^P}{a_l^D}\right) \times \sigma_{z,eff} \sim a_l^P, \tag{5.28}$$

regardless of whether $a_l^D \gg a_l^P$ or $a_l^D \ll a_l^P$. This condition requires the two neutrinos to be produced with a separation along the parallel direction smaller than the production processes' spatial resolution a_l^P. Therefore, the inability to distinguish the two neutrinos by the localization of detection and production processes is essential to the interference effect.

On the other hand, the same analysis leading to Eq. (5.27)-(5.28) can be applied to $\left|\Delta k_0^P\right|$ and $\left|\Delta k_0^D\right|$ as well. By assuming the maximally allowed value $\sigma_{z,eff}$ for $\left|t_2 - t_1 - \Delta_{D,\parallel}\right|$ and $\left|\Delta_{P,\parallel} - t_0\right|$ in Eq. (5.24) as well as combining with Eq. (5.23), the inequalities are found to be

$$\left|\Delta k_0^P\right| \lesssim \min\left(1, \frac{a_l^D}{a_l^P}\right) \times \sigma_{k,eff} \sim \frac{1}{2a_l^P} \text{ and} \tag{5.29a}$$

$$\left|\Delta k_0^D\right| \lesssim \min\left(1, \frac{a_l^P}{a_l^D}\right) \times \sigma_{k,eff} \sim \frac{1}{2a_l^D}, \tag{5.29b}$$

regardless of whether $a_l^D \gg a_l^P$ or $a_l^D \ll a_l^P$. As shown above, it is also crucial for the interference effect that the WP states cannot be distinguished by their momenta. In Eq. (5.27)-(5.29), the smallest (most strict) upper bound for each quantity is presented; although these upper bounds are not required to be satisfied all at once by the original conditions shown in shown in Eq. (5.21), (5.23), and (5.24), they clearly indicate that the interference effect is closely tied with the particles' indistinguishability.

The last piece of the puzzle can be uncovered by the condition shown in Eq. (5.25). As discussed in Sec. 4.3, the detection process finds the incoming wave train with a momentum pointing in a direction consistent with that defined

in a ballistic sense. In the case of pair-detection, the two neutrinos are found to have momenta pointing in very similar directions; the perpendicular component of the momentum difference between the two neutrinos is estimated to be $\delta k_\perp \approx k_0^D \times \Delta_{P,\perp}/L_0$, where $\Delta_{P,\perp}/L_0$ is the apparent angle of the production process pair as seen at the detection site. The term

$$\xi \bar{k}_0^P + (1-\xi)\bar{k}_0^D = \frac{1}{4}\left(k_{eff}^{P_1 D_1} + k_{eff}^{P_2 D_2} + k_{eff}^{P_1 D_2} + k_{eff}^{P_2 D_1}\right) \tag{5.30}$$

represents the arithmetic average of the four effective momenta (see Eq. (5.8) and Eq. (5.16)) and, to a very good approximation, $\xi \bar{k}_0^P + (1-\xi)\bar{k}_0^D \approx k_0^{D_1} \approx k_0^{D_2}$ since the momentum widths are expected to be small. Therefore, the condition in Eq. (5.25) can be translated to

$$\delta k_\perp \Delta_{D,\perp} \lesssim 1. \tag{5.31}$$

Furthermore, the detection processes also find the parallel momentum difference and spatial separation between the two neutrinos to be, respectively, $\delta k_\parallel \sim \left|\Delta k_0^D\right|$ and $\left|t_2 - t_1 - \Delta_{D,\parallel}\right|$. With Eq. (5.27), Eq. (5.29), and Eq. (5.31) squared, such pair-detection renders the two neutrinos in a phase space volume

$$\delta^3\vec{k} \times \delta^3\vec{r} \lesssim 1, \tag{5.32}$$

where the upper bound is to be compared with the minimal phase space volume $(2\pi)^3$ occupied by a quantum particle. Although this upper bound may appear as a poor numerical match with $(2\pi)^3 \approx 250$, the minimal phase space volume[2] of a quantum particle, the result shown in Eq. (5.32) is in fact remarkable since the derived upper bound for the phase space volume would have been comparable to $(2\pi)^3$ had we chosen a more realistic range of a few "σ" ($\Leftrightarrow \pm(1 \sim 2) \times \sigma$ around the mean value) for each of the six momentum and position intervals.

It is clear at this point that, through tedious mathematical derivation, the Pauli exclusion principle is manifested by the interference effect in the wave mechanics. The HBT effect does not require any coherence between the pair of

[2] The minimal volume is $h^3 = (2\pi\hbar)^3$, where h is the Planck's constant. Since $\hbar = 1$ in natural units, the phase space volume is $(2\pi)^3$.

production processes or between the pair of detection processes; therefore, macroscopic separation in time and in space between either pair is allowed as long as the spatial and kinematical indistinguishability between the two neutrinos is maintained and the geometrical criteria is satisfied. In the next chapter, we shall estimate whether it is possible to observe this HBT effect for neutrinos in a practical experimental setting.

Chapter 6

Possibility of Observing Neutrino HBT Effect

As discussed in Chap. 4, a massless neutrino WP maintains constant longitudinal width and angular size as it propagates away from the source at the speed of light. One can imagine that if the production rate of the source is high enough the neutrino wave functions start to overlap among themselves and, in other words, a "traffic jam" of neutrinos occurs. It has been demonstrated in Chap. 5 that the issue of indistinguishability, hence the interference effect, may arise if the pair-detection process find the two particles in the same phase space cell. However, the interference requires the overlap among neutrino wave functions and such overlap is generally ignored based on the belief that the intensities of neutrino sources are low [69, for example].

To assess the viability of observing the interference among neutrinos, we will develop a simple model [70] to estimate the degree of overlap among WPs from various man-made and astrophysical neutrino sources. Such model is designed with a particular emphasis on the "production" aspect of the problem which means that the model only concerns the constraints from Eq. (5.28) and Eq. (5.29a) as a preliminary assessment of the sources. From this overlap model, we will show that a galactic SN is an interesting candidate source to observe the neutrino HBT

effect from; however, further examination reveals the difficulty of observing such effect even with a next-generation neutrino detector. Our work confirm and shed light on the experimental difficulty as pointed out in [26].

6.1 Definition of the WP Overlap Factor

We assume a point-like source which emits neutrinos randomly at a predictable average rate. For the remaining of the discussion, the energy E_ν of a neutrino WP will be used in place of its mean momentum k_0. In addition, we will suppress the superscript "P" in the width parameters, a_l^P and a_t^P, associated with a production process as this overlap model does not concern the detection of WPs. To begin, we note that a WP mathematically extends to infinity so it is practical to define its size based on the region where it is most likely to be found. According to Eq. (4.27), the probability of finding the neutrino within a volume element is

$$|\Psi_{\text{far}}(\vec{r},t)|^2 \mathrm{d}^3\vec{r} = |\Psi_{1D}(r,t)|^2 \mathrm{d}r \times \Theta(\hat{r})\mathrm{d}\Omega. \tag{6.1}$$

We define the "physical extent" of an evolved WP to be the the volume swept by the fan-shaped strip, as shown in Fig. 6.1, around the neutrino's classical path. The radial width and the angle subtended by the fan-shaped strip are chosen so that each of them corresponds to 95% probability according to the radial and angular probability distributions, respectively. This way, the overall probability of finding the neutrino in the region is approximately 90% ($\approx 0.95^2$). The radial width is $4a_l$ as inferred from the Gaussian form after taking the modulus square of Eq. (4.28). The angle subtended by the fan-shaped strip with respect to the WP's classical path are computed from both Eq. (4.32) and Eq. (4.36) as a comparison; the former angular distribution is an exact result whereas the later is an approximation under the assumption of sharp momentum distribution. The

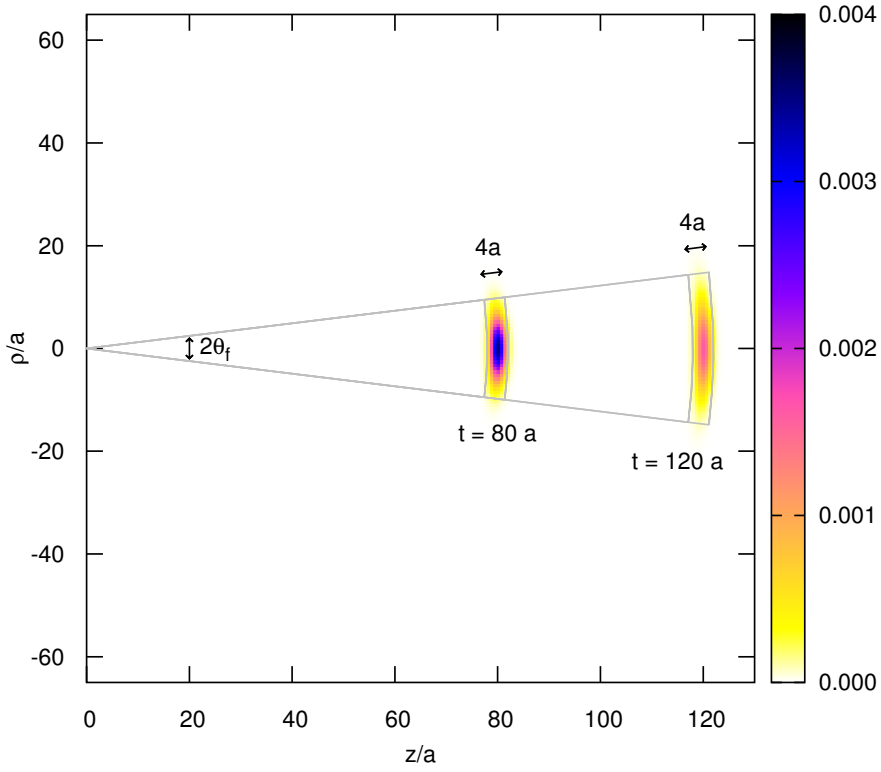

Figure 6.1: The probability density of the WP in the far-field limit at selected times. The WP is assumed to be produced at the origin at $t = 0$ and propagates along z direction. This plot is produced by using Eq. (4.26) and assuming $a_t = a_l = a$ and $E_\nu a_t = 10$. The fan-shaped strips enclosed between two gray sectors correspond to the cross sections of the 90%-probability volumes at the two indicated times. As shown by the strips, the WP maintains constant longitudinal width $4a$ and asymptotically subtends a constant angle with respect to the origin during propagation. All length and time scales are expressed in unit of a.

angle computed from the former is determined numerically and it is denoted as

$$\begin{aligned} &\theta_f = P^{-1}(0.95), \text{ where} \\ &P(\theta_f) \equiv 2\pi \int_0^{\theta_f} S(\theta) \sin\theta \mathrm{d}\theta. \end{aligned} \tag{6.2}$$

On the other hand, the angle from the later can be found from the analytic result of the integration:

$$\begin{aligned} &\theta'_f = P^{-1}_{\text{approx}}(0.95) \approx 1.22 \times (E_\nu a_t)^{-1}, \text{ where} \\ &P_{\text{approx}}(\theta'_f) \equiv 2\pi \int_0^{\theta'_f} \Theta(\theta) \times \theta \times \mathrm{d}\theta = 1 - \exp\left(\frac{-\theta'^2_f}{2 \cdot (2E_\nu a_t)^{-2}}\right). \end{aligned} \tag{6.3}$$

Both θ_f and θ'_f are plotted as functions of $E_\nu a_t$ in Fig. 6.2 which, as a confirmation of our earlier results, clearly demonstrates their convergence at $(E_\nu a_t)^2 \gg 1$. The comparison shows that the simple form of θ'_f suffices to estimate the angular size of the WP and it will be used in the following analysis.

With a well-defined volume for each WP, we can define the criteria for two WPs to be considered as overlapping. Consider an auxiliary sphere centered at the source and a reference WP passes through such sphere at time t_{ref}. In addition, the center of this reference WP propagates along some direction $\hat{r}_{\text{ref}}$. If another WP, with direction $\hat{r}$ and passage time t similarly defined, were to spatially overlap with the reference WP, two criteria must be met:

$$\cos^{-1}(\hat{r} \cdot \hat{r}_{\text{ref}}) < 2\theta'_f \text{ and} \tag{6.4a}$$

$$|t - t_{\text{ref}}| < \tau, \tag{6.4b}$$

where $\tau = 4a_l$ according to our definition of the WP volume. These criteria are illustrated diagrammatically in Fig. 6.3.

Next, we define a positive factor η to quantify the average number of WPs that each WP overlaps with. Let $\mathrm{d}^2\Phi/\mathrm{d}E_\nu\mathrm{d}\Omega$ be the differential rate at which a particular source gives off neutrinos and ΔE be the energy range of neutrinos of

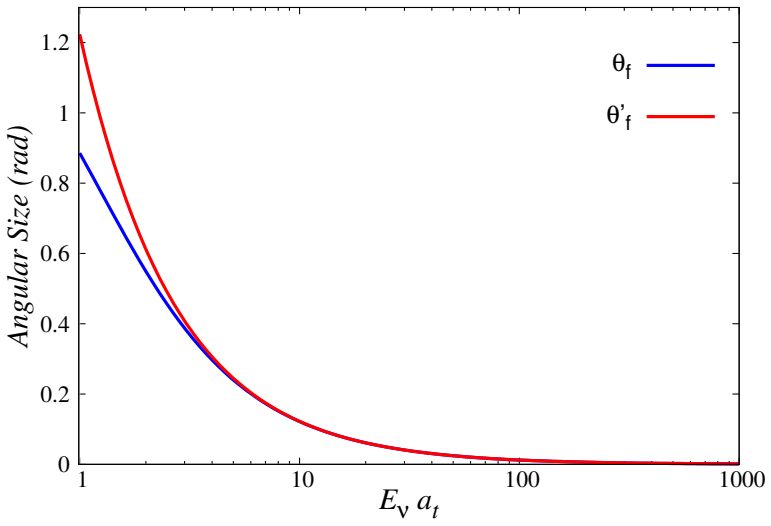

Figure 6.2: The angular size of a WP corresponding to 95% probability from the angular probability distributions as functions of $E_\nu a_t$. The numerical result of θ_f is computed assuming $E_\nu a_l = 100$. In the plot, θ_f is computed from Eq. (6.2) where as θ'_f is derived from Eq. (6.3). As discussed in Sec. 4.3, $S(\theta)$ is independent of a_l if $E_\nu a_l \gg 1$.

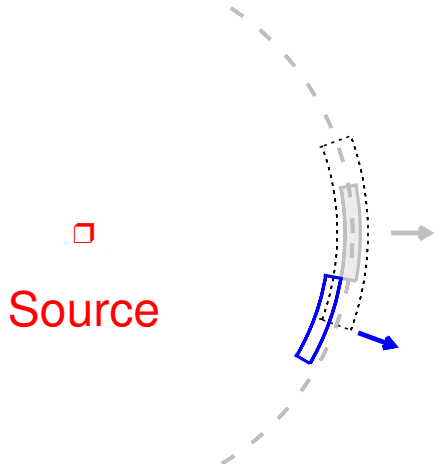

Figure 6.3: Diagrammatic illustration of the overlap criteria. The gray solid strip represents the reference WP, of which the center passes through an auxiliary sphere plotted as the gray dashed circumference. If the other WP (shown as the blue strip) were to overlap, its center must be within the black dotted boundary. Note that the status of being overlapped with each other is independent of time.

relevance. The expected number of WPs satisfying these criteria is

$$\eta \equiv \frac{\mathrm{d}^2\Phi}{\mathrm{d}E_\nu \mathrm{d}\Omega} \times \Delta E \times 2\tau \times \Delta\Omega_{\mathrm{overlap}}, \tag{6.5}$$

where

$$\Delta\Omega_{\mathrm{overlap}} = 4\pi {\theta'_f}^2 \approx 6\pi (E_\nu a_t)^{-2} \tag{6.6}$$

is the solid angle covered by possible $\hat{r}$ according to the criterion Eq. (6.4a). In addition to spatial overlap, their overlap in momentum space is ensured by $\Delta\Omega_{\mathrm{overlap}}$ and ΔE, which respectively concern the overlap of transverse and longitudinal momentum components. By expanding the massless energy-momentum relation $E_\nu = |\vec{k}|$ with the WP momentum distribution from Eq. (4.3), it can be shown that the energy uncertainty of a WP,

$$\sigma_E = \sqrt{(2a_l)^{-2} + (4E_\nu a_t^2)^{-2}} \approx \frac{1}{2a_l}, \tag{6.7}$$

receives dominant contribution from the longitudinal momentum uncertainty under the assumption shown in Eq. (4.18). Therefore, by choosing $\Delta E = 4\sigma_E = 2/a_l$, the overlap factor η counts the average number of neutrinos that are indistinguishable from the chosen reference WP. We notice that the dependence on a_l from τ and from ΔE immediately cancels and the overlap factor reduces to

$$\eta \sim \frac{\mathrm{d}^2\Phi}{\mathrm{d}E_\nu \mathrm{d}\Omega} \times \frac{96\pi}{(E_\nu a_t)^2} \ll 96\pi \times \frac{\mathrm{d}^2\Phi}{\mathrm{d}E_\nu \mathrm{d}\Omega}. \tag{6.8}$$

We remark that the numerical factor in Eq. (6.8) is in fact up to the exact definition of "overlap", but the order of magnitude of η should nevertheless provide a clear indication of the neutrino "traffic jam". Also, for the reference, the consideration of ΔE and τ in fact correspond to the HBT effect conditions shown in Eq. (5.28) and Eq. (5.29a).

6.2 How Large Is the Initial WP?

An *ab initio* calculation of the initial WP size is difficult due to our limited knowledge of the details of the production process (the same also applies to the

detection process). The overlap factor depends on only one of the position widths, a_t, as shown in Eq. (6.8). While the longitudinal width a_l can easily exceed the position uncertainty of the neutrino production vertex if the temporal localization of the process is loose [6], the transverse width a_t should more or less reflect the position localization of the parent particle and other entangled daughter particles involved in the production process. A rigorous treatment should take into account the interaction of the involved particles with the environment as the position widths of the neutrino simply reflect its momentum uncertainty inherited from other involved particles. We find very limited literature on this subject and only a recent theoretical work [71] using decoherence theory [72, 73] addresses this issue in the context of accelerator neutrino experiment. We refrain from delving into the determination of a_t as it is beyond the scope of this work. Instead, we will leave a_t (or equivalently $E_\nu a_t$) as a free parameter in the following discussion.

6.3 Overlap Estimate for Various Sources

Based on Eq. (6.8), we perform an order-of-magnitude estimate on the overlap factor for various neutrino sources. The estimate here can only yield the upper bound of η since no specific assumption on the value of a_t is made except that $E_\nu a_t \gg 1$.

Accelerator

In accelerator experiments, high energy protons hit a stationary target to produce mesons which subsequently decay to produce muon neutrinos or anti-neutrinos. Protons arrive at the target bunch by bunch, resulting in peaked structures in the instantaneous proton-on-target (POT) rate. The mesons (mostly pions) and the neutrinos travel at approximately the speed of light down the beamline, so, to an observer far away, the instantaneous neutrino production rate retains similar time structure to the instantaneous POT rate. As an example, we take the parameters of the low energy configuration of the NuMI beam [74, 75] for the following

estimate.

There are approximately 500 bunches in each NuMI spill and each spill delivers a total of 2×10^{13} protons. The time width of each bunch is of order 1 nsec. This corresponds to an instantaneous POT rate about 4×10^{19} POT $\cdot$ s^{-1}. The ν_μ charged current event spectrum (unoscillated) peaks at $E_\nu = 3$ GeV, at which each POT results in approximately $10^{-3}\,\nu_\mu$ GeV^{-1} passing through the near detector [74]. Neglecting neutrinos that are not intercepted by the near detector for simplicity, the effective energy-differential production rate of neutrinos is $\mathrm{d}\Phi/\mathrm{d}E_\nu \sim 4 \times 10^{16}$ GeV$^{-1} \cdot$ s^{-1}. We estimate $\Delta\Omega_{\mathrm{source}}$ to be the solid angle subtended by the near detector with respect to the mean decay location of pions in the decay pipe. The mean distance traveled by the pions of Lorentz factor $\gamma \sim 50$, which dominantly contribute to those 3 GeV neutrinos, before they decay is about 400 m. The near detector is approximately a cylinder of radius 2 m and locates at 1 km away from the upstream end of the pipe. Therefore, $\Delta\Omega_{\mathrm{source}} \sim 10^{-5}\pi$. Since the characteristic decay angle of these pions is much greater than the near detector's angular size, the neutrino flux can be treated as uniform within $\Delta\Omega_{\mathrm{source}}$. Finally, the overlap factor is estimated to be $\eta \sim 0.3 \times (E_\nu a_t)^{-2}$.

Fission Reactor

A reactor core is a strong and isotropic source for electron anti-neutrinos at MeV range [76, 77]. The typical measured spectrum of $\bar{\nu}_e$ ranges from 1.8 MeV to 8 MeV with a peak at $E_\nu = 3.6$ MeV. The energy-differential production rate $\mathrm{d}\Phi/\mathrm{d}E_\nu$ decreases with neutrino energy. For a typical commercial reactor core with 3 GW thermal power, $\mathrm{d}\Phi/\mathrm{d}E_\nu \sim 10^{20}\,\mathrm{MeV}^{-1} \cdot \mathrm{s}^{-1}$ at $E_\nu = 3.6$ MeV. The overlap factor is then $\eta \sim 1.6 \times (E_\nu a_t)^{-2}$.

The Sun

Thermal nuclear fusion processes take place in the solar core and result in a huge electron neutrino flux. The energy-differential rate of solar neutrino production is

$10^{32}\,\mathrm{MeV}^{-1}\mathrm{s}^{-1} \lesssim \mathrm{d}\Phi/\mathrm{d}E_\nu \lesssim 10^{39}\,\mathrm{MeV}^{-1}\mathrm{s}^{-1}$ in the energy range $0.1\,\mathrm{MeV} < E_\nu < 10\,\mathrm{MeV}$ [78]. The corresponding estimate for the overlap factor in the energy range is $\eta \sim (10^{12} - 10^{19}) \times (E_\nu a_t)^{-2}$.

Supernova

As discussed in Chap. 2, most of the gravitational energy of a SN is carried away by neutrinos, resulting in an astonishing neutrino flux soon after the onset of collapse. Taking a $M = 20M_\odot$ core-collapse SN [79] as an example, the differential rate of $\bar{\nu}_e$ emission is of order $10^{52}\ \mathrm{MeV}^{-1}\mathrm{s}^{-1} \lesssim \mathrm{d}\Phi/\mathrm{d}E_\nu \lesssim 10^{56}\ \mathrm{MeV}^{-1}\mathrm{s}^{-1}$ for $4\ \mathrm{MeV} < E_\nu < 40\ \mathrm{MeV}$ at the time $0.1\ \mathrm{s} < t < 10\ \mathrm{s}$ after the onset of collapse. Similar to the solar neutrino case, a huge overlap factor is obtained: $\eta \sim (10^{32} - 10^{36}) \times (E_\nu a_t)^{-2}$.

We summarize the above estimates in Table 6.1. With the assumption of sharp momentum distribution, we can conclude from the above estimate that the overlap is negligible for accelerator and reactor neutrinos without knowing the transverse width a_t. For astrophysical sources, on the other hand, any reasonable guess on the value of a_t would conclude significant overlap. For instance, taking a_t as the mean interparticle distance of order $\mathcal{O}(10^{-11}\mathrm{m})$ estimated from the solar core density ($150\ \mathrm{g/cm}^3$) along with, say, $E_\nu = 10$ MeV would result in $\eta \sim 10^8$. Needless to say, the overlap among SN neutrino WPs is even more dramatic.

In addition to the overlap factor, the interference condition concerning the source and detector sizes shown in Eq. (5.25) is also examined for each source with

Source	$d^2\Phi/dE_\nu d\Omega$ ($\mathrm{MeV}^{-1}\ \mathrm{s}^{-1}\ \mathrm{sr}^{-1}$)	$\eta(k_0 a_t)^2$	L_0 (m)	E_ν (MeV)	HBT Setup (Eq. (5.25))
accelerator	10^{18}	0.1	10^6	10^3	No
reactor	10^{19}	1	10^3–10^5	1	No
sun	10^{32}–10^{38}	10^{13}–10^{19}	10^{11}	0.1–10	No
supernova	10^{51}–10^{55}	10^{32}–10^{36}	10^{20}	10	Yes

Table 6.1: Characteristics of various neutrino sources relevant for the overlap estimate. All numbers presented here are order-of-magnitude estimates.

the corresponding typical detector size; the results are listed in the last column of Table 6.1. Among the investigated neutrino sources, a galactic SN seems to be a promising candidate source for neutrino HBT effect after having examined the conditions Eq. (5.25), Eq. (5.28), and Eq. (5.29a) so far. The remaining question to answer is if the relevant event rate, which involves the detection aspect of the problem, is strong enough to allow experimenters to observe the anti-bunching of events.

6.4 HBT Effect for Supernova Neutrinos?

In our local galaxy, about three core-collapse SN events at an average distance 10 kpc from the Earth are expected every century [80]. At such distance, the condition Eq. (5.25) is satisfied by the typical proto-neutron star radius $\Delta_{P,\perp} \sim$ 10 km, $E_\nu \sim 10$ MeV, and a megaton water Cherenkov detector size of order $\Delta_{D,\perp} \sim 100$ m such as the one planned in the Hyper-Kamiokande experiment [81] to be operated in the near future. Optimistically, such galactic SN event would result in up to $\sim 10^6$ events in the megaton detector. Most of these events would be observed during the first few seconds and over an energy range ~ 10 MeV. Therefore, an optimal estimate on the energy-differential event rate is

$$\frac{\mathrm{d}^2 N}{\mathrm{d}E_\nu \mathrm{d}t} \sim \frac{10^6}{10\ \mathrm{MeV} \cdot 1\ \mathrm{sec}} \sim 10^{-16}, \tag{6.9}$$

where we express the differential rate in a dimensionless form ($\hbar \approx 6.6 \times 10^{-22}$ MeV$\cdot$ sec) and assume that the rate is constant over time and energy for simplicity. Without any interference effect, the observed events simply follow Poisson distribution. With the interference effect, however, the probability of observing two events close in time and in energy decreases compared to that expected by Poisson statistics.

We recall the conditions associated with the detection process for the interference effect shown in Eq.(5.27) and Eq. (5.29b). The former condition is equivalent

to

$$t_1 + \Delta_{D,\|} - a_l^D \lesssim t_2 \lesssim t_1 + \Delta_{D,\|} + a_l^D, \tag{6.10}$$

which suggests an interference time window of width $\sim a_l^D$. This time window is actually shifted with $\Delta_{D,\|}$ but, nonetheless, the width is independent of $\Delta_{D,\|}$. The later condition, on the other hand, suggests an energy interval of width $\sim 1/a_l^D$. Given a detected event, a time interval[1] as well as an energy interval surrounding that event can be defined. If Poisson statistics were the case, a small but nonzero number of events is predicted to be found in that 2D time-energy interval whereas, if there is an interference effect, no events will be found. With Poisson statistics, one expects to find a number

$$\frac{\mathrm{d}^2 N}{\mathrm{d}E_\nu \mathrm{d}t} \times \delta E_\nu \times \delta t \sim 10^{-16} \tag{6.11}$$

of events in the time-energy interval corresponding to each detected event. Since there are $\sim 10^6$ detected events, the expected number of to-be-correlated pair is $10^6 \times 10^{-16} = 10^{-10}$. Even with the knowledge of the value of a_l^D (such that a well defined time window can be used to search for correlated events) and with perfect time and energy resolution of the detector, there is obviously no experimental sensitivity to the interference effect. Due to the weakly interacting nature of neutrinos, as remarked in [26], the observation of the neutrino HBT effect would require a fundamental paradigm shift of how neutrinos are detected.

[1] Strictly speaking, it should be a set of time intervals corresponding to the location in the detector where the correlated event is searched.

Chapter 7

Conclusion

In the first part of this thesis (Chap. 2 and Chap. 3), we find that the rapid cooling of the PNS prescribed by the newly implemented convection treatment in the 1D hydrodynamic simulation of [30] does not agree well with the SN1987A data, particularly with the events K10-K12 in the KAM-II data set (see Table 3.1 and Table 3.2). Given the rather limited statistics of the SN1987A data, a few plausible explanations are as follows:

1. A relatively less probable outcome had been measured by chance by the KAM-II experiment during the SN1987A neutrino burst. The state-of-the-art 1D simulations of PNS cooling accurately predict the neutrino luminosities.

2. The KAM-II data set was a statistically probable outcome. The 1D simulations mischaracterize the cooling rate of the PNS such that the predicted neutrino luminosities fall off early. Model adjustments are necessary to slow down the cooling.

3. The KAM-II data set was a statistically probable outcome and the 1D simulations accurately characterize the PNS cooling. However, these simulations neglect fallback materials which contributed to additional neutrino luminosity observed by the KAM-II experiment.

As the current 1D SN simulations are still subject to theoretical and modeling uncertainties, the implications we derive from the SN1987A data in light of the latest simulation models can provide valuable inputs to future research.

In the second part of thesis (Chap. 4 - Chap. 6), we discuss the quantum mechanical aspect of neutrino detection. With the solution of the 3D Gaussian WP, namely Eq. (4.26), we elaborate on the concept of wave-particle duality in 3D space. Applying this concept to the detection of such WP at a distance far away from the source, we derive the transition amplitude, Eq. (5.6), which reflects approximate conservation of momentum and causality. This transition amplitude is subsequently applied to calculating the interference term in the joint-detection probability as shown in Eq. (5.19). We analyze the conditions for observing the interference effect known as the HBT effect. We find that an observable interference requires the joint-detection to render the two particles in the same phase space cell and that such effect does not require any coherence between the two production processes or between the two detection processes. After all, the interference effect simply reflects the exchange symmetry of fundamental particles. In the last chapter, we explore the possibility of observing such interference effect in neutrino experiments and reach a conclusion that it is extremely difficult, if not impossible, to observe such effect in practical experimental settings.

References

[1] S. E. Woosley, A. Heger, and T. A. Weaver. The evolution and explosion of massive stars. *Rev. Mod. Phys.*, 74:1015–1071, 2002.

[2] E. Baron and J. Cooperstein. The effect of iron core structure on supernovae. *The Astrophysical Journal*, 353:597–611, April 1990.

[3] Hans-Thomas Janka. Explosion Mechanisms of Core-Collapse Supernovae. *Ann. Rev. Nucl. Part. Sci.*, 62:407–451, 2012.

[4] C. Patrignani et al. Review of Particle Physics. *Chin. Phys.*, C40(10):100001, 2016.

[5] Boris Kayser. On the Quantum Mechanics of Neutrino Oscillation. *Phys. Rev.*, D24:110, 1981.

[6] S. Nussinov. Solar Neutrinos and Neutrino Mixing. *Phys. Lett.*, B63:201–203, 1976.

[7] C. Giunti, C. W. Kim, and U. W. Lee. When do neutrinos really oscillate?: Quantum mechanics of neutrino oscillations. *Phys. Rev.*, D44:3635–3640, 1991.

[8] Ken Kiers, Shmuel Nussinov, and Nathan Weiss. Coherence effects in neutrino oscillations. *Phys. Rev.*, D53:537–547, 1996, hep-ph/9506271.

[9] C. Giunti and C. W. Kim. Coherence of neutrino oscillations in the wave packet approach. *Phys. Rev.*, D58:017301, 1998, hep-ph/9711363.

[10] Marek Zralek. From kaons to neutrinos: Quantum mechanics of particle oscillations. *Acta Phys. Polon.*, B29:3925–3956, 1998, hep-ph/9810543.

[11] J. Rich. The Quantum mechanics of neutrino oscillations. *Phys. Rev.*, D48:4318–4325, 1993.

[12] C. Giunti, C. W. Kim, J. A. Lee, and U. W. Lee. On the treatment of neutrino oscillations without resort to weak eigenstates. *Phys. Rev.*, D48:4310–4317, 1993, hep-ph/9305276.

[13] W. Grimus and P. Stockinger. Real oscillations of virtual neutrinos. *Phys. Rev.*, D54:3414–3419, 1996, hep-ph/9603430.

[14] C. Giunti, C. W. Kim, and U. W. Lee. When do neutrinos cease to oscillate? *Phys. Lett.*, B421:237–244, 1998, hep-ph/9709494.

[15] W. Grimus, P. Stockinger, and S. Mohanty. The Field theoretical approach to coherence in neutrino oscillations. *Phys. Rev.*, D59:013011, 1999, hep-ph/9807442.

[16] Christian Y. Cardall. Coherence of neutrino flavor mixing in quantum field theory. *Phys. Rev.*, D61:073006, 2000, hep-ph/9909332.

[17] Mikael Beuthe. Oscillations of neutrinos and mesons in quantum field theory. *Phys. Rep.*, 375:105–218, 2003, hep-ph/0109119.

[18] M. Beuthe. Towards a unique formula for neutrino oscillations in vacuum. *Phys. Rev.*, D66:013003, 2002, hep-ph/0202068.

[19] Evgeny Kh. Akhmedov and Alexei Yu. Smirnov. Paradoxes of neutrino oscillations. *Phys. Atom. Nucl.*, 72:1363–1381, 2009, 0905.1903.

[20] R. Hanbury Brown and R. Q. Twiss. Interferometry of the intensity fluctuations in light. i. basic theory: The correlation between photons in coherent beams of radiation. *Proc. R. Soc. London, Sec. A*, 242(1230):300–324, 1957.

[21] R. Hanbury Brown and R. Q. Twiss. Interferometry of the intensity fluctuations in light ii. an experimental test of the theory for partially coherent light. *Proc. R. Soc. London, Sec. A*, 243(1234):291–319, 1958.

[22] U. Fano. Quantum theory of interference effects in the mixing of light from phase-independent sources. *Am. J. Phys.*, 29(8):539–545, 1961.

[23] Urs Achim Wiedemann and Ulrich Heinz. Particle interferometry for relativistic heavy-ion collisions. *Phys. Rep.*, 319(45):145 – 230, 1999.

[24] Harald Kiesel, Andreas Renz, and Franz Hasselbach. Observation of hanbury brown-twiss anticorrelations for free electrons. *Nature*, 418(6896):392–394, Jul 2002.

[25] T. Jeltes et al. Comparison of the hanbury brown-twiss effect for bosons and fermions. *Nature*, 445(7126):402–405, Jan 2007.

[26] Thomas D. Gutierrez. Distinguishing between dirac and majorana neutrinos with two-particle interferometry. *Phys. Rev. Lett.*, 96:121802, Mar 2006.

[27] Warren P. Wright and James P. Kneller. Neutrino intensity interferometry: Measuring protoneutron star radii during core-collapse supernovae. *Phys. Rev. Lett.*, 119:051101, Aug 2017.

[28] Hans A. Bethe and R. Wilson, James. Revival of a stalled supernova shock by neutrino heating. *Astrophys. J.*, 295:14–23, 1985.

[29] Carlo Giunti and Chung W. Kim. *Fundamentals of Neutrino Physics and Astrophysics*. 2007.

[30] Alessandro Mirizzi et al. Supernova Neutrinos: Production, Oscillations and Detection. *Riv. Nuovo Cim.*, 39(1-2):1, 2016.

[31] Bernhard Mller, Hans-Thomas Janka, and Alexander Heger. New two-dimensional models of supernova explosions by the neutrino-heating mechanism: Evidence for different instability regimes in collapsing stellar cores. *The Astrophysical Journal*, 761(1):72, 2012.

[32] James M. Lattimer and F. Douglas Swesty. A generalized equation of state for hot, dense matter. *Nucl. Phys. A*, 535(2):331 – 376, 1991.

[33] A. W. Steiner, M. Hempel, and T. Fischer. Core-collapse supernova equations of state based on neutron star observations. *Astrophys. J.*, 774(1):17, 2013.

[34] K. Hirata et al. Observation of a neutrino burst from the supernova sn1987a. *Phys. Rev. Lett.*, 58:1490–1493, Apr 1987.

[35] K. Hirata et al. Observation in the kamiokande-ii detector of the neutrino burst from supernova sn1987a. *Phys. Rev. D*, 38:448–458, Jul 1988.

[36] R. M. Bionta et al. Observation of a neutrino burst in coincidence with supernova 1987a in the large magellanic cloud. *Phys. Rev. Lett.*, 58:1494–1496, Apr 1987.

[37] C. B. Bratton et al. Angular distribution of events from sn1987a. *Phys. Rev. D*, 37:3361–3363, Jun 1988.

[38] W. C. Haxton. The Nuclear Response of Water Cherenkov Detectors to Supernova and Solar Neutrinos. *Phys. Rev.*, D36:2283, 1987.

[39] Alessandro Strumia and Francesco Vissani. Precise quasielastic neutrino/nucleon cross-section. *Phys. Lett. B*, 564(12):42 – 54, 2003.

[40] H.-T. Janka and W. Hillebrandt. Neutrino emission from type II supernovae - an analysis of the spectra. *Astronomy & Astrophysics*, 224:49–56, October 1989.

[41] Mathias Th. Keil, Georg G. Raffelt, and Hans-Thomas Janka. Monte carlo study of supernova neutrino spectra formation. *Astrophys. J.*, 590(2):971, 2003.

[42] Irene Tamborra et al. High-resolution supernova neutrino spectra represented by a simple fit. *Phys. Rev. D*, 86:125031, Dec 2012.

[43] Cecilia Lunardini and Alexei Yu Smirnov. Probing the neutrino mass hierarchy and the 13-mixing with supernovae. *JCAP*, 2003(06):009, 2003.

[44] A. Burrows. Supernova neutrinos. *Astrophys. J.*, 334:891, 1988.

[45] Cecilia Lunardini and Alexei Yu. Smirnov. Neutrinos from sn1987a: flavor conversion and interpretation of results. *Astropart. Phys.*, 21(6):703 – 720, 2004.

[46] Beat Jegerlehner, Frank Neubig, and Georg Raffelt. Neutrino oscillations and the supernova 1987a signal. *Phys. Rev. D*, 54:1194–1203, Jul 1996.

[47] K. S. Hirata et al. Real-time, directional measurement of ^{8}B solar neutrinos in the kamiokande ii detector. *Phys. Rev. D*, 44:2241–2260, Oct 1991.

[48] E.N. Alexeyev et al. Detection of the neutrino signal from sn 1987a in the lmc using the inr baksan underground scintillation telescope. *Phys. Lett. B*, 205(2):209 – 214, 1988.

[49] Thomas J. Loredo and Donald Q. Lamb. Bayesian analysis of neutrinos observed from supernova sn 1987a. *Phys. Rev. D*, 65:063002, Feb 2002.

[50] Thomas J. Loredo and Donald Q. Lamb. Neutrinos from sn 1987a - implications for cooling of the nascent neutron star and the mass of the electron antineutrino. *Ann. N. Y. Acad. Sci.*, 571:601–630, 1989.

[51] K. S. Hirata et al. Observation of ^{8}B solar neutrinos in the kamiokande-ii detector. *Phys. Rev. Lett.*, 63:16–19, Jul 1989.

[52] G. Pagliaroli et al. Improved analysis of {SN1987A} antineutrino events. *Astropart. Phys.*, 31(3):163 – 176, 2009.

[53] R. M. Bionta et al. Search for proton decay into $e^+\pi^0$. *Phys. Rev. Lett.*, 51:27–30, Jul 1983.

[54] Peter J. Kernan and Lawrence M. Krauss. Updated limits on the electron neutrino mass and large angle oscillations from {SN1987A}. *Nucl. Phys. B*, 437(1):243 – 256, 1995.

[55] W. David Arnett, John N. Bahcall, Robert P. Kirshner, and Stanford E. Woosley. Supernova 1987a. *Annual Review of Astronomy and Astrophysics*, 27(1):629–700, September 1989.

[56] Glen Cowan. *Statistical data analysis*. Oxford science publications. Clarendon Press ; Oxford University Press, Oxford : New York, 1998.

[57] Alessandro Mirizzi and Georg G. Raffelt. Analysis of the sn 1987a neutrinos with a flexible spectral shape. *Phys. Rev. D*, 72:063001, Sep 2005.

[58] Cecilia Lunardini. The diffuse supernova neutrino flux, supernova rate and {SN1987A}. *Astropart. Phys.*, 26(3):190 – 201, 2006.

[59] Tobias Fischer et al. Probing axions with the neutrino signal from the next galactic supernova. *Phys. Rev. D*, 94:085012, Oct 2016.

[60] Chris L. Fryer. Neutrinos from fallback onto newly formed neutron stars. *The Astrophysical Journal*, 699(1):409, 2009.

[61] S.E. Woosley and A. Heger. Nucleosynthesis and remnants in massive stars of solar metallicity. *Physics Reports*, 442(1):269 – 283, 2007. The Hans Bethe Centennial Volume 1906-2006.

[62] Carlos Almeida and Arthur Jabs. Spreading of a Relativistic Wave Packet. *Am. J. Phys*, 52:921–925, 1984.

[63] I.P. Christov. Propagation of Femtosecond Light Pulses. *Opt. Commun.*, 53:364 – 366, 1985.

[64] A. E. Bernardini and S. De Leo. Analytic Approach to the Wave Packet Formalism in Oscillation Phenomena. *Phys. Rev. D*, 70:053010, Sep 2004.

[65] Mark Andrews. The Evolution of Free Wave Packets. *Am. J. Phys*, 76:1102–1107, 2008.

[66] Dmitry V. Naumov and Vadim A. Naumov. Neutrino Velocity Anomalies: A Resolution without a Revolution. 2011, 1110.0989.

[67] Denis Bernard. Comment on: 'Neutrino Velocity Anomalies: A Resolution without a Revolution'. 2011, 1110.2321.

[68] Cheng-Hsien Li and Yong-Zhong Qian. A Pedagogical Discussion on Neutrino Wave-Packet Evolution. *Phys. Procedia*, 61:724–728, 2015, 1404.1408.

[69] Leo Stodolsky. The Unnecessary wave packet. *Phys. Rev.*, D58:036006, 1998, hep-ph/9802387.

[70] Cheng-Hsien Li and Yong-Zhong Qian. Do Neutrino Wave Functions Overlap and Does it Matter? In *Prospects in Neutrino Physics (NuPhys2015) London, UK, December 16-18, 2015*, 2016, 1605.00344.

[71] B. J. P. Jones. Dynamical pion collapse and the coherence of conventional neutrino beams. *Phys. Rev.*, D91(5):053002, 2015, 1412.2264.

[72] Erich Joos et al. *Decoherence and the appearance of a classical world in quantum theory*. Springer Science & Business Media, 2013.

[73] Maximilian A Schlosshauer. *Decoherence: and the quantum-to-classical transition*. Springer Science & Business Media, 2007.

[74] P. Adamson et al. Study of muon neutrino disappearance using the fermilab main injector neutrino beam. *Phys. Rev. D*, 77:072002, Apr 2008.

[75] P. Adamson et al. The numi neutrino beam. *Nucl. Instrum. Methods, Sec. A*, 806:279 – 306, 2016.

[76] Th. A. Mueller et al. Improved Predictions of Reactor Antineutrino Spectra. *Phys. Rev.*, C83:054615, 2011, 1101.2663.

[77] P. Vogel, L. J. Wen, and C. Zhang. Neutrino oscillation studies with reactors. *Nature Commun.*, 6, Apr 2015.

[78] W. C. Haxton, R. G. Hamish Robertson, and Aldo M. Serenelli. Solar Neutrinos: Status and Prospects. *Ann. Rev. Astron. Astrophys.*, 51:21–61, 2013, 1208.5723.

[79] T. Totani et al. Future detection of supernova neutrino burst and explosion mechanism. *Astrophys. J.*, 496(1):216, 1998.

[80] Scott M. Adams et al. Observing the next galactic supernova. *Astrophys. Journal*, 778(2):164, 2013.

[81] K. Abe et al. Letter of Intent: The Hyper-Kamiokande Experiment — Detector Design and Physics Potential —. 2011, 1109.3262.

[82] Peter W Milonni and Joseph H Eberly. *Lasers*. John Wiley & Sons, 1988.

Appendix A

Conditional Distribution of Poisson Variables

We summarize some properties of Poisson variables and show that a set of Poisson variables will follow multinomial distribution under the condition that their sum is fixed. Let upper case X be a Poisson variable, lower case $x \in \{0, 1, 2, \dots\}$ be its outcome, and $\lambda = E[X]$ be the expectation value. The probability of getting a particular outcome x is governed by Poisson distribution

$$Pr(X = x) = \frac{\lambda^x \exp(-\lambda)}{x!}, \tag{A.1}$$

which satisfies the normalization condition $\sum_{x=0}^{\infty} Pr(X = x) = 1$.

An important property is that the sum of two Poisson variables is also a Poisson variable. Let us use subscript $i \in \{1, 2\}$ to differentiate between two Poisson variables and define the third random variable $Y \equiv X_1 + X_2$ to denote their sum. The probability of getting a particular outcome $y \in \{0, 1, 2 \dots\}$ is then

$$
\begin{aligned}
Pr(Y=y) &= \sum_{x_1=0}^{\infty}\sum_{x_2=0}^{\infty} \frac{\lambda_1^{x_1}\exp(-\lambda_1)}{x_1!} \times \frac{\lambda_2^{x_2}\exp(-\lambda_2)}{x_2!} \times \delta_{y,(x_1+x_2)} \\
&= \exp\left\{-(\lambda_1+\lambda_2)\right\} \sum_{x_1=0}^{y} \frac{\lambda_1^{x_1}}{x_1!} \times \frac{\lambda_2^{y-x_1}}{(y-x_1)!} \\
&= \frac{\exp\left\{-(\lambda_1+\lambda_2)\right\}}{y!} \sum_{x_1=0}^{y} \frac{y!}{x_1!(y-x_1)!} \times \lambda_1^{x_1}\lambda_2^{y-x_1} \\
&= \frac{(\lambda_1+\lambda_2)^y \exp\left\{-(\lambda_1+\lambda_2)\right\}}{y!},
\end{aligned}
\tag{A.2}
$$

which clearly shows that Y is a Poisson variable with expectation value $\lambda_1+\lambda_2$. This, of course, can be generalized to the sum of an arbitrarily number of Poisson variables.

Now suppose we have k Poisson variables and recall the conditional probability formula, $P(A\big|B) = P(A\cap B)/P(B)$. Under the condition that their sum is a fixed number n, the probability mass function of these k Poisson variables can be deduced to be a multinomial distribution

$$
\begin{aligned}
&Pr\left(X_1=x_1, X_2=x_2, \ldots \Big| \sum_{i=1}^{k} x_i = n\right) \\
&= \frac{Pr\left(X_1=x_1, X_2=x_2, \ldots\right) \times \delta_{n,(x_1+x_2+\cdots+x_k)}}{Pr\left(\sum_{i=1}^{k} x_i = n\right)} \\
&= \delta_{n,(x_1+x_2+\cdots+x_k)} \times \left(\prod_{i=1}^{k} \frac{\lambda_i^{x_i}\exp(-\lambda_i)}{x_i!}\right) \Big/ \left(\frac{\lambda_{sum}^{n}\exp(-\lambda_{sum})}{n!}\right) \\
&= \delta_{n,(x_1+x_2+\cdots+x_k)} \times n! \times \prod_{i=1}^{k} \frac{\left(\lambda_i/\lambda_{sum}\right)^{x_i}}{x_i!} = \delta_{n,(x_1+x_2+\cdots+x_k)} \times n! \times \prod_{i=1}^{k} \frac{p_i^{x_i}}{x_i!},
\end{aligned}
\tag{A.3}
$$

where $\lambda_{sum} \equiv \sum_{i=1}^{k} \lambda_i$ and $p_i \equiv \lambda_i/\lambda_{sum}$.

Appendix B

Monte Carlo Confidence Intervals

The procedure of obtaining the confidence intervals shown in Fig. 3.7 is described as follows. We first assume that the observed SN1987A events were a statistically probable outcome so that the best fit parameters are a good approximation to the true parameters when we use a Monte Carlo simulation to sample fake data sets. In each iteration of such Monte Carlo simulation, the number of events in each detector as well as the event energies are allowed to fluctuate according to the relevant probability distribution functions. There is a small yet non-negligible probability, 5% (13.5%) with the best fit parameters found from using the three (two) late-time KAM-II events, that no events are sampled for both detectors in an iteration and such instances will be neglected. With each fake data set that contains at least one sampled event, the combined likelihood function $\mathcal{L}^{\text{fake data}}_{\text{combined}}(\mathcal{I}_{\bar{\nu}_e}, T_\nu)$ is maximized to find the "best fit" point which is then plotted as one gray dot in Fig. 3.7. The distribution of the gray dots then suggests the uncertainty in the fitted parameters one would observe from repeating the same experiment.

The streak-like structures of the gray dots are due to the fact that the number of sampled events is discretized; the streaks closely follow the trajectories that predict integral numbers of events in KAM-II detector in the region where the predicted number of events for IMB is much less than 1. The streaks apparently do not suggest a smooth probability distribution function of the parameters as would

be expected in typical parameter estimation analyses. However, imagine that, if the detector masses were continuously varied, the streaks as well as the total event contours (red and green dashed contours in Fig. 3.7) would have continuously swept across the parameter space. This means that the physical parameters should not be restricted to discretized possibilities resulting from low statistics. Therefore, we construct the 68.3% (1σ) and 95.4% (2σ) confidence intervals by choosing Δ such that the contours defined by

$$\log \mathcal{L}^{1987A}_{\rm combined}(\mathcal{I}_{\bar{\nu}_e}, T_\nu) = \log \mathcal{L}^{1987A}_{\rm combined,max} - \Delta \tag{B.1}$$

enclose the corresponding percentage of the gray dots. To ensure good convergence of the enclosure probability, 10^5 iterations are performed in the Monte Carlo simulation. For the analysis with the three (two) KAM-II events, $\Delta_{1\sigma} = 1.26$ (0.93) and $\Delta_{2\sigma} = 4.00$ (3.58). We remark that these values are somewhat different from those derived based on asymptotic normality of the log-likelihood function which is, of course, invalid in this case.

Appendix C

The Paraxial Solution

The paraxial solution [82, e.g.] is a solution that describes a laser beam with a transverse Gaussian distribution at the beam waist. It is an approximate solution to the wave equation

$$\left(-\partial_t^2 + \nabla^2\right) \Psi(\vec{r}, t) = 0. \tag{C.1}$$

We summarize the derivation of this solution and discuss its criteria here. Suppose we were to find an energy eigenstate allowed by the wave equation and we assume that the spatial and temporal dependence of the desired solution are separable. Plugging

$$\Psi(\vec{r}, t) = \Phi(\vec{r})\, T(t) \tag{C.2}$$

in the wave equation leads to

$$\frac{1}{T(t)} \frac{\mathrm{d}^2 T(t)}{\mathrm{d}t^2} = \frac{1}{\Phi(\vec{r})} \nabla^2 \Phi(\vec{r}) = \text{constant}, \tag{C.3}$$

where the constant is conventionally defined to be $-k^2$. The wave number k is equivalent to momentum in natural units. Eq. (C.3) contains two independent equations; one involves only the time variable and the other only the position variables. The spatial equation, known as the Helmholtz equation, requires a specific boundary condition to be specified before a solution can be determined. For instance, plane waves $e^{i\vec{k}\cdot\vec{r}}$ and spherical waves e^{ikr}/r are solutions with different

boundary conditions. The paraxial solution is derived by imposing a transverse Gaussian profile at the beam waist plane which will be defined as $z = 0$.

By assuming that the spatial part of the wave function takes the form

$$\Phi(\vec{r}) = \phi(\vec{r})\, \mathrm{e}^{ikz} \tag{C.4}$$

and that the z-derivative of the envelop function $\phi(\vec{r})$ varies insignificantly over the distance of a wavelength along the z-direction, i.e.

$$\left|\frac{\partial^2}{\partial z}\phi(\vec{r})\right| \ll \left|k\frac{\partial}{\partial z}\phi(\vec{r})\right|, \tag{C.5}$$

the Helmholtz equation reduces to the paraxial wave equation

$$\left(\nabla_\perp^2 + 2ik\frac{\partial}{\partial z}\right)\phi(\vec{r}) \approx 0. \tag{C.6}$$

Moreover, we plug in the above equation an ansatz solution

$$\phi(\vec{r}) \propto \exp\left[p(z) + \rho^2 q(z)\right], \tag{C.7}$$

where $\rho \equiv \sqrt{x^2 + y^2}$ and $p(z)$ and $q(z)$ are two complex-valued parameterization functions, and then impose the boundary condition $\phi(\vec{r}) \propto \exp\left(-\rho^2/4a_t^2\right)$ at $z = 0$. It follows that $p(z)$ and $q(z)$ can be solved from Eq. (C.6). Then, one finds that Eq. (C.6) has a solution

$$\phi(\vec{r}) = \frac{A}{\sigma_t(t)} \exp\left\{-\frac{\rho^2}{4\sigma_t(z)^2} + i\left[\frac{k\rho^2}{2R(z)} - \zeta(z)\right]\right\}, \tag{C.8}$$

where A is a normalization constant, $L_R \equiv 2ka_t^2$ is the Rayleigh range, $\sigma_t(z) \equiv a_t\sqrt{1 + z^2/L_R^2}$, $R(z) \equiv z\left(1 + L_R^2/z^2\right)$, and $\zeta(z) \equiv \tan^{-1}(z/L_R)$. Combining with the time-dependent part $T(t) = \exp\left(-ikt\right)$, we obtain the approximate solution shown in Eq. (4.10). The real part of $\Phi(\vec{r})$ is plotted in Fig. C.1, from which it can be seen that the solution behaves as a plane wave at $z \ll L_R$ and as a spherical wave at $z \gg L_R$.

The paraxial approximation shown in Eq. (C.5) is made in simplifying the Helmholtz equation and here we examine the criteria of the approximation. By

directly computing $\partial_z^2\phi(\vec{r})$ and $\partial_z\phi(\vec{r})$ in terms of the dimensionless variables,

$$\begin{aligned} \tilde{z} &\equiv z/L_R \text{ and} \\ \tilde{\rho} &\equiv \rho/a_t, \end{aligned} \tag{C.9}$$

we find

$$\frac{\partial\phi(\vec{r})}{\partial z} = \frac{\phi(\vec{r})}{L_R(1+\tilde{z})^2}\left\{-\tilde{z}\left(1+\tilde{z}^2-\frac{1}{2}\tilde{\rho}^2\right)+i\left[\frac{1}{4}\left(1+\tilde{z}^2\right)\tilde{\rho}^2-1\right]\right\} \tag{C.10}$$

and

$$\begin{aligned} \frac{\partial^2\phi(\vec{r})}{\partial z^2} = \frac{\phi(\vec{r})}{L_R^2(1+\tilde{z})^2}\Bigg\{&\left[-\tilde{z}+\frac{\tilde{z}\tilde{\rho}^2}{2(1+\tilde{z}^2)}+i\left(\frac{\tilde{\rho}^2(1-\tilde{z}^2)}{4(1+\tilde{z}^2)}-1\right)\right]^2+1-\tilde{z}^2 \\ &+\frac{\tilde{\rho}^2}{2}-\frac{2\tilde{z}^2\tilde{\rho}^2}{1-\tilde{z}^2}+i\left[\frac{\tilde{\rho}^2}{2\tilde{z}}\left(\frac{(1-\tilde{z}^2)^2}{1+\tilde{z}^2}-1\right)-2\tilde{z}\right]\Bigg\}. \end{aligned} \tag{C.11}$$

We then examine the approximation, Eq. (C.5), in the following regions on the first quadrant of the 2D plane of $\tilde{\rho}$ and $\tilde{z}$ (the same results can be applied to the other three quadrants).

1. $\tilde{\rho} \lesssim 1$ and $\tilde{z} \lesssim 1$:

   The moduli of the terms enclosed within the curly brackets in Eq. (C.10) and Eq. (C.11) are of order $\mathcal{O}(1)$. Therefore the approximation requires $L_R^{-1} \ll k$ or, equivalently, $(ka_t)^2 \gg 1$.

2. $\tilde{z} \sim \tilde{\rho} \gg 1$: The terms within the curly brackets in Eq. (C.10) and Eq. (C.11) are dominated by the one with the highest combined order of $\tilde{z}$ and $\tilde{\rho}$. Both sets of curly brackets are dominated by the fourth order terms so they are of the same order of magnitude. By the same argument as in region 1, the approximation requires $(ka_t)^2 \gg 1$.

3. $\tilde{z} \gg \tilde{\rho}$ and $\tilde{z} \gg 1$:

   If $\tilde{z} \gg \tilde{\rho} \gg 1$, $|\partial_z\phi| \sim |\phi L_R^{-1}(1+\tilde{z})^{-2} \times \max(\tilde{z}^3, \tilde{z}^2\tilde{\rho}^2)|$ and $|\partial_z^2\phi| \sim |\phi L_R^{-2}(1+\tilde{z})^{-2} \times \max(\tilde{z}\tilde{\rho}^2, \tilde{\rho}^4)|$. Regardless of whether $\tilde{z}$ is greater than

$\tilde{\rho}^2$, the approximation requires $ka_t \gg 0$. If $\tilde{z} \gg 1 \gtrsim \tilde{\rho}$, Eq. (C.10) and Eq. (C.11) are dominated by the term with highest order in $\tilde{z}$. It is then straightforward to conclude that the approximation requires $ka_t \gg 0$ as well.

4. $\tilde{\rho} \gg \tilde{z}$ and $\tilde{\rho} \gg 1$:

   Following similar reasoning to that for region 3, it can be shown that the approximation requires $(ka_t)^2 \gg \tilde{\rho}^2/\tilde{z}^2$ if $\tilde{\rho} \gg \tilde{z} \gg 1$ and $(ka_t)^2 \gg \tilde{\rho}^2$ if $\tilde{\rho} \gg 1 \gtrsim \tilde{z}$. Since $\tilde{\rho}$ is a variable, the approximation is not valid in this region. However, $\phi(\vec{r})$ is exponentially suppressed in this region and thus $\partial_z^2\phi(\vec{r})$, which is proportional to $\phi(\vec{r})$, can be safely neglected from the Helmholtz equation.

In conclusion, the paraxial approximation $|\partial_z^2\phi(\vec{r})| \ll |k\partial_z\phi(\vec{r})|$ requires

$$(ka_t)^2 \gg 1. \tag{C.12}$$

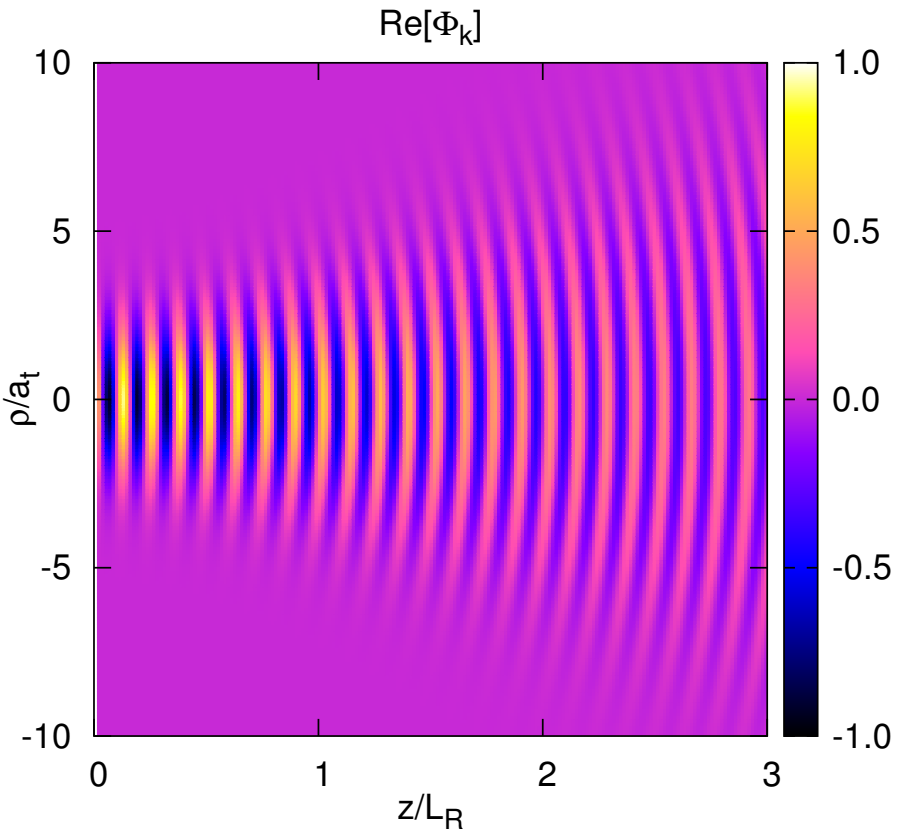

Figure C.1: The real part of $\Phi(\vec{r})$ assuming $k_0 a_t = 5$ and arbitrary A. The longitudinal and transverse coordinates are scaled by L_R and a_t, respectively. At $z \gg L_R$, the transverse width increases linearly with z.

Appendix D

Length Approximation for the HBT Effect

We begin by defining the average production-detection separation vector

$$\vec{L}_0 \equiv \frac{1}{2}(\overrightarrow{P_1D_1} + \overrightarrow{P_2D_2}) = \frac{1}{2}(\overrightarrow{P_1D_2} + \overrightarrow{P_2D_1}) \tag{D.1}$$

along with two separation vectors for the pairs of production and detection processes

$$\begin{aligned} \vec{\Delta}_P &\equiv \overrightarrow{P_1P_2} \\ \vec{\Delta}_D &\equiv \overrightarrow{D_1D_2}. \end{aligned} \tag{D.2}$$

The second equality of Eq. (D.1) can be obtained by adding $\vec{\Delta}_P$ to one vector and subtract $\vec{\Delta}_P$ from the other (alternatively, $\vec{\Delta}_D$ can be used). Then the four separation vectors shown in Fig. 5.1 can be expressed as

$$\begin{aligned} \overrightarrow{P_1D_1} &= \vec{L}_0 + \frac{1}{2}\vec{\Delta}_P - \frac{1}{2}\vec{\Delta}_D \\ \overrightarrow{P_1D_2} &= \vec{L}_0 + \frac{1}{2}\vec{\Delta}_P + \frac{1}{2}\vec{\Delta}_D \\ \overrightarrow{P_2D_1} &= \vec{L}_0 - \frac{1}{2}\vec{\Delta}_P - \frac{1}{2}\vec{\Delta}_D \\ \overrightarrow{P_2D_2} &= \vec{L}_0 - \frac{1}{2}\vec{\Delta}_P + \frac{1}{2}\vec{\Delta}_D, \end{aligned} \tag{D.3}$$

which allow the expansion of each distance up to a desired order of Δ/L_0.

As these distances are related to the quantum phase relevant for the HBT effect, the error resulting from such expansion should not exceed the de Broglie wavelength. From hindsight, the only conceivable candidate source to observe neutrino HBT effect from is a galactic core-collapse supernova ($L_0 \sim 10^{20}$ m). The typcial supernova neutrinos momentum is of order 10 MeV which corresponds to a de Broglie wavelength of order $\lambda_{dB} \sim 10$ fm. As the size of proto-neutron star (~ 10 km) dominates the size of a supernova neutrino detector, we deduce that the factor $\max(\Delta_P, \Delta_D)/L_0 \sim 10^{-16}$. The second order terms of such expansion corresponds to an order of magnitude 10^{-12} m ($\gg \lambda_{dB}$) whereas the third order terms are about 10^{-28} m $\ll \lambda_{dB}$. Therefore, the following length approximations will be up to second order.

The length of each vector can be expressed explicitly with $\vec{L}_0$, $\vec{\Delta}_P$, and $\vec{\Delta}_D$ according to Eq. (D.3). For instance,

$$\begin{aligned} L_{11} &= \left|\overrightarrow{P_1 D_1}\right| \\ &= L_0 \left[1 + \left(\hat{L}_0 \cdot \hat{\Delta}_P\right) \frac{\Delta_P}{L_0} - \left(\hat{L}_0 \cdot \hat{\Delta}_D\right) \frac{\Delta_D}{L_0} + \frac{1}{4L_0^2} \left(\vec{\Delta}_P - \vec{\Delta}_D\right)^2\right]^{\frac{1}{2}}, \end{aligned} \tag{D.4}$$

which can be expanded using $\sqrt{1+\epsilon} = 1 + \epsilon/2 - \epsilon^2/8 + \mathcal{O}(\epsilon^3)$. By keeping terms only up to second order in Δ/L_0, Eq. (D.4) can be approximated as

$$\begin{aligned} L_{11} = L_0 \Bigg\{ & 1 + \left(\hat{L}_0 \cdot \hat{\Delta}_P\right) \frac{\Delta_P}{2L_0} - \left(\hat{L}_0 \cdot \hat{\Delta}_D\right) \frac{\Delta_D}{2L_0} + \left(\vec{\Delta}_P - \vec{\Delta}_P\right)^2 \frac{1}{8L_0^2} \\ & - \left(\hat{L}_0 \cdot \hat{\Delta}_P\right)^2 \frac{\Delta_P^2}{8L_0^2} - \left(\hat{L}_0 \cdot \hat{\Delta}_D\right)^2 \frac{\Delta_D^2}{8L_0^2} \\ & + \left(\hat{L}_0 \cdot \hat{\Delta}_P\right) \left(\hat{L}_0 \cdot \hat{\Delta}_D\right) \frac{\Delta_P \Delta_D}{4L_0^2} + \mathcal{O}\left(\frac{\Delta^3}{L_0^3}\right) \Bigg\}. \end{aligned} \tag{D.5}$$

Similar approximations can be made to the other three distances. With patience,

one finds

$$\begin{aligned} L_{11} + L_{22} - L_{21} - L_{12} &\approx -\frac{1}{L_0}\left[\vec{\Delta}_P \cdot \vec{\Delta}_D - \left(\vec{\Delta}_P \cdot \hat{L}_0\right)\left(\vec{\Delta}_D \cdot \hat{L}_0\right)\right] \\ &= -\frac{\vec{\Delta}_{P,\perp} \cdot \vec{\Delta}_{D,\perp}}{L_0} \\ L_{11} - L_{22} + L_{21} - L_{12} &\approx -2\vec{\Delta}_D \cdot \hat{L_0} = -2\Delta_{D,\parallel} \\ L_{11} - L_{22} - L_{21} + L_{12} &\approx 2\vec{\Delta}_P \cdot \hat{L_0} = 2\Delta_{P,\parallel}, \end{aligned} \tag{D.6}$$

where the decomposition $\vec{\Delta} = \vec{\Delta}_\parallel + \vec{\Delta}_\perp$ is defined with respect to $\hat{L}_0$.